POLYTECHNIC SCHOOL OF THE UNIVERSITY OF SÃO PAULO

Graduate Program in Civil Engineering

Osvaldo Dario Quintana Ruiz

A coupled thermo-mechanical model for the simulation of discrete particle systems in advanced manufacturing

São Paulo

2021

OSVALDO DARIO QUINTANA RUIZ

A coupled thermo-mechanical model for the simulation of discrete particle systems in advanced manufacturing

Revised Version

Thesis submitted to the Graduate Program in Civil Engineering of the Polytechnic School of University of São Paulo in partial fulfillment of the requirements for the obtention of the degree of Doctor in Science.

Area of Concentration: Structural Engineering

Advisor:
Prof. Dr. Eduardo M.B. Campello

São Paulo

2021

Name: QUINTANA RUIZ, Osvaldo Dario
Title: A coupled thermo-mechanical model for the simulation of discrete particle systems in advanced manufacturing.

Thesis submitted to the Graduate Program in Civil Engineering of the Polytechnic School of University of São Paulo in partial fulfillment of the requirements for the obtention of the degree of Doctor in Science.

Area of concentration: Structural Engineering.

Approved in:

Thesis Defense Committee

Prof. Dr. Eduardo M. B. Campello (President)
Institution: USP
Judgment: _____

Prof. Dr. Carlos Manuel Tiago Tavares Fernandes
Institution: IST/Lisboa
Judgment: _____

Prof. Dr. Eduardo A. Fancello
Institution: UFSC
Judgment: _____

Prof. Dr. José Luís Drummond Alves
Institution: COPPE/UFRJ
Judgment: _____

Prof. Dr. Cheng Liang-Yee
Institution: USP
Judgment: _____

QUINTANA RUIZ, Osvaldo Dario. **A coupled thermo-mechanical model for the simulation of discrete particle systems in advanced manufacturing.** 2021. Num of pages 151 p. Thesis (Doctor in Science) – Polytechnic School – University of São Paulo, São Paulo, 2021.

Abstract

Modern industry, such as in aerospace, automotive, biomedical and military fields, has adopted advanced manufacturing (such as particle sintering-like processes and other 3D printing) as a rapid and efficient alternative for manufacturing industrial parts. Also, state-of-the-art techniques in the civil engineering industry include 3D concrete printing and cement-based additive manufacturing processes. All these techniques invariably include thermally-active particles, such as sintering powders and functionalized cementitious materials. The purpose of this work is to present a thermo-mechanical model for the simulation of problems involving thermo-mechanically-active particles forming discrete particles systems in advanced manufacturing. Our approach is based on the Discrete Element Method (DEM), combined with lumped heat transfer equations to describe the various thermal phenomena that may take place for such systems. Particles' motion and their thermal states over time are computed under the influence of body (e.g., gravitational) forces, contact and friction forces (and the related moments w.r.t. the particles' centers), adhesive forces as well as applied heat from external devices, heat transfer through conduction (upon contact with other particles and objects), convective cooling and radiative effects. Phase transformation, which may be critical in certain applications, is also considered. A numerical scheme is presented for solution of the model's equations. We then develop direct, large-scale numerical simulations to illustrate the validity of the proposed scheme and its practical use to the simulation of modern advanced manufacturing processes.

Keywords: Particles, thermo-mechanical effects, multiphysical particle systems, advanced manufacturing and 3D printing, discrete element method (DEM)

QUINTANA RUIZ, Osvaldo Dario. **Um modelo acoplado termo-mecânico para a simulação de sistemas discretos de partículas em manufatura avançada.** 2021. Num de Pág. 151 f. Tese (Doutor em Ciências) – Escola Politécnica – Universidade de São Paulo, São Paulo, 2021.

Resumo

A indústria moderna, em especial os setores aeroespaciais, de defesa, automotivo e biomédico, recentemente começou a adotar a manufatura avançada (como processos de sinterização e aglutinação de partículas e outros processos de impressão em 3D) como uma alternativa rápida e eficiente para a fabricação de peças. Além disso, técnicas mais recentes na indústria da construção civil estão começando a utilizar a impressão de concreto em 3D e processos de manufatura aditiva a base de cimento. Todas essas técnicas invariavelmente incluem partículas termicamente ativas, como pós de sinterização e materiais granulares cimentícios. O objetivo desde trabalho é apresentar um modelo computacional termomecânico para o estudo e simulação de problemas envolvendo partículas termicamente ativas constituindo sistemas dinâmicos discretos na manufatura avançada. A abordagem é baseada no método dos elementos discretos (MED), combinado com equações de transferência de calor para descrever os diversos fenômenos de origem térmica. As posições das partículas e suas temperaturas ao longo do tempo são calculadas sob a influência de forças de campo (por exemplo, gravitacionais), forças de contato e atrito (e seus respectivos momentos em relação aos centros das partículas), forças de adesão, assim como do calor aplicado a partir de dispositivos externos, da transferência de calor por condução (a partir do contato com outras partículas ou objetos), e do resfriamento por convecção e radiação. Mudança de fase, que pode ser crítica em algumas aplicações, também é considerada. O trabalho apresenta um procedimento numérico para solução das equações do modelo, além de uma série de simulações numéricas para validar e ilustrar o esquema proposto e o seu uso prático em processos que envolvem manufatura avançada.

Palavras-chave: partículas, efeitos termomecânicos, sistemas multi-físicos de partículas, manufatura avançada e impressão em 3D, método dos elementos discretos (MED)

Este exemplar foi revisado e corrigido em relação à versão original, sob responsabilidade única do autor e com a anuência de seu orientador.

Assinatura do autor: _____

Assinatura do orientador: _____

Catalogação-na-publicação

Quintana Ruiz, Osvaldo Dario
A coupled thermo-mechanical model for the simulation of discrete particle systems in advanced manufacturing / O. D. Quintana Ruiz -- versão corr. -- São Paulo, 2021.
151 p.

Tese (Doutorado) - Escola Politécnica da Universidade de São Paulo. Departamento de Engenharia de Estruturas e Geotécnica.

1.Partículas 2.Efeitos termomecânicos 3.Sistemas multifísicos de partículas 4.Manufatura avançada e impressão 3D 5.Método dos elementos discretos (MED) I.Universidade de São Paulo. Escola Politécnica. Departamento de Engenharia de Estruturas e Geotécnica II.t.

To my parents, Rufino and Beatriz

ACKNOWLEDGMENTS

I would like to express my deep gratitude to my advisor, Professor Eduardo MB Campello, for his support, guidance and advice during this research. Thanks for all you have taught me and for always encourage me to keep working.

I would also like to thank Professor Antonio Aquino (from Paraguay), for encouraging me to come to São Paulo and for his support at the beginning of this journey.

I wish to express my sincere thanks to my colleagues and staff of the Laboratory of Computational Mechanics (LMC) of the Polytechnic School at the University of São Paulo (POLI-USP), I am very grateful for their kindness and friendship, and for creating a friendly environment, which is very important for who is far from home.

To all members of my family, thanks for supporting me spiritually and for the encouragement along this process.

I would like to offer my special thanks to The National Program of Scholarships Abroad for the Strengthening of Research, Innovation and Education in Paraguay "Don Carlos Antonio López" (BECAL), for the financial support of my research under the grant 590/2016.

Finally, my greatest thanks to my lovely wife, Patricia Giménez. I have an immense gratitude for her patience and support that I have needed during these challenging past years.

SUMMARY

LIST OF FIGURES

LIST OF SYMBOLS

ρ	specific mass
r	radius
C	center of mass
t_0	initial time instant
t_F	final time instant
t^r	time at reference configuration
t	time at current configuration
$\boldsymbol{x}_c^r$	position vector of the center of the particle in the reference configuration
$\boldsymbol{v}_c^r$	velocity vector of the center of the particle in the reference configuration
$\boldsymbol{\alpha}^{\Delta}$	incremental rotation vector
$\boldsymbol{x}^r$	position vector of a material point in the reference configuration
r^r	radial vector of the particle (vector that connects the center of the particle and a material point on its surface)
$\boldsymbol{Q}_{\Delta}$	rotation tensor
$\boldsymbol{A}_{\Delta}$	Skew ($\boldsymbol{\alpha}^{\Delta}$)
$\boldsymbol{v}_c$	velocity of particle's center of mass in the current configuration
$\boldsymbol{\Omega}$	velocity tensor of the particle in the current configuration
$\boldsymbol{\omega}$	spin of the particle in the current configuration
$\boldsymbol{a}$	acceleration of the center of mass of the particle
$\dot{\boldsymbol{\Omega}}$	angular acceleration tensor
$\boldsymbol{\lambda}$	linear momentum
$\boldsymbol{\mu}$	angular momentum
V	volume of the particle
$\boldsymbol{J}$	inertial tensor of the particle
$\boldsymbol{I}$	identity tensor
$\boldsymbol{f}^{tot}$	vector of the total forces acting on the center of mass of the particle
$\boldsymbol{m}_c^{tot}$	vector of the total moments acting on the center of mass of the particle
N_P	total number of particles
$\boldsymbol{x}_i$	position vector of the particle i
$\boldsymbol{v}_i$	velocity vector of the particle

$\boldsymbol{\omega}_i$ spin vector of the particle

α_i^{Δ} incremental rotation vector of the particle

m_i mass of the particle

r_i radius of the particle

$\boldsymbol{f}_i^{con}$ vector of the forces due to mechanical contacts

$\boldsymbol{f}_i^{fric}$ vector of the forces due to friction

$\boldsymbol{f}_i^{adh}$ vector of the adhesion forces

$\boldsymbol{f}_i^{env}$ vector the forces due to the environment and external fields

$\boldsymbol{f}_{ij}^{con}$ force that acts on particle i due to its contact with particle (or object) j

$\boldsymbol{f}_{ij}^{bond,el}$ bond elastic force vector

$\boldsymbol{f}_{ij}^{con,el}$ contact force vector in case there is no bonding

$\boldsymbol{f}_{ij}^{con,d}$ viscous damping vector

$\boldsymbol{f}_{ij}^{bond,d}$ viscous damping vector when bond criterion is met

$\boldsymbol{m}_i^{fric}$ moment due to friction forces

$\boldsymbol{m}_i^{rol}$ moment induced by rolling resistance effects

$\boldsymbol{g}$ gravity acceleration vector

N_i^C number of particles and objects that are in contact with particle i

m^* effective mass

r^* effective radius

E^* effective elasticity modulus

G^* effective shear modulus

E_i elasticity modulus of particle i

ν_i Poisson coefficient of particle i

G shear modulus of particle i

δ_{ij} overlap between the pair $i-j$

$\boldsymbol{n}_{ij}$ unit vector connecting the center of particle i to the center of particle (or object) j

$\boldsymbol{t}_{ij}$ tangential (or sliding) direction of the pair $i-j$

$\boldsymbol{s}_{ij}$ rolling axis direction of the pair $i-j$

d^{con} contact´s damping constant

d^{fric} friction damping constant

d^{rol} rolling resistance damping constant

d^* adhesion damping constant

ξ^{con} normal damping rate of the contact

ξ^{fric} tangential damping rate

ξ^{rol} rolling resistance damping rate

ξ^{bond} bonding damping rate

k^{fric} stiffness of the frictional spring

$\boldsymbol{\Delta x}_{ij}^{trial}$ trial elastic deformation in the tangential direction for the pair $i-j$

$\boldsymbol{\Delta x}_{ij}^{r}$ elastic deformation at the reference configuration for the pair $i-j$

$\boldsymbol{\Delta \theta}_{ij}^{trial}$ pair′s trial rotation for the pair $i-j$

$\boldsymbol{v}_{ij,t}$ tangential relative velocity between i and j

$\boldsymbol{v}_i^P$ velocity at the contact point i

$\boldsymbol{v}_j^P$ velocity at the contact point j

$\boldsymbol{r}_i^P$ vector who links the center of i

$\boldsymbol{r}_j^P$ vector who links the center of j

μ_s static friction coefficient

μ_d dynamic friction coefficient

μ_r rolling resistance coefficients

$\boldsymbol{m}_{ij}^{fric}$ moment on particle i due to its friction with particle (or object) j

$\boldsymbol{m}_{ij}^{rol}$ rolling resistance moment on particle i due to its rolling over particle (or object) j

Δt time-step size between two consecutive instants

ψ force potential

r_{eq} equilibrium position of i with respect to j

d_{eq} equilibrium distance of i with respect to j

r_{crit} inflection point of the potential

d_{crit} critical distance of the interaction $i-j$

δ_{eq} equilibrium overlap of the interaction

δ_{crit} critical overlap of the interaction

$\delta_{ij,\max}$ maximum penetration of the contacting particles $i-j$

W_{adh} work of adhesion of the particles under a fluid

γ interfacial surface energy

k_{adh} stiffness of the adhesion spring

α_{adh} exponent of the adhesion force

ε_{ij} normalized overlap or local contact deformation

$\varepsilon_{ij,eq}$ equilibrium deformation of the pair $i-j$

$\varepsilon_{ij,crit}$ critical deformation

$\boldsymbol{v}_{ij,rel}$ pre-collision relative velocity between $i-j$

δt_{con} duration of the collision

K_i particle i´s kinetic energy

U_i^{int} particle i´s internal energy

P_i^{ext} mechanical power due to the external forces

Q_i^{ext} particle i´s heat input from external devices

Q_i^{cond} particle i´s heat flow due to conduction

Q_i^{conv} particle i´s heat flow due to convection

Q_i^{rad} particle i´s heat flow due to radiation

C_i specific heat of the particle

C_E environment´s specific heat

μ_E environment´s fluid viscosity

ε_i particle´s radiative cooling efficiency (or material emissivity)

B Stefan-Boltzmann constant

θ_i particle´s temperature

θ_E environment´s temperature

θ^* critical temperature

$\theta_{i,m}$ melting temperature of particle i

$\theta_{i,v}$ vaporization (or boiling) temperature of particle i

Q_{ij}^{cond} conduction heat flow on particle i due to its contact with particle (or object) j

A_{ij}^C contact area between the pair $i-j$

A_i^s total surface area of the particle i

k_{mat} material´s thermal conductivity

k_E environment´s thermal conductivity

h_i convection (or film) coefficient of the particle i w.r.t its surrounding environment

Nu Nusselt number

Re Reynolds number

Pr	Prandtl number
η_{air}	viscosity of the air
I_i^{dev}	device's input power at the particle i's location
a_i	particle i's absorptance
I_0	nominal input intensity
$d_{\max}$	maximum penetration (or heating reach)
z_i	depth of particle i with respect to the device's striking position
μ	material's attenuation coefficient
λ_i	radial distance of the particle i
w	beam spot size
f	distribution factor
P_0	nominal power of the laser in (W)
ϕ	porosity
$\Delta\theta$	thermal gradient of the particle between two configurations
α_i	thermal expansion coefficient of the particle i
$C_{i,solid}$	specific heat in the solid phase
$C_{i,liquid}$	specific heat in the liquid phase
$C_{i,gas}$	specific heat in the gas phase
$L_{i,m/s}$	latent heat of melting or solidification
$L_{i,v/c}$	latent heat of vaporization (or condensation)

LIST OF TABLES

Chapter 1

Introduction

1.1 Motivation

Recently, modern industry, such as in aerospace, automotive, biomedical, and military fields, has adopted advanced manufacturing (such as 3D printing and other particle sintering-like processes) as a rapid and efficient alternative for manufacturing industrial parts. According to Cotteleer et al. [1], NASA, for example, used seventy 3D-printed parts for the fabrication of its last Mars Rover vehicles, and more recently, SpaceX has been using 3D-manufactured components for its rocket engines. In the same line, the automotive industry has turned to this technology as a source of innovation allowing the production of customized parts, sometimes with individual properties, with a remarkable reduction of the material usage since this technique utilizes only the material that is necessary to produce the component. BMW, for example, has recently revealed its plans for a fully 3D-printed car (see Mouzakis [2]). On the other hand, in the civil engineering industry, state-of-the-art applications include 3D concrete printing and cement-based additive manufacturing processes. These processes allow the production of 3D large-scale complex geometries or building components, sometimes even without the use of temporary supports. In this context, two technologies are emerging in the construction industry, one is material extrusion, especially used for printing concrete, and the other is the particle-bed 3D printing. In the first, an object is produced layer-by-layer with a nozzle that deposits cemented-based materials along a defined path (see Figure 1a, XtreeE [3]), while in the second, an adhesive solution is deposited selectively with a printer head (see Figure 1b, Lowke et al. [4]) onto a dry particle bed in order to bind the particles (the fluid in this technique may be a mixture of cement, water, and admixtures or resin).

Figure 1 – Two techniques of additive manufacturing used in the construction industry.
a) Material extrusion b) Particle-bed 3D printing

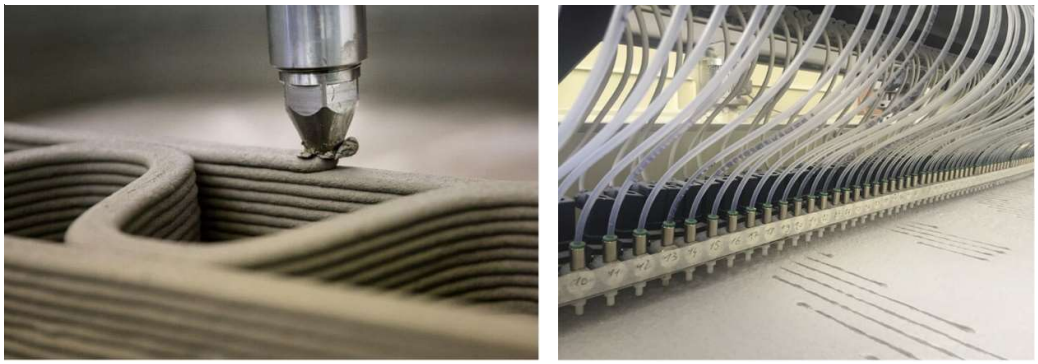

(a) (b)

Source: a) XtreeE [3] b) Lowke et al. [4].

In general, Additive Manufacturing (AM) can provide innumerous benefits which may include: (i) enabling design of shapes that are hard (if not impossible) to create using traditional processes; (ii) reduced energy consumption; and (iii) reduced material usage, to cite just a few. AM techniques invariably include granular materials in the form of thermo-mechanically-active particles, such as sintering powders and functionalized cementitious materials. From a mechanistic point of view, these particles constitute discrete particle systems, which may be subjected to a range of multiphysical effects. In order to have a reliable and fairly accurate representation of their behavior under external (both thermal and mechanical) excitations, a multiphysical description is required.

Lately, understanding and modelling the behavior of the mechanical and thermal states of granular and particulate media has been a major research subfield, and discrete particle simulation plays an important role in this regard. In particular, this technique has become an efficient analysis tool that may provide very rich information at any desired time instant of a simulation, such as the trajectories of (and transient forces acting on) individual particles, their individual temperatures, heat powers, and many others, which are difficult (if not impossible) to obtain by conventional experimental techniques. Additionally, discrete approaches that explicitly take into account the various interactions that happen at the level of the particle contacts have gained increasing attention in order to replicate the behavior of granular media.

One of their most recent engineering applications nowadays is in the advanced manufacturing field.

1.2 Justification

Granular systems display different characteristics on multiple spatial and temporal scales. In this sense, while the response of granular materials (from a macroscopic scale) may at times appear to be similar to that of a continuum, when seen from the mesoscale, they are essentially a system of multiple (and interacting) discrete particles. According to Richard et al. [5], granular materials constitute (after water) the most processed materials in industry and engineering. They are ubiquitous in nature, industry and can be observed in various forms (e.g., powder, sand, coal and granular assemblies like food grains, to cite just a few). In this context, in addition to physical experiments, computational simulation and numerical approaches can be useful tools to a better understanding of the phenomena involved in those materials. Indeed, in the past few decades, there has been a considerable increase in the development and use of numerical methods (such as, but not only, the discrete element method) for the study of granular materials, including their various intricacies and myriad applications. With regard to heat transfer in particulate media, however, the developments are more recent and not as numerous. Albeit this deficiency, it can be already found in the literature that the conduction contribution is considered the most significant form of heat transfer (see, e.g., Schlünder [6]). It depends on the conductivity of the particles' constituent material, the inter-particle contacts (which provide one source of coupling between the thermal and mechanical fields) and the overall structure of the particle packing. Other contributions, such as convective cooling and radiative effects, are often ignored – though they may likewise play an important role, depending on the granular scale.

In recent years, AM, in its turn, has become a topic of great interest for the industry. The possibility to create high customized parts or complex lightweight structures constitutes some of the most important advantages of this technology. Among the large number of AM-classified processes, Selective Laser Sintering (SLS) is a type of powder bed fusion technique which

provides a host of benefits. For example, it offers the opportunity to create objects for a wide range of applications, sometimes in a matter of hours, or enables the printing of multiple parts (e.g., prototypes for testing) at once, to cite just a few. However, and according to King et al. [7] and Anon [8], manufacturers indicated that the not poor mechanical proprieties but the unpredictable proprieties of the final manufactured product still the principal barrier to adoption of AM (including SLS, see Figure 2). In this context, simulation and modeling can provide a mechanism to develop a deeper understanding of the physical process in order to manage the quality and in-service properties of AM parts. Moreover, simulation techniques can be used to enhance and optimize process performance.

Figure 2 – Principal barriers for manufactures to adopt AM technology

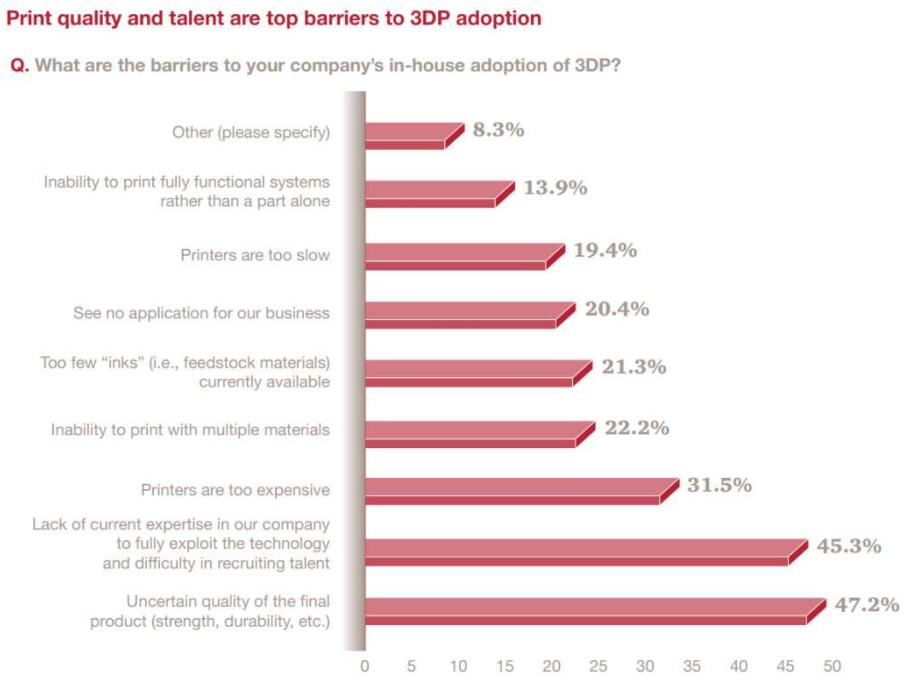

Source: PwC and Zpryme survey and analysis, "2014 Disruptive Manufacturing Innovations Survey," conducted in February 2014. Number of respondents: 108, apud Anon [8].

The purpose of this work is to develop a multiphysics (thermo-mechanical) computational model for the simulation of problems involving thermo-mechanically-active particles forming discrete particle systems and apply it to the simulation of modern AM processes. We aim to incorporate all essential ingredients that are relevant to the problem, such as inter-particle contact and bonding, heat transfer through conduction, radiation and convection, as well as

phase transformation. Our approach is based on the DEM for description the particles´ dynamics, combined with simple (lumped) heat transfer equations to describe the various thermal phenomena that may take place when the system is excited by temperature gradients and external heat sources. We are able to track the motion of the particles and their thermal states over time under the influence of body (e.g. gravitational) forces, contact and friction forces (and the related moments w.r.t the particles´ centers), adhesive forces, rolling resistance effects, as well as applied heat from external devices, heat transfer through conduction (at the particles´ interfaces upon contact with other particles and objects), convective cooling and radiative effects. Phase transformation, which may be critical in certain applications, is also considered through a simplified scheme. The model is relatively simple and straightforward to be implemented by engineers and analysts interested in the field, and may be a useful tool for practical, rapid process simulation, design, and analysis.

The DEM formulation that we adopt here is that of Campello [9] [10] and [11] for the mechanical part of the problem. Our strategy to incorporate thermal effects into it follows the same framework as that of Zohdi [12] and [13]. But it has some distinguished features: (i) we allow the particles to have rotational motion; (ii) we adopt a fully consistent stick-slip friction model (this is the friction type that is most frequently observed in dry granular materials, see e.g., Duran [14]) for arbitrary rotational particles; (iii) we take rolling resistance into account; (iv) we consider convective and radiative effects into the particles´ cooling behavior, as well as thermal expansion (and shrinkage), and (v) we incorporate an original adhesion force model to allow for inter-particle bonding in an effective way. Another distinction is that our contact and heat conduction models are based on parameters that are directly related to the underlying material properties of the particles, in contrast to Zohdi's model, which adopts “general” parameters that require problem-dependent calibration.

1.3 Objective

The main objective of this work is to develop a multiphysics numerical model for the simulation of problems involving thermo-mechanically-active particles forming discrete particle systems, and enable it to the study of modern AM processes and, in particular, SLS process. We emphasize the coupling between particle motion and heat transfer in dry particulate systems. The computational implementation is addressed through an in-house DEM code developed by the author. The main contribution is the incorporation of thermal effects into the DEM formulation of Campello [9] [10] [11], as well as the development of an original adhesion force model for inter-particle bonding, ultimately enabling the technique for the study and simulation of modern engineering applications involving dry particulate media. We remark that our objective here is not to develop a super complex model and an extremely accurate simulation tool, but instead to propose a model that is purposely simple, yet covering all the essential ingredients of thermo-mechanical particle systems for practical and rapid simulation of AM applications.

1.3.1 Specific objectives

- To extend the DEM (mechanical-only) model of Campello [9] [10] [11] as to incorporate thermal effects into it, using physical models to describe the various forms of heat transfer mechanisms such as conduction, convection, and radiation for discrete particles systems.
- To develop a model to represent the input of heat from external devices (e.g., fire nozzles, burners, laser beams, etc.) into discrete particle systems.
- To develop or incorporate a model to account for phase transformation within the developed DEM formulation.
- To develop an adhesion force model to represent the bonding of particles derived from melting at high temperatures, as observed in AM processes.

- To implement all developments above into an in-house DEM code, and validate the implementations against reference results (possibly with analytical or numerical solutions to compare with).
- To perform large-scale numerical simulations to illustrate the validity of the proposed scheme and its practical use to the simulation of AM techniques and, in particular, SLS processes.

1.4 Literature Review

In this subsection, we will present a literature review of the main topics related to the development of the thesis. Firstly, an overview of the most important aspects of the DEM will be discussed, especially about its origins, which were based on a purely mechanical approach, and its current state-of-the-art. Secondly, the pioneering considerations of thermal effects in particle systems will be approached and finally, the main aspects with respect to advanced AM processes will be drawn.

1.4.1 An overview of the discrete element method

The seminal ideas of the discrete element method were firstly proposed by Peter Cundall [15] [16] in the early 1970s–1980s to model mechanical problems, specifically in the context of geological engineering, and then by Professor Otto Strack in two reports to the United States' National Science Foundation (see Cundall and Strack [17] [18]), and a later one, in the journal Géotechnique (Cundall and Strack [19]). Originally, the method consisted of an assembly of confined rigid disks conforming a domain of particles (where each particle represented an individual grain size) where the application of Newton's second law gives the motion of the particle resulting from the forces acting on it, and therefore of the entire particle domain. While at the same time and with the same objective, other researchers attempted to describe the motion of an assembly of discs and spheres by conducting experiments (e.g., Duran [14] and

Wakabayashi [20]) or by analytical models (with mono-sized particles, e.g., Deresiewicz [21]), the contribution of Cundall achieved a greater relevance because he accomplish the solution through a numerical approach.

In essence, the DEM is a numerical tool for the simulation of large number of particles (either fully rigid or locally deformable) with emphasis on the contact locations and conditions that cannot be established "a priori" and, as consequence, need to be continuously updated during the simulation. According to Bićanić [22], applications may range for those of an inherently discontinuous behavior (particulate materials, sediment transport, brick masonry, to cite just a few) to modeling continuum-discontinuum problems. In its beginnings, the numerical approach consisted in represent the grain-to-grain contacts and friction by forces (e.g., elastics forces) through linear functions of the displacements, and the solution to obtain the new positions of the particles was given by explicit time integration of the equations, where the effect of dissipation on local (due to contacts and friction) and global (damping on velocities and spins) energy was also considered.

According to Campello [10], Cundall and Strack initially named their model as "the distinct element method", a name that several years later would turn into the current designation. Since then, several authors have proposed different contributions in this framework for the resolution and simulation of problems involving granular materials. In this sense, Thomas and Bray [23] attempting to achieve more realistic particle shapes, proposed to model nonspherical geometries by sticking disk particles together to create rigid clusters. Years later, Vu-Quoc et al. [24] used the same ideas to approximate ellipsoidal particles through clusters of overlapping spheres, which included a validation by physical experiments with different types of materials (e.g., aluminum, acrylic and glass) with qualitative agreement between the experimental and numerical part. The same procedure was performed by Favier et al. [25] and O'Sullivan [26] with a combination of overlapping spheres arranged in an axisymmetric configuration.

To increase the level of sophistication, Das et al. [27] proposed an algorithm to create cluster particles from digital images of real sands grains. In this technique, disks are subsequent added to conform a cluster in order to capture the shape from a binary image of the particle. In the same line, Jerves et al. [28] and Medina and Jerves [29] proposed another approach by the so-called "cloning algorithm", where a set of particles are created following the same

morphological parameters, such as aspect ratio, roundness, principal geometric directions, and spherical radius of a sample of real grains that have been previously digitalized. Another type of nonspherical shape is the superquadric (or superquadratic in 3D) geometry, which is an extension of spheres and ellipsoids. Firstly proposed in mathematics by Barr [30], this type of geometry has been used in DEM by several authors, especially for industrial applications (see Cleary [31] [32], Cleary and Sawley [33] and Podlozhnyuk et al. [34]). One more alternative type of geometry used to model granular materials is the polygonal (or polyhedral in 3D) particle, introduced by Cundall [35], here the contact detection is approximated through six types of potential contacts that can occur in polyhedral particles such as: (i) corner-corner; (ii) corner-edge; (iii) corner-face; (iv) edge-edge; (v) edge-face and (vi) face-face. Other authors like Nezami and Hashash [36], Pöschel and Schwager [37], Alonso-Marroquin and Wang [38] has proposed different approaches for the contact collision detection for this type of particles, however, still a lack of knowledge on how to compute the contact forces of this type of bodies.

In parallel (and almost at the same time) to the work of Cundall and Strack, Serrano and Rodriguez-Ortiz [39] propose a model with the same goal for a few number of particles, where the contact force was based on the Hertzian contact theory, and the friction force (for the tangential elastic deformations) by a spring with stiffness based on the Mindlin's theory. Here, the numerical solution scheme was based on the displacement method for the derivation of the global stiffness matrix (differently from the work of Cundall that does not resort to the use of matrices), where if at least one particle was underconstrained the stiffness matrix becomes singular, and the rearrangement of the particles becomes impossible. Moreover, the calculation of the stiffness matrix must be updated every time a contact is detected (or broken) with a highly computational cost, which certainly was too very influenced by the computational resources at that time.

Nowadays, as stated by Li et al. [40], DEM can be considered as a part of Lagrangian particle methods, which also include molecular dynamics (MD), Brownian dynamics (BD), and the dissipative particle dynamics (DPD). This classification can be seen schematically in Figure 3. Although there are various approaches of DEM, two categories of them are more relevant in the modeling of granular particle dynamics, which, according to O'Sullivan [41], both Duran [14] and Zhu et al. [42] they are the *soft sphere models* and *hard sphere models*. The main differentiation between both approaches is whether the particles are considered to be fully rigid

or locally deformable or not at their contact points. In the first, an overlap or penetration is allowed at the particles' contacts, whereas in the second, no penetration is considered.

Figure 3 – Schematic diagram indicating the time and length scales for various particles methods with typical applications

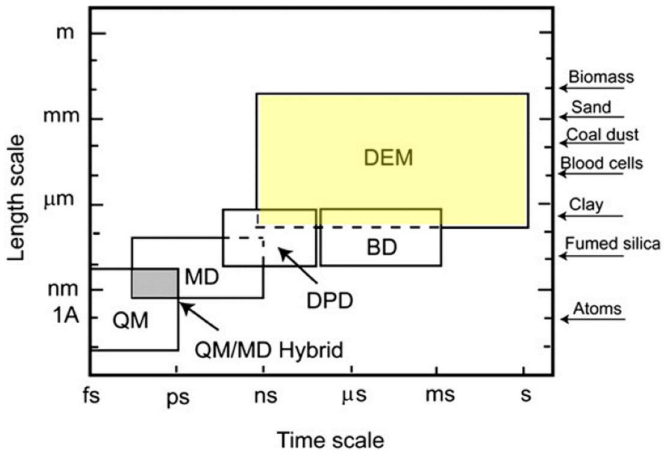

Source: Adapted from Li et al. [40].

So far, we limit the description of the method to the quasi-static regime (or confined flow). According to Zhu et al. [42], there is another area of great interest in the context of simulation of granular materials, when the particles behave like a fluid (or unconfined flow), where in contrast to the previous, solid-like and fluid-like behaviors may occur at the same time. Applications in this area are more related to industries such as pharmaceutical, chemical, food, and ceramic (e.g., flow in a hopper under gravity forces, flow in a rotating drum or mixing of particulate materials). The applicability of DEM of this type of flows has been conducted by Zhang and Vu-Quoc [43] with good agreement with experimental results in the case of inclined flows and by Matchett et al. [44], Yang and Hsiau [45] and Saeki [46] in vibrating flows. In the same context, in the presence of a fluid medium, the particle motion will be influenced by the hydrodynamic force exerted by the fluid (e.g., drag force, lift force). In this sense, the drag force is the driving force for the fluid-particle interaction, and it depends on a drag coefficient (which in turn depends on the Reynolds number of the flow and the fluid properties), the particle-fluid relative velocity and the particle size, O'Sullivan [41]. According to Zhu et al. [47], besides the drag and lift forces, other types of forces take part in this mechanics, such as the pressure gradient force (or buoyancy force), virtual mass force (the necessary force to accelerate the

fluid around the particle) and, the Basset force (force due to the lagging boundary layer development with changing relative velocity and accounting for the viscous effect). Several applications in engineering processes can be found in Zhu et al. [42], Curtis and Van Wachem [48], Feng et al. [49], and Feng and Owen [50].

1.4.2 Modeling of thermal effects in particles systems

Researching on heat transfer in granular media dates back to the 1960s, firstly focused on the modeling and understanding of both radiation and conduction phenomena across granular materials. Various types of heat transfer mechanisms can be present in a particulate system, including the heat generation derived from collisions between particles (or objects) or chemical reactions derived from the presence of a reactive substance onto the surface of the particle, as depicted in Figure 4. According to Radjaï and Dubois [51], the different types of heat transfer mechanics turns out to be more complex in particulate systems. In this context, to better understand the heat transfer mechanism in particle systems, Schlünder [6] analyzed the transfer of heat by conduction from rigid walls to adjacent packed beds (wall-to-particle) and the heat conduction in packed beds (particle-to-particle), and an attempting to solve the heat convection by particle motion. Here, it is important to emphasize that at that time, there was still a lack of knowledge about the particle dynamics, and in the words of the author:

> "More difficult is the analysis of the phenomenon of heat convection by particle motion, mainly because of the fact that the particle motion is not well known. At present more or less arbitrary modelling of particle motion is a typical attempt to overcome this difficulty."

Following the same line, and attempting to contribute with the understanding of other types of heat transfer mechanics, experiments were carried out by Sun and Chen [52] where they analyzed the impacting heat exchange between spherical particles and particles with surfaces (where the relative motion between particles-to-particles or particle-to-objects can be

a source of heat generation[1]) or in the case of heat transfer between particle-to-gas and gas-to-particle (gas penetrating into the particle array), where Molerus [53] compared his theoretical model (equivalent pipe diameter) with experiment results from the literature. In both cases, the results conducted (in some circumstances) to largely contradictory conclusions, reason why the researchers resorted to the numerical approach in order to enhance the understanding of this phenomenon.

Figure 4 – Different phenomena of local heat transfer

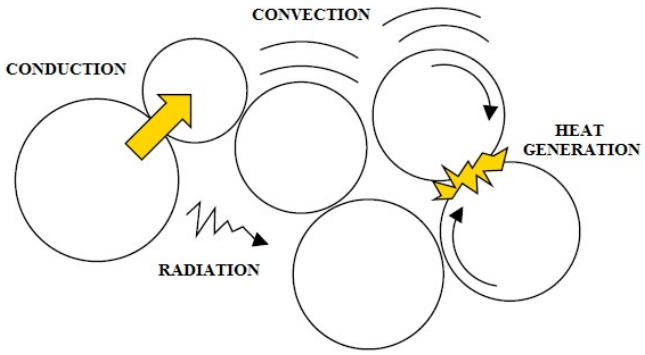

Source: Adapted from Radjaï and Dubois [51].

As mentioned in the previous paragraph, initially the focus was to improve the knowledge of heat transfer due to radiation and conduction. In the context of radiative effects, Chen et al. [54] proposed the first analytical model from the work of Siegel and Howell [55] and, Yang et al. [56] the first numerical model based on a Monte-Carlo approach. Moreover, other authors like Singh and Kaviany [57], Strieder [58] and Brewster [59] attempted to contribute with other different approaches and here, it is important to emphasize that all of them consider the particles with no particular mechanical role, only thermal properties like its resistance or thermal barrier were taken into account in the propagation of radiation. Later, Argento and Bouvard [60] coupled the radiation and conduction effects from the numerical model of Yang et al. [56] to investigate the evolution of the global conductance of a sample when this becomes more densified.

On the other hand, and with respect to heat transfer through conduction, the determination of the contact area constitutes an important part of the mechanism since this

[1] This research is among the first to draw attention in this aspect.

controls the amount of heat flux between particles (or particles with objects). In this sense, Batchelor and O'Brien [61] proposed an approximately analytical solution by assuming flat surfaces and elastic materials between sphere-sphere and sphere-plane contacts in the presence of a fluid, these individual contact conductances were then used to predict the effective thermal conductivity of a granular assembly. In the same line, other analytical approaches were generally based on spherical particle-to-particle contacts to estimate the thermal conductance where the contact area is obtained through the assumption of elasto-plastic behavior (see Majumdar and Bhushan [62], Sridhar and Yovanovich [63]) or by a multi-scale behavior (see Jackson et al. [64]). Another approach, though valid only for 2D particles (i.e., circles or disks), is the discrete thermal element method (DTEM) proposed by Feng et al. [65], which is a particular solution of the Dini's integral, where the heat conduction within a particle is considered by solving analytically the temperature distribution over a circular domain subjected to Neuman boundary conditions and the number of unknowns (temperature) is equal to the number of its neighboring particles in contact, however they did not present any comparison of their results with existing models from the literature. In addition, Siu and Lee [66] proposed the Discrete Conduction Model (DCM) where a uniform temperature is assigned to each particle and constructs the energy conservation equation in terms of the thermal resistances between these contacting spherical particles. Similarly to the DTEM approach, a number of heat pipes are assumed between the particles through which the heat flux between then and there is a thermal resistance for each contact.

With respect to numerical methods, besides of the initial efforts of Argento and Bouvard [60] [67], Hunt [68] proposed a discrete model to analyze the evolution of the temperature as a function of its agitation and compared his results with theoretical assumptions. Other authors like Cheng et al. [69] found a direct link between the structure of the granular material to its effective thermal conductivity. According to Radjaï and Dubois [51], the work of Vargas-Escobar [70] can be considered the first attempt to the thermo-mechanical modeling of discrete media with the introduction of the term "thermal particle dynamics" (TPD). In this approach, the thermal contact conductance of two contacting particles is integrated into DEM for the simulation of few identical particles under vacuum conditions, taking into account in the same framework, both local thermal phenomena and mechanical behavior. Here, the value of the thermal conductance depends on the contact radius (i.e., varies with the magnitude of the

normal force) and may be obtained from Hertz contact theory (previously, a similar approach was performed by Chan and Tien [71] for a bed of particles) and the interface between the particles is assumed to be isothermal, since the particles present a very low degree of roughness. A similar approach was presented by Ji and Liu [72] with the incorporation of the thermal resistance (reciprocal of the thermal conductance) of a contact particle pair into the DEM framework.

Zhang et al. [73] extended the analysis for a granular assembly showing that compressive loads produce an increase of the value of the thermal conductivity and, as consequence, of the overall granular system. Moreover, in the same research shows the strong dependency of thermal resistance with respect to the particle size (i.e., when decrease the particle size, increase the value of the thermal resistance and vice versa). On the other hand, several studies have been conducted for particles with large Biot number ($\gg 1$) where the assumption of uniform temperature distribution within the particle no longer hold. Despite this is not the scope of the thesis, we refer the interested reader to selected works where the focus was to resolve the temperature distribution inside an individual particle, see Baniasadi et al. [74], Dierich et al. [75], Gan et al. [76], Oschmann and Kruggel-Emden [77] and Ozisik [78] .

1.4.3 Advanced manufacturing

AM, often referred to as 3D printing, refers primarily to the use of additive processes, combining materials (metallic, polymeric or ceramical) usually in a layer-by-layer fashion. According to ISO (International Organization for Standardization), AM it is defined as “the process of joining materials to make parts from 3D model data, usually layer upon layer, as opposed to subtractive manufacturing and formative manufacturing methodologies”. This technology came about as a result of developments in a diversity of different technology sectors, for example: computing power, control, and the improvement on the design of many kinds of subdevices used in AM processes. Also, the advances in the structural design, like topology optimization, constitutes a key point that enables to a better use and take advantage of all the capabilities of this technology. Many of the earliest AM systems were based on laser technology

and until now, continue as an ideal candidate as long as this technology requires material in each layer to be solidified or joined in a selective manner.

Today, there are various techniques of AM, which are based on different physical principles (e.g., stereolithography, multi-jet modelling, and laser sintering) and the processes differs depending on the material and machine technology used. According to the ASTM International Technical Committee F42 on AM technologies [79] the seven majors are:

1. Photopolymerization: in this technique a resin it cures or hardens to model an object by the use of an ultraviolet (UV) light;
2. Material Jetting: droplets of material (commonly polymers and waxes) are deposited onto a platform from a nozzle and, after being cooled and solidified, the layer is cured or hardened by UV light;
3. Binder Jetting: this technique is composed of two materials, a powder and a binder. The binder usually comes in a liquid form and serves to join the powder layers previously sprayed by a print head;
4. Material Extrusion: the material is deposited layer-by-layer through a nozzle in a continuous stream. The bonded occurs by temperature or by the use of chemical agents, it is commonly used in domestic 3D printers (fused deposition modeling (FDM) or fused filament fabrication (FFF));
5. Powder Bed Fusion: an external heat source, which could be a laser or electron beam, is used to melt and fuse a powder bed of particles to conform a layer. Next, a roller or a blade spread again another layer of material (~ 0.1 mm thick) and the process is repeated;
6. Sheet Lamination: sheets of metals are bound it together (e.g., by the use of an ultrasonic welding) and after the bond take place, a laser or knife cut the layer to reach the desired shape;
7. Direct Energy Deposition: a multi axis arm nozzle deposit melted material, where it solidifies. In this technique, the material can be polymer, ceramic but is usually used with metal, in the form of either powder or wire.

According to Gibson et al. [80], the principal steps in the AM process include: i) conceptualization and CAD: corresponds to the first idea and development process of the product following by the model creation through a software, scanning of an existing physical

object or a combination of all of these; ii) conversion to STL/AMF: procedure in which a CAD model is described in terms of its geometry alone by the use of a series of triangular facets iii) transfer and manipulation on AM machine: the STL file is send to the AM machine (toolpath generation); iv) machine setup: the AM machine is prepared for a build and this process varies according of the type of machine; v) build: the object is printed until the build is complete ; vi) removal and cleanup: consists of removal of excess material surrounding the object; vii) post-processing: finishing the object for the application purpose (e.g., polishing, thermal or chemical treatment, etc.); viii) application: the object is ready for use.

In this work, we will focus on the SLS process, which is a special type of the Powder Bed Fusion (PBF) technique, firstly proposed in the mid-1980s by Dr. Carl Deckard and Dr. Joe Beaman at the University of Texas at Austin. It was the first commercialized PBF process and originally was developed to produce plastic prototypes using a point-wise laser. According to Gibson et al. [80], this approach was subsequently extended to metal and ceramics powder and is very popular nowadays in the industry – reason why it is one that we opt to focus here. Basically, in this technique powder particles are sintered or partial fused (i.e., joining of particles without complete melting) through an external heat source (e.g., laser beam, electron beam) and subsequently solidified to create one solid part. According to Milewski [81], in SLS process, a heat source is used to break up surface oxides to bring atoms and molecules close enough to allow diffusion and grain growth to form metallic bonds between the particles. The final microstructure is created under a controlled porosity, and the void volume or un-sintered spaces will depend upon the material, temperature, pressure, and time (see Figure 5).

Figure 5 – Stages of powder sintering

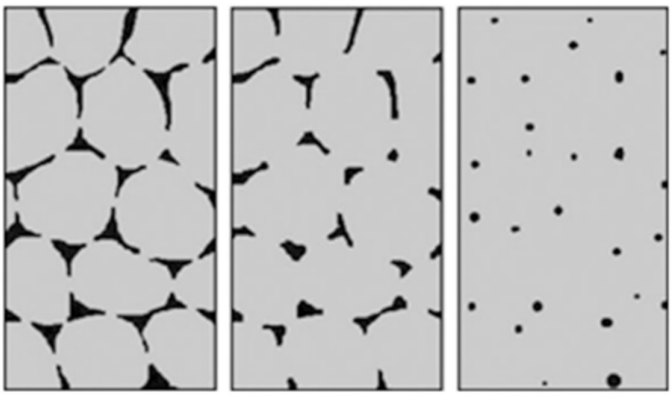

Source: Milewski [81].

With this technique, becomes easier to print alloys containing materials with different melting points, or even combine two different materials, like metal and plastic materials (e.g., alumide, which is a mixture of nylon powder and aluminum powder) and since the SLS technique does not fully melt the metal, less energy is required in the process. Another common technique in AM is the Selective Laser Melting (SLM), where the metal powder particles fully melt and fuse to each other to create a solid part. However, this approach is outside the scope of this thesis, hence is not considered here.

Figure 6 – Scanning electron microscope (SEM) morphology (x200) of 316L stainless steel powder typically used in AM processes

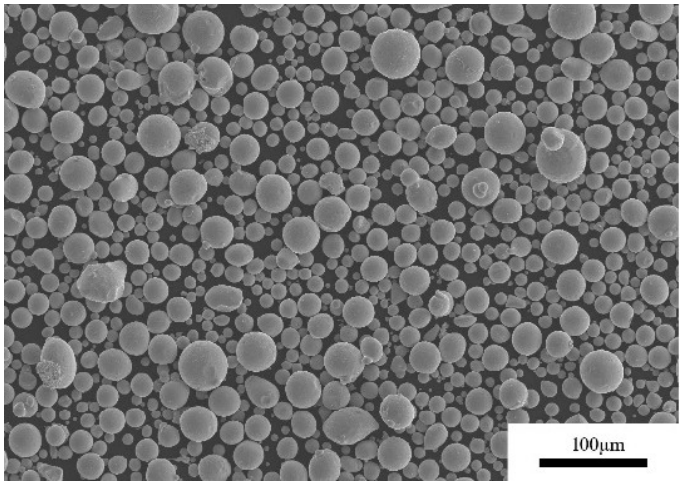

Source: Du et al. [82].

The SLS process consists in the following steps: powder particles (e.g., metallic powder, see Figure 6, Du et al. [82]) are dispersed using a blade or a counter-rotating powder leveling roller in a thin layer (typically $0.075 - 0.1$ mm thick) on top of a platform followed by a preheat of the powder which makes it easier for the laser to raise the temperature (sintering temperature) of specific regions of the powder bed. Then, the laser scans the top layer of the powder bed (according to the shape of the part that is desired to be built) causing the powder to fuse together mechanically and with the layer underneath it, and this process repeats until the build is complete. Finally, the finished part is removed and cleaned of excess powder parts, and further finishing operations, if necessary, are performed (thermal or chemical treatment, etc.). A schematic illustration can be seen in Figure 7, Chen et al. [83].

Regarding the modeling and simulation of AM processes, we can find in the literature different approaches to simulate this process. According to Ganeriwala [84], they can subdivided into empirical, continuum-based, and discrete models. All of them have their advantages and disadvantages, while the empirical models can be effective to simplify certain types of processes, they have a limitation when trying new type of materials. On the other hand, continuum-based models (e.g., finite element method, finite volume method, etc.) may help to understand the various physical phenomena involved and, at the same time, can be an efficient tool to investigate process parameter effects in order to propose optimized solutions, but fail to capture the inhomogeneities of the particle assembly and also, have problems in dealing with strong discontinuities such as contacts (with friction and adhesion) as well as phase transformation. Despite of some commercial software packages such as COMSOL, ANSYS or MoldFlow are available to simulate welding, casting or molding from a continuum-based approach, the discrete models offer better flexibility in dealing with material discontinuities and occasional phase change, which are the type of problems that we are studying in this work.

Figure 7 – Schematic SLS process

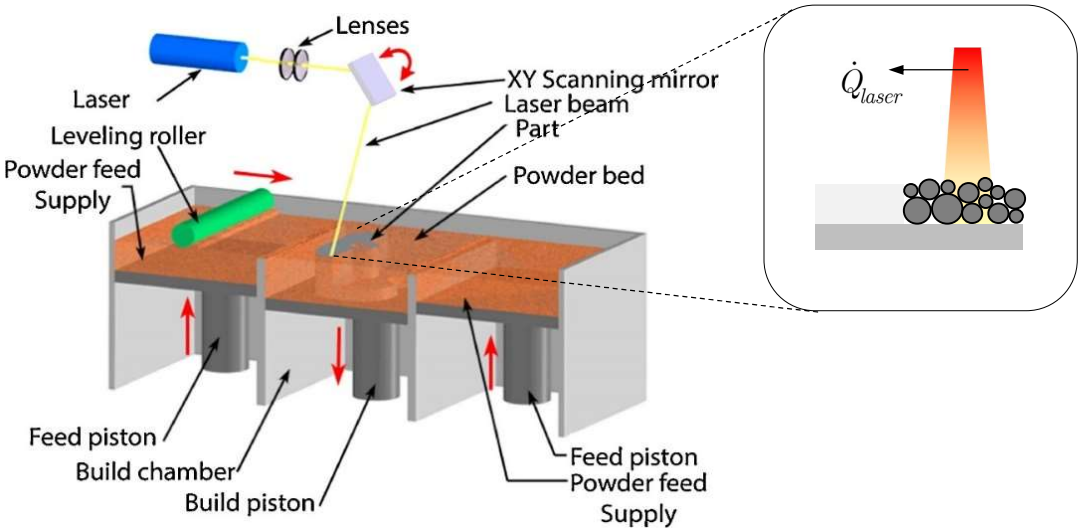

Source: Adapted from Chen et al. [83].

In the literature we found that Simchi and Pohl [85] used empirical results to determine the densification and microstructural evolution during direct laser sintering of metal powders, where the empirical sintering rate data was related to the energy input of the laser beam. Matsumoto et al. [86] calculated the temperature field and stress distribution of a single layer

forming on a metallic powder bed through a finite element model, and Antony et al. [87], use the same numerical method to perform numerical and experimental investigations of SLM of 316L stainless steel powder attempting to understand the melt zone and ball formation. Regarding to this phenomenon, the ball formation or "balling effect", can be described as large spheroidal beads around the laser beam causing voids, discontinuities, and poor surface roughness during the printing process (see Figure 8, Kirihara and Nakata [88]). In the case of AM with polymer powders, Mokrane et al. [89] propose a numerical model based on the finite volume method to simulate SLS process considering the shrinkage involved in the process.

Figure 8 – Balling effect

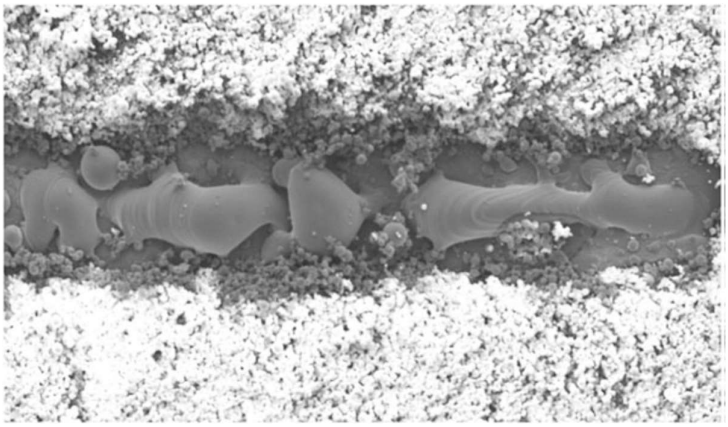

Source: Kirihara and Nakata [88].

Gusarov and Kruth [90] proposed an analytical expression for the penetration of a laser beam into a particle assembly as a function of the density and particle size distribution, part of the conclusion of this research pointed out that the attenuation coefficient[2] directly depends on the structure of the powder (size, shape, and arrangement) and not of the optical properties of the material. This realization will be used in the implementation of one type of laser beam in this work, the so-called Gaussian laser beam, as it will be seen in Chapter 4 and Chapter 5. Khairallah and Andereson [91] presented a multiphysics model using a hybrid finite element and finite volume formulation to simulate the SLM process of a random bed of 316L stainless steel particles and validate their results with experimental data with good agreement, however with an expensive computational cost for a relatively short time of simulation (~ 400 μs). Its important to highlight due to the difficult to account the phase change in the continuum-based

[2] It can also be found in the literature under the name of extinction coefficient.

models, some of the previous mentioned works decided to not consider this effect. With respect to discrete models, we refer to the pioneering works of Zohdi and his group [13] [92] [93] [94], whom are, in our opinion, one of the leading experts in the field. A comprehensive overview on advanced manufacturing techniques, including process description, industrial issues, and practical aspects, can be found in Gibson et al. [80] and specifically for AM processes using metallic powders in Milewski [81].

1.5 Organization of the thesis

The thesis is organized as follows. In Chapter 2, there is a description of the adopted DEM formulation, with the various force and moment contributions that govern the particles´ dynamics and their corresponding equations of motion. In Chapter 3, we introduce our bond model for inter-particle adhesion, with its corresponding equilibrium conditions and stability requirements. In Chapter 4, we present our developments to incorporate thermal effects into the DEM formulation, with detailed accounts of each possible heat transfer mechanism and the numerical method for solution of the system´s equations (examples are provided for validation and illustration). In Chapter 5, we show numerical examples attempting to simulate SLS manufacturing processes, and in Chapter 6 we close the thesis with our conclusions and possible future works. Throughout the text, plain italic letters ($a, b, .., \alpha, \beta, .., A, B, ..$) denote scalar quantities, whereas boldface italic letters ($\boldsymbol{a}, \boldsymbol{b}, .., \boldsymbol{\alpha}, \boldsymbol{\beta}, .., \boldsymbol{A}, \boldsymbol{B}, ..$) denote vectors in a three-dimensional Euclidean space. The (standard) inner product of two vectors is denoted by $\boldsymbol{u} \cdot \boldsymbol{v}$, and the norm of a vector by $\left\| \boldsymbol{u} \right\| = \sqrt{\boldsymbol{u} \cdot \boldsymbol{u}}$. Notation with a superposed dot is adopted to designate time derivatives.

Chapter 2

A DEM formulation for discrete particle systems

The DEM formulation presented in this chapter is based on the works of Campello [9] [10] [11]. It follows the so-called soft-sphere approach, whereby particle contacts are described and resolved through the amount of local penetration (or overlap) at their contact points. Additional features that were developed and incorporated during the course of this thesis, such as the adhesion force model and the consideration of thermal effects, will be described separately in Chapter 3 and Chapter 4, respectively. Here, we will restrict ourselves to the DEM formulation itself (i.e., to the purely mechanical part of the problem), with which we will be able to present the basic concepts underlying our model and, introduce our notation. We will first deal with the dynamics of a single particle in Section 2.1, and then with multi-particle systems (and their related forces and moments) in Sections 2.2 and 2.3. The numerical solution procedure to the model´s equations is presented in Section 2.4.

2.1 Dynamics of a single particle

We follow a Lagrangian, discrete element description and consider, for the sake of simplicity and computational efficiency, only spherical particles here. Let us assume a single particle with specific mass ρ and radius r. Let the center of mass of the particle be designated by C and $\left\{O,\boldsymbol{e}_1,\boldsymbol{e}_2,\boldsymbol{e}_3\right\}$ will be the orthonormal global (inertial) reference of the system, with origin at point O, and let $\left\{x_1,x_2,x_3\right\}$ or $\left\{x,y,z\right\}$ be the coordinates of each directions of the

system, see Figure 9. Let us consider the motion of the system between two-time instants, t_0 (initial) and t_F (final). At time $t^r, t_0 \leq t^r < t_F$, the system occupies the region in space called reference configuration, whereas at a later instant $t, t^r < t \leq t_F$, it occupies the region called current configuration. We denote the position vector of the center of the particle by $\boldsymbol{x}_c^r$, the velocity vector by $\boldsymbol{v}_c^r$, the incremental rotation vector by $\boldsymbol{\alpha}^{\Delta}$ (this is the rotation vector relative to two consecutive configurations).

Figure 9 – Kinematics of a single particle

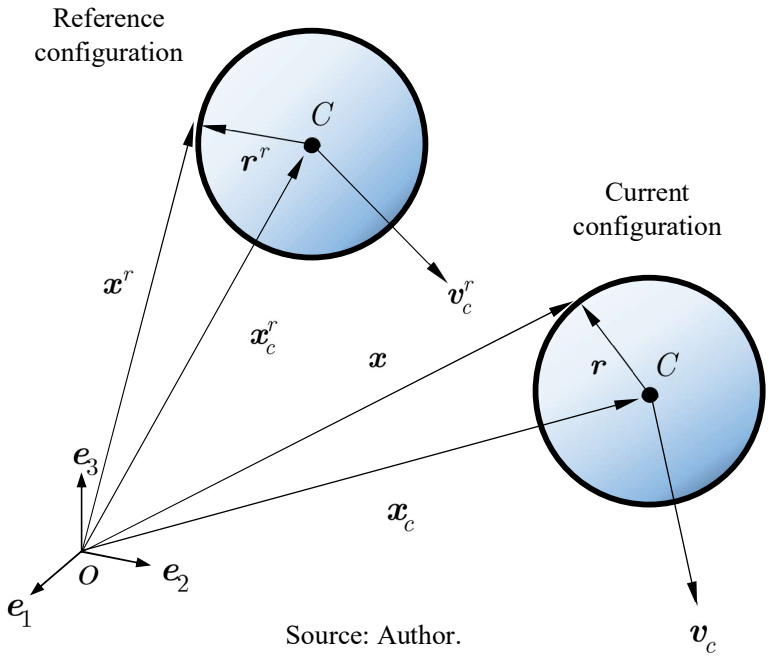

Source: Author.

The position vector of a material point on the surface of the particle in the reference and current configuration is given by

$$\boldsymbol{x}^r = \boldsymbol{x}_c^r + \boldsymbol{r}^r \quad \text{and} \quad \boldsymbol{x} = \boldsymbol{x}_c + \boldsymbol{r}, \tag{1}$$

where $\boldsymbol{r}^r$ the radial vector that links the center of mass of the particle and the material point on the surface of the particle. In the current configuration, the radial vector is expressed by

$$\boldsymbol{r} = \boldsymbol{Q}_{\Delta}\boldsymbol{r}^r, \tag{2}$$

in which $\boldsymbol{Q}_{\Delta}$ is the rotation tensor who describes the rotation of the particle between two configurations, which is given by

$$\boldsymbol{Q}_{\Delta} = \boldsymbol{I} + \frac{4}{4 + \alpha_{\Delta}^2}\left(\boldsymbol{A}_{\Delta} + \frac{1}{2}\boldsymbol{A}_{\Delta}^2\right), \tag{3}$$

where $\alpha_\Delta = \left\| \boldsymbol{\alpha}^\Delta \right\|$ and $\boldsymbol{A}_\Delta = \text{Skew}(\boldsymbol{\alpha}^\Delta)$. By taking the time derivative of equation $(1)_2$, we obtain the velocity of the material point as follows

$$\boldsymbol{v} = \dot{\boldsymbol{x}}_c + \dot{\boldsymbol{r}} = \boldsymbol{v}_c + \dot{\boldsymbol{Q}}_\Delta \boldsymbol{Q}_\Delta^T \boldsymbol{r} = \boldsymbol{v}_c + \boldsymbol{\Omega}\boldsymbol{r}, \tag{4}$$

where $\boldsymbol{v}_c = \dot{\boldsymbol{x}}_c$ is the velocity of the center of mass of the particle (here we resort to Newton's notation to denote the time derivative), and $\boldsymbol{\Omega} = \dot{\boldsymbol{Q}}_\Delta \boldsymbol{Q}_\Delta^T$ is the velocity tensor of the particle. Note that $\boldsymbol{\Omega}$ is an antisymmetric tensor, and therefore has an axial vector, which can be defined by $\boldsymbol{\omega} = \text{axial}(\boldsymbol{\Omega})$. By taking into account equation (3) we obtain

$$\boldsymbol{\omega} = \text{axial}\,(\dot{\boldsymbol{Q}}_\Delta \boldsymbol{Q}_\Delta^T) = \frac{4}{4 + \alpha_\Delta^2}\left(\boldsymbol{I} + \frac{1}{2}\boldsymbol{A}_\Delta \right)\dot{\boldsymbol{\alpha}}^\Delta = \boldsymbol{\Xi}_\Delta \dot{\boldsymbol{\alpha}}^\Delta, \tag{5}$$

where $\boldsymbol{\omega}$ corresponds to the spin of the particle, and the velocity of the center of mass of the particle in equation (4) can be rewritten as follows

$$\boldsymbol{v} = \boldsymbol{v}_c + \boldsymbol{\omega} \times \boldsymbol{r}. \tag{6}$$

The acceleration of the material point is given by the time derivative of equation (4)

$$\boldsymbol{a} = \dot{\boldsymbol{v}}_c + \dot{\boldsymbol{\Omega}}\boldsymbol{r} + \boldsymbol{\Omega}\dot{\boldsymbol{r}} = \boldsymbol{a}_c + \dot{\boldsymbol{\Omega}}\boldsymbol{r} + \boldsymbol{\Omega}(\dot{\boldsymbol{Q}}_\Delta \boldsymbol{Q}_\Delta^T \boldsymbol{r}) = \boldsymbol{a}_c + \dot{\boldsymbol{\Omega}}\boldsymbol{r} + \boldsymbol{\Omega}^2 \boldsymbol{r}, \tag{7}$$

where $\boldsymbol{a}_c = \dot{\boldsymbol{v}}_c$ is the acceleration of the center of mass of the particle and $\dot{\boldsymbol{\Omega}}$ is the angular acceleration tensor. Then, equation (7) can be rewritten as

$$\boldsymbol{a} = \boldsymbol{a}_c + \dot{\boldsymbol{\omega}} \times \boldsymbol{r} + \boldsymbol{\omega} \times (\boldsymbol{\omega} \times \boldsymbol{r}). \tag{8}$$

The linear momentum in the current configuration, taking into account equation (6) is given by

$$\boldsymbol{\lambda} = \int_V \rho \boldsymbol{v}\, dV = \int_V \rho \boldsymbol{v}_c\, dV + \int_V \rho(\boldsymbol{\omega} \times \boldsymbol{r})\, dV = m\boldsymbol{v}_c\,, \tag{9}$$

where V is the volume of the particle (which is considered constant by hypothesis), and m is the particle mass, which is defined by

$$m = \int_V \rho\, dV \tag{10}$$

The angular momentum of the particle w.r.t. its center of mass in the current configuration can be defined by

$$\boldsymbol{\mu}_c = \int_V (\boldsymbol{x} \times \rho \boldsymbol{v}) dV = \boldsymbol{x}_c \times \int_V \rho(\boldsymbol{v}_c + \boldsymbol{\omega} \times \boldsymbol{r}) dV + \int_V \boldsymbol{r} \times \rho(\boldsymbol{v}_c + \boldsymbol{\omega} \times \boldsymbol{r}) dV$$

$$= \boldsymbol{x}_c \times m\boldsymbol{v}_c + \boldsymbol{J}_c \boldsymbol{\omega}, \tag{11}$$

where

$$\boldsymbol{J}_C = \int_V \rho \left[(\boldsymbol{r} \cdot \boldsymbol{r}) \boldsymbol{I} - \boldsymbol{r} \otimes \boldsymbol{r} \right] dV, \tag{12}$$

is the inertial tensor of the particle w.r.t C. For spherical particles equation (12) stays

$$\boldsymbol{J}_C = j\boldsymbol{I} \text{ with } j = \frac{2}{5} m r^2. \tag{13}$$

where $\boldsymbol{I}$ is the identity tensor. The time derivative of equations (9) and (11) gives

$$\dot{\boldsymbol{\lambda}} = m\boldsymbol{a}_c \quad \text{and} \quad \dot{\boldsymbol{\mu}} = j\dot{\boldsymbol{\omega}}. \tag{14}$$

Now, we can define by $\boldsymbol{f}^{tot}$ and $\boldsymbol{m}^{tot}$ as the vector of the total forces and total moments acting on the center of mass of the particle. According to the Euler's laws, the following relations must hold for the particle at every time instant

$$\dot{\boldsymbol{\lambda}} = \boldsymbol{f}^{tot} \quad \text{and} \quad \dot{\boldsymbol{\mu}} = \boldsymbol{m}^{tot}, \tag{15}$$

and for spherical particles, taking into account equation (14) we have

$$\dot{\boldsymbol{\lambda}} = m\boldsymbol{a}_c \Rightarrow \dot{\boldsymbol{\lambda}}_i = \boldsymbol{f}^{tot},$$

$$\dot{\boldsymbol{\mu}} = j\dot{\boldsymbol{\omega}} \Rightarrow \dot{\boldsymbol{\mu}} = \boldsymbol{m}^{tot}. \tag{16}$$

Through equation (16), we obtain the governing equations of motion of the particle´s dynamics in terms of its velocity vector $\boldsymbol{v}$ and spin vector $\boldsymbol{\omega}$.

2.2 Dynamics of a system of particles

With the intention to characterize a system of particles, we need to adjust the notation that will be used henceforth. The position vector of the center of mass of the particle i will defined as $\boldsymbol{x}_i\,(i=1,2,3,...,N_P)$ where N_P is the total number of particles of the system. Accordingly, $\boldsymbol{v}_i$ is the velocity vector, $\boldsymbol{\omega}_i$ is the spin vector, and $\boldsymbol{\alpha}_i^{\Delta}$ is the incremental rotation vector. Moreover, m_i is the mass of the particle and r_i will be the radius of the particle, see Figure 10.

Figure 10 – Schematic representation of multiples particles

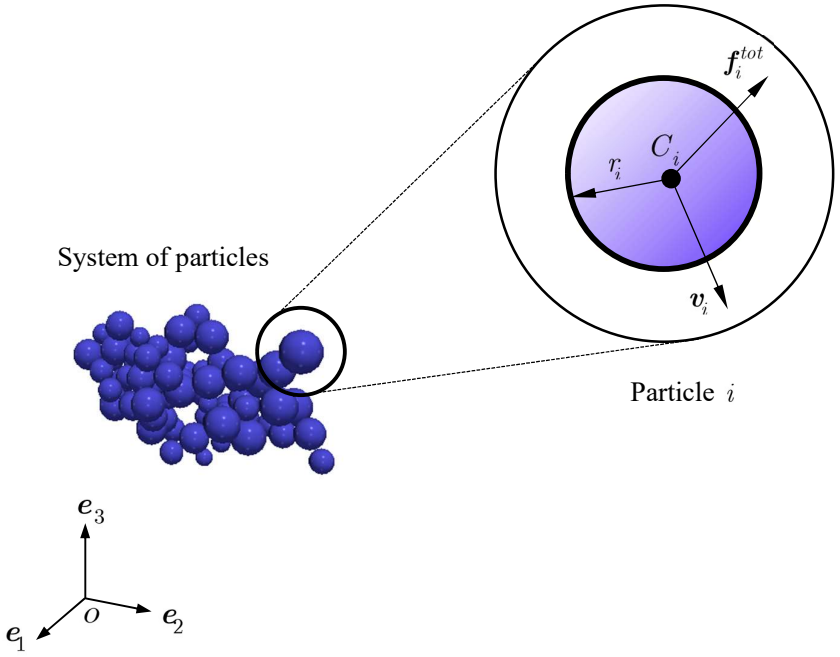

Source: Adapted from Campello [10].

The system's dynamics can be fully characterized by the following expressions

$$\begin{aligned} m_i\dot{\boldsymbol{v}}_i &= \boldsymbol{f}_i^{tot} \qquad \text{with} \qquad \boldsymbol{f}_i^{tot} = \boldsymbol{f}_i^{adh} + \boldsymbol{f}_i^{con} + \boldsymbol{f}_i^{env} + \boldsymbol{f}_i^{fric}, \\ j_i\dot{\boldsymbol{\omega}}_i &= \boldsymbol{m}_i^{tot} \qquad \text{with} \qquad \boldsymbol{m}_i^{tot} = \boldsymbol{m}_i^{fric} + \boldsymbol{m}_i^{rol}. \end{aligned} \tag{17}$$

where $\boldsymbol{f}_i^{con}$ are the forces due to mechanical contacts (or collisions) with other particles and objects, $\boldsymbol{f}_i^{fric}$ are the forces due to friction (which arise from these contacts or collisions), $\boldsymbol{f}_i^{adh}$ corresponds to adhesion forces and, $\boldsymbol{f}_i^{env}$ are the forces due to the environment and external fields (e.g., the gravitational force $m_i\boldsymbol{g}$, where $\boldsymbol{g}$ is the gravity acceleration vector). With

respect to moments, $\boldsymbol{m}_i^{fric}$ is the moment due to the friction forces (these forces are eccentric w.r.t. the particle′s center, and thereby generate a moment on the particle), and $\boldsymbol{m}_i^{rol}$ is the moment induced by rolling resistance effects (w.r.t. the particle′s center). Each one of these force and moment contributions is described next, except for the adhesion force, which as said in the introduction of this chapter will be presented separately in Chapter 3.

2.3 Forces and moments

The contact forces are given as a function of the amount of overlap between any two contacting particles (or particle and object). We follow Hertz contact theory (see Johnson [95]) and adopt the following expression:

$$\boldsymbol{f}_i^{con} = \sum_{j=1}^{N_i^c} \boldsymbol{f}_{ij}^{con}, \quad \text{with} \quad \boldsymbol{f}_{ij}^{con} = -\frac{4}{3}\sqrt{r^*}E^*\delta_{ij}^{3/2}\boldsymbol{n}_{ij} - d^{con}\dot{\delta}_{ij}\boldsymbol{n}_{ij}, \qquad (18)$$

where $\boldsymbol{f}_{ij}^{con}$ is the force that acts on particle i due to its contact with particle (or object) j, N_i^c is the number of particles and objects that are in contact with particle i and,

$$r^* = \frac{r_i r_j}{r_i + r_j} \quad \text{and} \quad E^* = \frac{E_i E_j}{E_j(1-\nu_i^2) + E_i(1-\nu_j^2)}, \qquad (19)$$

are the effective radius and the effective elasticity modulus of the $i-j$ contacting pair (in which E_i, E_j, ν_i, ν_j are the elasticity modulus and the Poisson coefficient of i and j, respectively), and δ_{ij} is the overlap between the pair (see Figure 11), which is given by

$$\delta_{ij} = \|\boldsymbol{x}_i - \boldsymbol{x}_j\| - \left(r_i + r_j\right). \qquad (20)$$

Still in equation (18), $\boldsymbol{n}_{ij}$ is the contact normal direction, or unit vector that points from the center of particle i to the center of particle (or object) j, i.e.,

$$\boldsymbol{n}_{ij} = \frac{\boldsymbol{x}_j - \boldsymbol{x}_i}{\|\boldsymbol{x}_j - \boldsymbol{x}_i\|}, \qquad (21)$$

whereas d^{con} is the contact′s damping constant (related to viscous energy dissipation in the normal direction), given by

$$d^{con} = 2\xi^{con}\sqrt{2E^* m^* \sqrt{r^*}}\,\delta_{ij}^{1/4}, \quad \text{with} \quad m^* = \frac{m_i m_j}{m_i + m_j}, \tag{22}$$

and $\dot{\delta}_{ij}$ is the overlap velocity of the contacting pair (i.e., relative velocity of the pair in the pair´s central direction). In equation (22), m^* is the effective mass of the pair $i-j$, ξ^{con} is the damping rate of the contact, which must be given (typically, one has $0 \leq \xi^{con} \leq 1$, with $\xi^{con} = 0$ standing for a perfectly elastic contact and $\xi^{con} = 1$ for a critically damped one). It is important to realize that the elastic part of the equation $(18)_2$ results always in a repulsive contribution to the contact force, whereas the viscous part, either repulsive or attractive, depending on the sign of $\dot{\delta}_{ij}$. In this sense, in the compression stage (particle-particle or particle-object moving towards each other), it is repulsive and in the decompression stage (particle-particle or particle-object moving away from each other), it is attractive. Sometimes, in the decompression stage, the attractive contribution may occasionally overcome the elastic part and the contact force results in an attractive force. To circumvent this inconsistency, it is necessary to check the sign of $(18)_2$ against $\boldsymbol{n}_{ij}$. Accordingly, if $\boldsymbol{f}_{ij}^{con} \cdot \boldsymbol{n}_{ij} > 0$, we impose that $\boldsymbol{f}_{ij}^{con} = \boldsymbol{0}$ (with $\boldsymbol{0}$ as the null vector).

Figure 11 – Overlap between a pair of particles

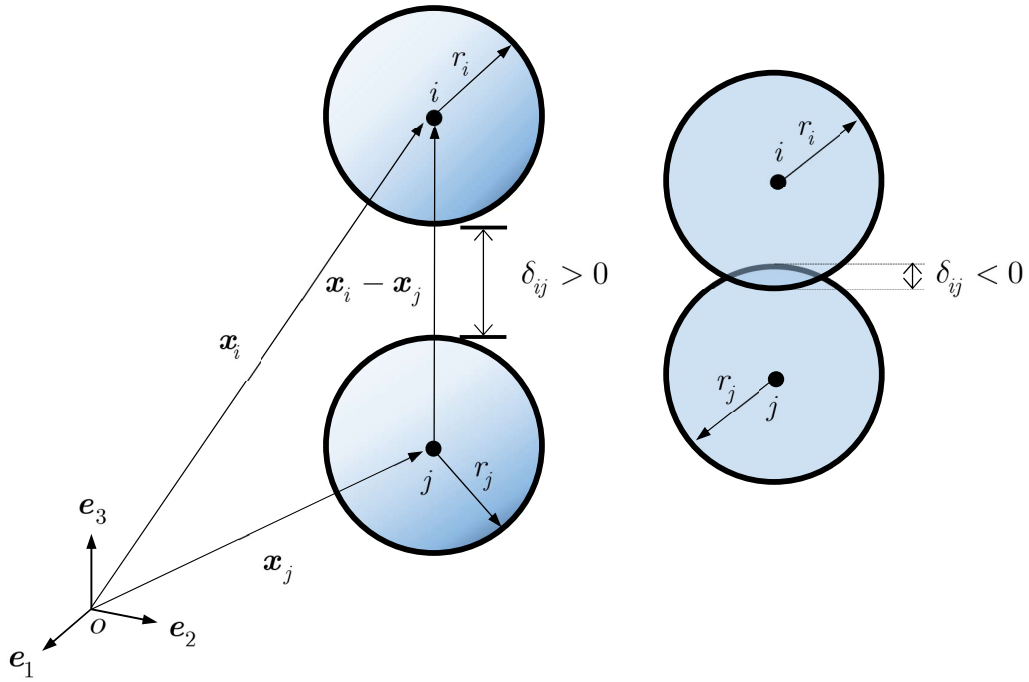

Source: Adapted from Campello [10].

The friction forces are described by means of a *stick-slip* model given by Mindlin´s elastic solution for sticking contact between spheres combined with Coulomb´s law for coupling the tangential force with the normal force whenever there is sliding (i.e., dynamic friction). Accordingly, we first consider an elastic "trial stick state" in which the friction force is

$$\boldsymbol{f}_i^{fric} = \sum_{j=1}^{N_i^c} \boldsymbol{f}_{ij}^{fric,\text{trial}}, \quad \text{with} \quad \boldsymbol{f}_{ij}^{fric,\text{trial}} = \underbrace{-8G^*\sqrt{r^*\delta_{ij}^{1/2}}}_{k^{fric}} \Delta\boldsymbol{x}_{ij}^{\text{trial}} - d^{fric}\boldsymbol{v}_{ij,t} \,. \quad (23)$$

In the above expression, k^{fric} is the stiffness of the spring (as derived from Mindlin's elastic solution, see Johnson [95]), G^* is the effective shear modulus of the contacting pair (which is a function of the pair´s individual shear moduli), given by

$$G^* = \frac{G_i G_j}{2G_i + 2G_j - G_i\nu_i - G_j\nu_j} \,, \quad (24)$$

and $\Delta\boldsymbol{x}_{ij}^{\text{trial}}$ is the pair´s trial elastic deformation in the tangential direction

$$\Delta\boldsymbol{x}_{ij}^{\text{trial}} = \Delta\boldsymbol{x}_{ij}^{r} + \Delta\boldsymbol{x}_{ij}^{\Delta,\text{trial}}, \quad (25)$$

where $\Delta\boldsymbol{x}_{ij}^{r}$ corresponds to the elastic deformation at the reference configuration, $\Delta\boldsymbol{x}_{ij}^{\Delta,\text{trial}}$ is the incremental trial elastic deformation for the pair $i-j$ from the reference to the current configuration, d^{fric} is a friction damping constant (analogous to d^{con} in equation $(22)_1$, as to allow for viscous energy dissipation in the tangential direction), such that

$$d^{fric} = 2\xi^{fric}\sqrt{m^* k^{fric}}, \quad (26)$$

where ξ^{fric} is the tangential damping rate, and $\boldsymbol{v}_{ij,t}$ is the tangential relative velocity between i and j at the contact point P (see Figure 12) denoted by

$$\boldsymbol{v}_{ij,t} = \boldsymbol{v}_{ij}^{P,rel,\tan} = \boldsymbol{v}_{ij}^{P,rel} - (\boldsymbol{v}_{ij}^{P,rel}\cdot\boldsymbol{n}_{ij})\boldsymbol{n}_{ij} \quad \text{where} \quad \boldsymbol{v}_{ij}^{P,rel} = \boldsymbol{v}_i^P - \boldsymbol{v}_j^P, \quad (27)$$

where $\boldsymbol{v}_i^P$ and $\boldsymbol{v}_j^P$ are the velocities of the contact points between the pair $i-j$ given by

$$\boldsymbol{v}_i^P = \boldsymbol{v}_i + \boldsymbol{\omega}_i \times \boldsymbol{r}_i^P \quad \text{and} \quad \boldsymbol{v}_j^P = \boldsymbol{v}_j + \boldsymbol{\omega}_j \times \boldsymbol{r}_j^P, \quad (28)$$

and $\boldsymbol{r}_i^P$ and $\boldsymbol{r}_j^P$ corresponds to the vectors who links the center of i and j with point P.

Figure 12 – Contact point between particle *i* and particle *j*

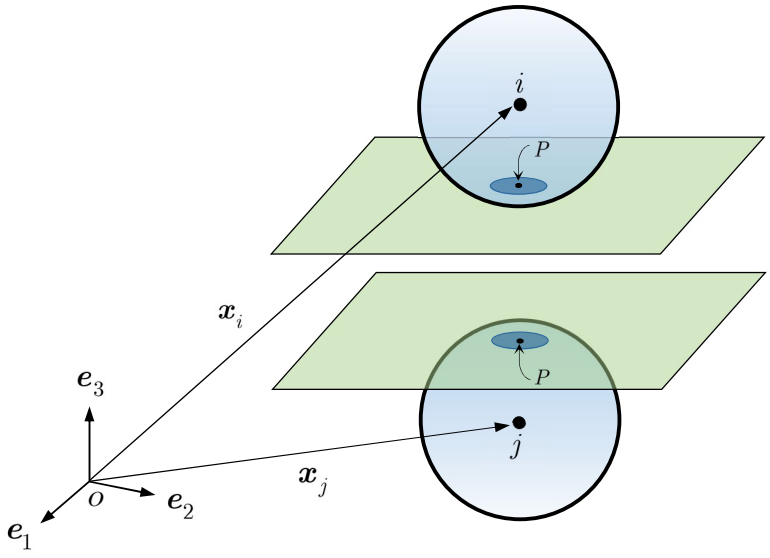

Source: Adapted from Campello [10].

If the interpenetration of the particles in the pair $i-j$ is small, which is our case, $\boldsymbol{r}_i^P$ and $\boldsymbol{r}_j^P$ can be computed by $\boldsymbol{r}_i^P \approx r_i \boldsymbol{n}_{ij}$ and $\boldsymbol{r}_j^P \approx r_j \boldsymbol{n}_{ij}$. Now, we verify it by a slip check against the static friction limit if the sticking assumption is valid or not:

$$\begin{cases} IF \quad \left\| \boldsymbol{f}_{ij}^{fric,\text{trial}} \right\| \leq \mu_s \left\| \boldsymbol{f}_{ij}^{con} \right\| \Rightarrow \boldsymbol{f}_{ij}^{fric} = \boldsymbol{f}_{ij}^{fric,\text{trial}} \ \text{(trial state is valid)}; \\ IF \quad \left\| \boldsymbol{f}_{ij}^{fric,\text{trial}} \right\| > \mu_s \left\| \boldsymbol{f}_{ij}^{con} \right\| \Rightarrow \boldsymbol{f}_{ij}^{fric} = \mu_d \left\| \boldsymbol{f}_{ij}^{con} \right\| \boldsymbol{t}_{ij} \ \text{(sliding occurs)}. \end{cases} \tag{29}$$

In equation (29), μ_s and μ_d are the static and dynamic friction coefficients, whereas $\boldsymbol{t}_{ij} = \boldsymbol{v}_{ij,t} \left\| \boldsymbol{v}_{ij,t} \right\|^{-1}$ is the tangential (or sliding) direction of the pair. Moreover, in equation (29) if sticking occurs, $\Delta \boldsymbol{x}_{ij} = \Delta \boldsymbol{x}_{ij}^{\text{trial}}$, otherwise it must be obtained by the following expression, which is essentially a return scheme for when the sticking assumption is violated:

$$\Delta \boldsymbol{x}_{ij} = \frac{1}{k^{fric}} \left(\mu_d \left\| \boldsymbol{f}_{ij}^{con} \right\| \boldsymbol{t}_{ij} - d^{fric} \boldsymbol{v}_{ij} \right), \tag{30}$$

In contrast to the normal contact force, wherein the pair´s local deformation (i.e., overlap) is given from pure geometrical arguments, in the friction force the pair´s tangential deformation has to be computed incrementally through time integration of the pair´s tangential relative velocity, which gives (along with equation (25))

$$\Delta \boldsymbol{x}_{ij}^{\Delta,\text{trial}} = \int_{t^r}^{t} v_{ij,t}(\tau)\, d\tau. \tag{31}$$

where t_r corresponds to time in the reference configuration and t to the time in the current configuration. Plus, the friction history must be stored during the whole duration of the contact. For a detailed algorithmic treatment, we refer the reader to Campello [10] [11].

For the moments due to the friction forces (relatively to the center of the particle) we have

$$\boldsymbol{m}_i^{fric} = \sum_{j=1}^{N_i^c} \boldsymbol{m}_{ij}^{fric}, \quad \text{with} \quad \boldsymbol{m}_{ij}^{fric} = \boldsymbol{r}_{ij} \times \boldsymbol{f}_{ij}^{fric}, \tag{32}$$

where $\boldsymbol{m}_{ij}^{fric}$ is the moment on particle i due to its friction with particle (or object) j, and $\boldsymbol{r}_{ij} \approx r_i \boldsymbol{n}_{ij}$ is the vector that connects the center of particle i to its contact point with particle j.

The moments due to rolling resistance, in turn, are given by a rotational spring-damper-slider model (often also called an "elastic-plastic" model), which may be thought of as the rotational version of the stick-slip friction model presented above. Accordingly, first we consider an elastic trial stick state (i.e., one in which there is no rolling) in which the rolling resistance moment is

$$\boldsymbol{m}_i^{rol} = \sum_{j=1}^{N_i^c} \boldsymbol{m}_{ij}^{rol,\text{trial}}, \quad \text{with} \quad \boldsymbol{m}_{ij}^{rol,\text{trial}} = -k^{rol} \Delta \boldsymbol{\theta}_{ij}^{\text{trial}} - d^{rol} \boldsymbol{\omega}_{ij}, \tag{33}$$

where $\boldsymbol{m}_{ij}^{rol,\text{trial}}$ is the rolling resistance moment acting on particle i due to its rolling on particle (or object) j, k^{rol} is the stiffness of the rotational spring given by Iwashita and Oda [96]'s recommendation for rolling spheres

$$k^{rol} = k^{fric}(r^*)^2 = 8G^*\sqrt{r^*\delta_{ij}^{1/2}}(r^*)^2, \tag{34}$$

and $\Delta \boldsymbol{\theta}_{ij}^{\text{trial}}$ is the pair´s trial rotation, such that

$$\Delta \boldsymbol{\theta}_{ij}^{\text{trial}} = \Delta \boldsymbol{\theta}_{ij}^{r} + \Delta \boldsymbol{\theta}_{ij}^{\Delta,\text{trial}}, \tag{35}$$

where $\Delta \boldsymbol{\theta}_{ij}^{r}$ corresponds to the rotation at the reference configuration and $\Delta \boldsymbol{\theta}_{ij}^{\Delta,\text{trial}}$ is the trial incremental rotation for the pair $i-j$ from the reference to the current configuration (increasing or decreasing the rotation between both configurations), d^{rol} is a rolling damping constant (analogous to the contact and friction damping constants in equation (23)), given by

$$d^{rol} = 2\xi^{rol}\sqrt{j^* k^{rol}}, \tag{36}$$

where ξ^{rol} is the rolling damping rate which must be known, and

$$j^* = \left(\frac{1}{j_i + m_i r_i^2} + \frac{1}{j_j + m_j r_j^2} \right)^{-1}, \tag{37}$$

is the rotational inertia of the pair $i-j$ w.r.t. its contact point, and the angular velocity $\boldsymbol{\omega}_{ij} = \boldsymbol{\omega}_i - \boldsymbol{\omega}_j$ is the relative rotational velocity between the particles contacting pair $i-j$. Now, we verify it by a slip check against the static rolling (or "yield") limit:

$$\begin{cases} IF \ \left\| \boldsymbol{m}_{ij}^{rol,\text{trial}} \right\| \le \mu_r r^* \left\| \boldsymbol{f}_{ij}^{con} \right\| \Rightarrow \boldsymbol{m}_{ij}^{rol} = \boldsymbol{m}_{ij}^{rol,\text{trial}} \quad (\text{trial state is valid}); \\ IF \ \left\| \boldsymbol{m}_{ij}^{rol,\text{trial}} \right\| > \mu_r r^* \left\| \boldsymbol{f}_{ij}^{con} \right\| \Rightarrow \boldsymbol{m}_{ij}^{rol} = \mu_r r^* \left\| \boldsymbol{f}_{ij}^{con} \right\| \boldsymbol{s}_{ij} \quad (\text{rolling occurs}). \end{cases} \tag{38}$$

Still in equation (38), μ_r is the rolling resistance coefficient, whereas $\boldsymbol{s}_{ij} = \boldsymbol{\omega}_{ij} \left\| \boldsymbol{\omega}_{ij} \right\|^{-1}$ is the rolling axis direction. Likewise in the friction case, if the assumption is violated and rolling occurs, $\Delta\boldsymbol{\theta}_{ij}$ can be obtained by the following return scheme

$$\Delta\boldsymbol{\theta}_{ij} = \frac{1}{k^{rol}} \left(\mu_r r^* \left\| \boldsymbol{f}_{ij}^{con} \right\| \boldsymbol{s}_{ij} - d^{rol} \boldsymbol{\omega}_{ij} \right), \tag{39}$$

Similarly, as to the friction force, in the rolling resistance moment the pair´s rolling rotation has to be computed incrementally through time integration of the pair´s relative rolling velocity, which gives

$$\Delta\boldsymbol{\theta}_{ij}^{\Delta,\text{trial}} = \int_{t^r}^{t} \boldsymbol{\omega}_{ij}(\tau)\, d\tau. \tag{40}$$

The total rolling rotation is then obtained by inserting this result into equation (35). Plus, its time history must likewise be stored during the whole duration of the contact. Again, for a detailed algorithmic treatment, we refer the reader to Campello [10] [11].

Remark 1. The consideration of other force and moment contributions, such as near-field interactions, electromagnetic effects from external fields, drag forces (from the surrounding environment), van der Waals effects, as well as other rolling resistance models, is entirely possible, but not considered here. The interested reader is referred to Campello [10] [11] for details. Also, it is worth mentioning that the interaction between

particles and rigid walls may be represented as a special case of that between particles, simply by taking the walls with infinite mass, radius, inertia and elastic parameters in the above force and moment expressions.

Remark 2. As it will be discussed in Chapter 4, some of the particles´ mechanical properties, such as the elasticity modulus, may vary with temperature, providing some sort of thermal softening (or stiffening) due to a change in temperature. This is one source of coupling between the thermal and mechanical fields and can be taken into account in a straightforward way by simply considering a temperature-dependent value for the corresponding property (e.g., from a given input curve), instead of a constant-valued one. This will be dealt with in subsection 4.6. Another source of coupling is the heat transfer between particles through conduction, which is dependent on the particles´ contact area and the distance between their centers – and thereby, on the particles´ positions and velocities, as will be seen in subsection 4.2.

2.4 Numerical solution method (mechanical part)

To solve the mechanical system, we proceed to numerically integrate the governing equations of the system, i.e., equation (17), for $i = 1,2,...,N_P$. First, we discretize the time interval of the analysis (t_0, t_F) into time instants $\{t_0, t_1, t_2, ..., t_i, t_{i+1}, t_F\}$, wherein for convenience we set $t_0 = 0$. Between any two consecutive instants, t_i and t_{i+1}, we adopt the configuration corresponding to t_i as the reference configuration, and t_{i+1} as the current configuration. Then, starting with $i = 0$ by time integration of the governing equations we obtain the positions, velocities, spatial orientations, and spins of the particles at t_{i+1} from their known values at t_i. Next, with those obtained values, the current configuration becomes the new reference configuration $i \leftarrow i + 1$ and subsequently the procedure is repeated until $t_{i+1} = t_F$.

Now, we defined $\Delta t = t_{i+1} - t_i$ as the time-step size between two consecutive instants, and for the sake of simplicity, let $t = t_i$ and $t + \Delta t = t_{i+1}$ be the way to identify those instants. Accordingly, for the velocities and spins of the particles, between t and $t + \Delta t$, we have

$$\begin{aligned} \boldsymbol{v}_i(t+\Delta t) &= \boldsymbol{v}_i(t) + \frac{1}{m_i}\int_t^{t+\Delta t} \boldsymbol{f}_i^{tot} dt \quad , \\ \boldsymbol{\omega}_i(t+\Delta t) &= \boldsymbol{\omega}_i(t) + \frac{1}{j_i}\int_t^{t+\Delta t} \boldsymbol{m}_i^{tot} dt \quad . \end{aligned} \tag{41}$$

with $\boldsymbol{f}_i^{tot} = \hat{\boldsymbol{f}}_i^{tot}(\boldsymbol{x}_k, \boldsymbol{v}_k, \boldsymbol{\alpha}_k, \boldsymbol{\omega}_k)$ and $\boldsymbol{m}_i^{tot} = \hat{\boldsymbol{m}}_i^{tot}(\boldsymbol{x}_k, \boldsymbol{v}_k, \boldsymbol{\alpha}_k, \boldsymbol{\omega}_k)$ where $k = 1, 2, ..., N_P$. As we can see, in equation (41) both $\boldsymbol{f}_i^{tot}$ and $\boldsymbol{m}_i^{tot}$ explicitly depends on $\boldsymbol{x}_k, \boldsymbol{v}_k, \boldsymbol{\alpha}_k, \boldsymbol{\omega}_k$ (with k standing for all particles of the system, and not only for particle i) and consequently cannot be solved analytically (except only in few cases). For that reason, the integrals of the right-hand side of the equation (41) are approximated by using a generalized trapezoidal rule

$$\begin{aligned} \int_t^{t+\Delta t} \boldsymbol{f}_i^{tot} dt &\approx \Big[\phi \boldsymbol{f}_i^{tot}(t+\Delta t) + (1-\phi)\boldsymbol{f}_i^{tot}(t)\Big]\Delta t, \\ \int_t^{t+\Delta t} \boldsymbol{m}_i^{tot} dt &\approx \Big[\phi \boldsymbol{m}_i^{tot}(t+\Delta t) + (1-\phi)\boldsymbol{m}_i^{tot}(t)\Big]\Delta t. \end{aligned} \tag{42}$$

where $\phi \in \mathbb{R}, 0 \leq \phi \leq 1$. When $\phi = 0$, the integration becomes to an explicit scheme; when $\phi = 1$, to an implicit one and when $\phi = 0.5$, to the implicit classical trapezoidal rule. By inserting equation (42) into equation (41), we arrive

$$\begin{aligned} \boldsymbol{v}_i(t+\Delta t) &= \boldsymbol{v}_i(t) + \frac{\Delta t}{m_i}\Big[\phi \boldsymbol{f}_i^{tot}(t+\Delta t) + (1-\phi)\boldsymbol{f}_i^{tot}(t)\Big], \\ \boldsymbol{\omega}_i(t+\Delta t) &= \boldsymbol{\omega}_i(t) + \frac{\Delta t}{j_i}\Big[\phi \boldsymbol{m}_i^{tot}(t+\Delta t) + (1-\phi)\boldsymbol{m}_i^{tot}(t)\Big]. \end{aligned} \tag{43}$$

with $\boldsymbol{f}_{ij}^{tot}$ and $\boldsymbol{m}_{ij}^{tot}$ given by equation (17), whereas for the positions and incremental rotations we write

$$\begin{aligned} \boldsymbol{x}_i(t+\Delta t) &= \boldsymbol{x}_i(t) + \int_t^{t+\Delta t} \boldsymbol{v}_i dt\,, \\ \boldsymbol{\alpha}_i^{\Delta}(t+\Delta t) &= \int_t^{t+\Delta t} \boldsymbol{\omega}_i dt\,. \end{aligned} \tag{44}$$

and again, by invoking the generalized trapezoidal rule for the integrals on the right-hand side of equation (44), we have

$$\begin{aligned}\int_t^{t+\Delta t} \boldsymbol{v}_i dt &\approx \big[\phi \boldsymbol{v}_i(t+\Delta t) + (1-\phi)\boldsymbol{v}_i(t)\big]\Delta t,\\ \int_t^{t+\Delta t} \boldsymbol{\omega}_i dt &\approx \big[\phi \boldsymbol{\omega}_i(t+\Delta t) + (1-\phi)\boldsymbol{\omega}_i(t)\big]\Delta t.\end{aligned} \tag{45}$$

and by introducing equation (45) into (44) we obtain

$$\begin{aligned}\boldsymbol{x}_i(t+\Delta t) &= \boldsymbol{x}_i(t) + \big[\phi \boldsymbol{v}_i(t+\Delta t) + (1-\phi)\boldsymbol{v}_i(t)\big]\Delta t,\\ \boldsymbol{\alpha}_i^{\Delta}(t+\Delta t) &= \big[\phi \boldsymbol{\omega}_i(t+\Delta t) + (1-\phi)\boldsymbol{\omega}_i(t)\big]\Delta t.\end{aligned} \tag{46}$$

The total rotation vectors of the particles are updated by means of the Rodrigues formula (for details, see Campello [9])

$$\begin{aligned}&\boldsymbol{\alpha}_i(t+\Delta t)\\ &= \frac{4}{4 - \boldsymbol{\alpha}_i(t)\cdot\boldsymbol{\alpha}_i^{\Delta}(t+\Delta t)}\left(\boldsymbol{\alpha}_i(t) + \boldsymbol{\alpha}_i^{\Delta}(t+\Delta t) - \frac{1}{2}\boldsymbol{\alpha}_i(t)\times\boldsymbol{\alpha}_i^{\Delta}(t+\Delta t)\right).\end{aligned} \tag{47}$$

The expressions (46), (43), for $i = 1,2,...,N_P$, constitute a set of nonlinear algebraic equations in which the position, velocity, spin, and incremental rotation vectors of the i^{th} particle at $t+\Delta t$ can be computed once $\boldsymbol{v}_i(t)$, $\boldsymbol{\omega}_i(t)$ and $\boldsymbol{x}_i(t)$ are known.

2.4.1 Programming algorithm

The solution process consists in a recursive strategy based on a fixed-point iterative scheme where the unknown variables (position, velocity, spin and incremental rotation vectors) are progressively updated in an inner loop over all particles, which is repeated until convergence is reached. Note that for the numerical solution, it is not necessary to solve any matrix system of equations. The algorithm is schematically outlined below:

Algorithm 1.

1. Initialize time variables and get initial conditions:

   $t = 0$, $\Delta t = \text{given}$, $t_F = \text{given}$, $\phi = \text{given}$

   $\boldsymbol{x}_i(0),\ \boldsymbol{v}_i(0),\ \boldsymbol{\omega}_i(0),\ \boldsymbol{\alpha}_i(0),\ \theta_i(0) = \text{given}$

2. Initialize time step:

   $I = 0$ (iteration counter)

   $\boldsymbol{x}_i^I(t+\Delta t) = \boldsymbol{x}_i(t)$, $\boldsymbol{\alpha}_i^{\Delta,I}(t+\Delta t) = 0$,

   $\boldsymbol{v}_i^I(t+\Delta t) = \boldsymbol{v}_i(t)$, $\boldsymbol{\omega}_i^I(t+\Delta t) = \boldsymbol{\omega}_i(t)$

3. WHILE $t \le t_F$, loop over particles: FOR $i = 1,...,N_P$ DO

   i. Compute force and moment vectors at $t+\Delta t$:

   $$\boldsymbol{f}_i^{tot,I+1}(t+\Delta t) = \hat{\boldsymbol{f}}_i^{tot}\left(\boldsymbol{x}_j^I(t+\Delta t), \boldsymbol{v}_j^I(t+\Delta t), \boldsymbol{\omega}_j^I(t+\Delta t), \boldsymbol{\alpha}_j^{\Delta,I}(t+\Delta t)\right)$$
   $$\boldsymbol{m}_i^{tot,I+1}(t+\Delta t) = \hat{\boldsymbol{m}}_i^{tot}\left(\boldsymbol{x}_j^I(t+\Delta t), \boldsymbol{v}_j^I(t+\Delta t), \boldsymbol{\omega}_j^I(t+\Delta t), \boldsymbol{\alpha}_j^{\Delta,I}(t+\Delta t)\right)$$

   ii. Update velocity and spin vectors:

   $$\boldsymbol{v}_i^{I+1}(t+\Delta t) = \boldsymbol{v}_i(t) + \frac{\Delta t}{m_i}\left[\phi \boldsymbol{f}_i^{tot,I+1}(t+\Delta t) + (1-\phi)\boldsymbol{f}_i^{tot}(t)\right]$$
   $$\boldsymbol{\omega}_i^{I+1}(t+\Delta t) = \boldsymbol{\omega}_i(t) + \frac{\Delta t}{j_i}\left[\phi \boldsymbol{m}_i^{tot,I+1}(t+\Delta t) + (1-\phi)\boldsymbol{m}_i^{tot}(t)\right]$$

   iii. Update position and incremental rotation vectors:

   $$\boldsymbol{x}_i^{I+1}(t+\Delta t) = \boldsymbol{x}_i(t) + \left[\phi \boldsymbol{v}_i^{I+1}(t+\Delta t) + (1-\phi)\boldsymbol{v}_i(t)\right]\Delta t$$
   $$\boldsymbol{\alpha}_i^{\Delta,I+1}(t+\Delta t) = \left[\phi \boldsymbol{\omega}_i^{I+1}(t+\Delta t) + (1-\phi)\boldsymbol{\omega}_i(t)\right]\Delta t$$

4. Check for convergence:

   i. Compute errors[3] $error(\boldsymbol{v})$, $error(\boldsymbol{\omega})$, $error(\boldsymbol{x})$ and $error(\boldsymbol{\alpha}^{\Delta})$

   ii. IF $ANY(error) > TOL \Rightarrow I \leftarrow I+1$, $GOTO\,3$ (iterate)

   iii. IF $ALL\,(errors) \le TOL \Rightarrow t \leftarrow t+\Delta t$, update α_i and $GOTO\,2$ (next time step)

In this work, we adopt an explicit (forward Euler, $\phi = 0$) scheme. This is justified by the fact that we will be dealing with contacts and collisions that may be of very short duration, thereby requiring very small time-steps for a proper integration of the contact forces – which ultimately renders implicit schemes dispensable. This is common practice in the DEM literature whenever contacts are modeled through the soft-sphere approach, which intrinsically requires integration of the contact forces. The step-by-step is schematically outlined in the Algorithm 2, which is a particular case of Algorithm 1.

[3] A strategy to compute the error measures in step 4 can be found in Campello [10] [11].

Algorithm 2.

1. Initialize time variables and get initial conditions:

   $t = 0$, $\Delta t = \text{given}$, $t_F = \text{given}$, $\phi = \text{given}$

   $\boldsymbol{x}_i(0),\ \boldsymbol{v}_i(0),\ \boldsymbol{\omega}_i(0),\ \boldsymbol{\alpha}_i(0),\ \theta_i(0) = \text{given}$

2. WHILE $t \leq t_F$, loop over particles: FOR $i = 1,...,N_P$ DO

   i. Compute forces and moments at time t via equations (18), (23)-(29), (32) and (33)-(38).

   ii. Update velocities, spins, positions and incremental rotations via equations (43) and (46), we recall that $\phi = 0$.

   iii. Save updated variables and move to next time step:

   $\boldsymbol{v}_i(t) \leftarrow \boldsymbol{v}_i(t + \Delta t)$,

   $\boldsymbol{\omega}_i(t) \leftarrow \boldsymbol{\omega}_i(t + \Delta t)$,

   $\boldsymbol{x}_i(t) \leftarrow \boldsymbol{x}_i(t + \Delta t)$,

   $\boldsymbol{\alpha}_i(t) \leftarrow \boldsymbol{\alpha}_i(t + \Delta t)$,

   $t \leftarrow t + \Delta t$.

3. GOTO 2

2.5 Contact detection

Contact detection is the computational bottleneck of any DEM model. To partially overcome this issue, in this work contact detection is performed by the method so-called binning algorithm. With this technique it is possible to reduce the computational complexity (amount of time and memory requirements) from $O(N_P^2)$ to $O(N_P)$, where N_P is the total number of particles in the system. Basically, the procedure consists in decomposing the domain into cells or "bins" and sorting the particles into them, such that the neighbors searches are performed only within neighboring cells instead of within the whole domain, see Figure 13. To perform this task, let $(x_I, x_F),(y_I, y_F),(z_I, z_F)$ be the initial coordinates of the domain in the x, y, z directions where $L_x = x_F - x_I, L_y = x_F - x_I, L_z = x_F - x_I$ are the dimensions of the domain.

Figure 13 – Schematic illustration of 2D binning algorithm. Only particles in the green box will be checked for contact

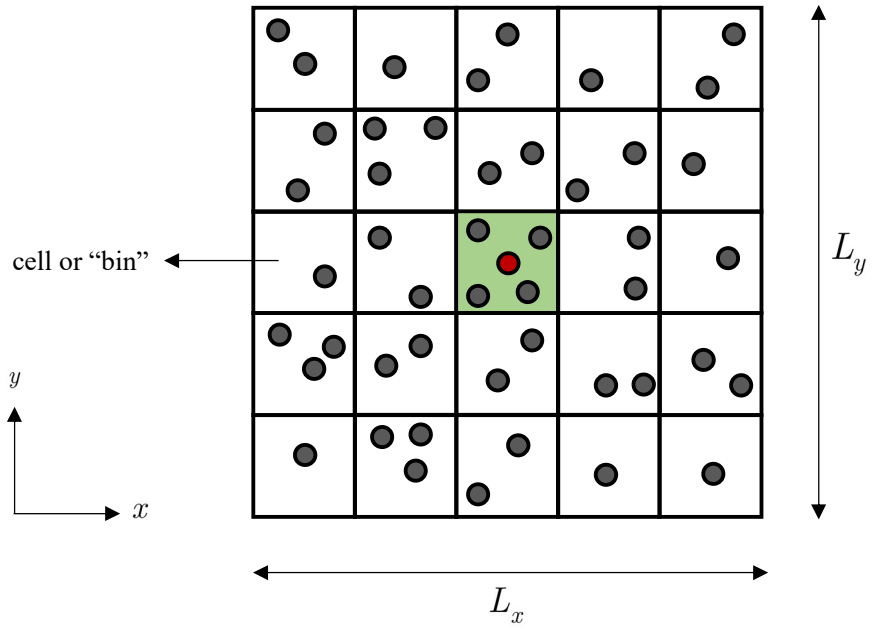

Source: Adapted from Ganeriwala [84].

To identify to which cell or "bin" a particle belongs, we proceed as follows:

$$BIN_{x_i} = \text{int}\left(\frac{x_i - x_I}{L_x}\right) \times NDIV_x + 1,$$

$$BIN_{y_i} = \text{int}\left(\frac{y_i - y_I}{L_y}\right) \times NDIV_y + 1, \tag{48}$$

$$BIN_{z_i} = \text{int}\left(\frac{z_i - z_I}{L_z}\right) \times NDIV_z + 1.$$

where $NDIV_x, NDIV_y, NDIV_z$ are the number of desired divisions or subdomains in each of the three directions and x_i, y_i, z_i are the coordinates of the particle i in the current time step. Although, with this technique the computational cost is remarkably less since it is not necessary to check the position of every particle, care must be taken to not let the cells get too small, otherwise some interactions could be missed. Additionally, the cells must be frequently updated throughout the solution in the case of the particle moves from one cell to another to identify the

new particle's position and his corresponding cell. For details, we refer the reader to Campello [10], Pöschel and Schwager [37], Zohdi [92], and Han et al. [97].

Chapter 3

Adhesion force model

The adhesion capabilities of powder particles may profoundly influence the quality of parts made by AM processes, Vallabh and Cetinkaya [98]. In this context, adhesive powder bonding has become a central issue among the various industrial sectors (e.g., automotive, aerospace) that resort to AM due to its demand for more resistant materials. Regarding the modeling of adhesion, in the small particles regime, wherein surface forces and near-field or long range interactions (i.e. electromagnetic interactions) dominate over gravitational forces and inertia effects, bonding can be satisfactorily modelled through forces derived from well-established adhesion theories, like, e.g., the classical JKR (Johnson, Kendall and Roberts [99]) theory. For heavier particles, however, typically of the order of at least a few hundred micrometers and higher, gravity and inertia dominate, and such adhesion-theory based models are no longer satisfactory. In this regime, bonding is better represented through phenomenological mass-spring models, which provide an attractive force to interacting particles whenever they come into contact, usually with stiffness given through some (oftentimes ad-hoc) constitutive equation or based on especial considerations on the problem at hand.

In this Chapter, we develop a simple (mass-spring) bond model able to capture inter-particle sticking very straightforwardly once a given bonding criterion is met. Our idea is to have a phenomenological model that is purposely simple and valid for both the small and non-small particles regimes, which may be used for general DEM applications and, in particular, for the simulation of AM processes. Also, we want to contribute with a simple strategy for the selection of proper parameter values (such as the stiffness of the bond) in such types of (mass-spring) models, since this commonly constitute an onerous (and invariably problem-dependent)

operation, often done through calibration. Moreover, differently from most mass-spring models found in the literature, here we provide a robust stability criterion (namely, the minimum overlap between particles or objects) that must be fulfilled to trigger a stable bond. The key aspects that have been derived here are analogous from those used in molecular dynamics, which are based on force potential interactions for non-conctacting particles. The model presented in this Chapter has been recently published by the authors in Campello and Quintana-Ruiz [100].

We remark that we will restrict ourselves to the central (normal) direction of the bond in this Chapter, which is the critical direction for bond formation and stability. Thus, we will leave tangential and rotational adhesion outside the scope of the Chapter (contrary to the normal adhesion, tangential and rotational bonds are very easy to be treated, and we shall turn to them when needed, in Chapter 5). Here, to damp out the particles´ lateral motion, we will resort to high friction coefficients. For the same reason, we will assume irrotational particles throughout.

3.1 Attraction and repulsion from force potentials

In several modeling approaches, such as molecular dynamics, pairwise attractive and repulsive interactions between particles of a system can be described through force potentials. For a particle i interacting with another j, if we only consider the central (normal) direction, we can say that i experiences a one-dimensional motion described by a coordinate r along this direction, in which it is both attracted to and repulsed from j, which in turn has coordinate r_j (see Figure 14).

Figure 14 – Pairwise attractive and repulsive interactions between particle *i* – *j*

Source: Author.

In these conditions, force potentials representing the motion of i have the following general form[4]

$$\psi(r) = c_1 |r - r_j|^{-m} - c_2 |r - r_j|^{-n} = c_1 \left(\frac{1}{|r - r_j|} \right)^m - c_2 \left(\frac{1}{|r - r_j|} \right)^n, \quad (49)$$

where $|r - r_j|$ is the distance between particle i and particle j, and c_1, c_2, m, n are nonnegative constants ($c_1, c_2 \geq 0$ and $m, n \geq 0$). One well-known example of such potentials are the Mie´s potentials, of which the classic Lennard-Jones potential [101] is a special case. These potentials may likewise be written as

$$\psi(r) = \frac{k_1}{-\alpha_1 + 1} |r - r_j|^{-\alpha_1 + 1} - \frac{k_2}{-\alpha_2 + 1} |r - r_j|^{-\alpha_2 + 1}, \quad (50)$$

wherein the k´s and α´s are nonnegative. Accordingly, the force acting on i due to its interaction with j reads

$$f(r) = -\frac{d\psi}{dr} = k_1 |r - r_j|^{-\alpha_1} n - k_2 |r - r_j|^{-\alpha_2} n, \quad (51)$$

$$\text{with} \quad n = -\frac{d}{dr} |r - r_j| = \frac{r_j - r}{|r - r_j|}.$$

The positive term on the right-hand side of $f(r)$ stands for the attractive part of the interaction, whereas the negative term for the repulsive one. One can see from equation (51) that the interaction is a competition between the attractive and repulsive terms, with the net effect on i alternating between attraction to j and repulsion from it, as its position r changes. A necessary and sufficient condition for the interaction to have an equilibrium configuration is that the potential have a stationary point $r = r_{eq}$, such that

$$\left. \frac{d\psi}{dr} \right|_{r_{eq}} = -f(r_{eq}) = k_1 |r_{eq} - r_j|^{-\alpha_1} - k_2 |r_{eq} - r_j|^{-\alpha_2} = 0, \quad (52)$$

from which it follows

[4] A similar expression may be written to represent the motion of j.

$$|r_{eq} - r_j| = \left(\frac{k_2}{k_1}\right)^{\frac{1}{\alpha_2 - \alpha_1}}. \tag{53}$$

In the equation (53), r_{eq} represents the equilibrium position of i with respect to j in their central direction and $d_{eq} = |r_{eq} - r_j|$ is the equilibrium distance between them. One desirable property is that the equilibrium configuration be stable in the central direction, meaning that, if the interacting members are slightly displaced from such position in the central direction, they tend to return to it once the perturbation is removed. A necessary and sufficient condition for r_{eq} to be stable is that the potential be a minimum at r_{eq}, i.e. $\psi(r)$ should be locally convex around r_{eq}:

$$\left.\frac{d^2\psi}{dr^2}\right|_{r_{eq}} = -\alpha_1 k_1 |r_{eq} - r_j|^{-\alpha_1 - 1} + \alpha_2 k_2 |r_{eq} - r_j|^{-\alpha_2 - 1} > 0, \tag{54}$$

and taking into account equation (53) gives

$$\alpha_2 k_2 \left(\frac{k_2}{k_1}\right)^{\frac{-\alpha_2 - 1}{\alpha_2 - \alpha_1}} > \alpha_1 k_1 \left(\frac{k_2}{k_1}\right)^{\frac{-\alpha_1 - 1}{\alpha_2 - \alpha_1}}, \tag{55}$$

and consequently

$$\alpha_2 > \alpha_1 . \tag{56}$$

Equation (56) establishes the requirement for stability of the interaction. It states that the exponent of the repulsive term must always exceed that of the attractive one. Moreover, there may exist a point sufficiently far from r_{eq} at which the potential changes from convex to concave. If this happens, the interaction turns to unstable therefrom, and any small perturbation that shall be given to i at that point (in the central direction) will lead to an increasing growth of its position, driving it away from r_{eq} instead of toward it. The point at which this happens is the inflection point of the potential, or critical point r_{crit}, i.e., it is the point at which

$$\frac{d^2\psi}{dr^2} = -\alpha_1 k_1 |r - r_j|^{-\alpha_1 - 1} + \alpha_2 k_2 |r - r_j|^{-\alpha_2 - 1} = 0, \tag{57}$$

from which it follows that

$$|r_{crit} - r_j| = \left(\frac{\alpha_2 k_2}{\alpha_1 k_1}\right)^{\frac{1}{\alpha_2 - \alpha_1}}. \tag{58}$$

where $d_{crit} = \left|r_{crit} - r_j\right|$ is the critical distance of the interaction, and the requirement to avoid the loss of stability is that the interaction be truncated at (or remain bounded within) the critical distance, i.e.,

$$|r - r_j| \leq d_{crit} = \left(\frac{\alpha_2 k_2}{\alpha_1 k_1}\right)^{\frac{1}{\alpha_2 - \alpha_1}}. \tag{59}$$

Equation (59) establishes a "cut off" distance for the interaction. This is very common in molecular dynamics, whose potentials often display long-range instabilities, i.e., instabilities that show up at sufficiently long distances between the interacting members. One should notice that, due to $\alpha_2 > \alpha_1$ the critical distance is always greater than the equilibrium distance, with the relation between the two being

$$d_{crit} = \left(\frac{\alpha_2}{\alpha_1}\right)^{\frac{1}{\alpha_2 - \alpha_1}} d_{eq}. \tag{60}$$

3.2 Attraction and repulsion upon contact

Interactions based on force potentials usually do not admit the occurrence of physical contact between the interacting members. However, a contact interaction under the presence of an attractive force has the very same formal structure as that from the previous section. When two objects are in contact, attractive forces may appear besides the repulsive (contact) force they experience. Such conditions can be derived from, e.g., melting (and subsequent solidification) of their surface materials, or the onset of chemical reactions that may ultimately glue or weld the bodies. In the DEM and particle dynamics realms, contact interactions are often described through the amount of overlap (or local penetration) experienced by the

particles. Models that follow such an approach are commonly referred to as soft-sphere models. If we call such overlap by δ, and substitute $\left|r - r_j\right|^{-1}$ by δ in equation (50) we arrive

$$f(\delta) = k_1 \delta^{\alpha_1} n - k_2 \delta^{\alpha_2} n\,, \tag{61}$$

where k_1 is the stiffness of the attractive part and k_2 is the stiffness of the repulsive part. Following the same arguments as from the subsection 3.1, the equilibrium configuration of the interaction, if exists, happens at an equilibrium overlap given by

$$\delta_{eq} = \left(\frac{k_1}{k_2}\right)^{\frac{1}{\alpha_2 - \alpha_1}}. \tag{62}$$

Opposed to equation (53), here the base of the exponentiation now has the stiffness of the attractive term on the numerator and that of the repulsive term on the denominator, as a consequence of the reciprocal analogy established between δ and $\left|r - r_j\right|$. By imposing δ_{eq} to be a stable configuration (similarly as done for r_{eq}) we arrive at

$$\alpha_2 > \alpha_1\,. \tag{63}$$

i.e., the exponent of the contact term must always exceed that of the adhesion term. In addition, the critical overlap of the interaction (i.e., the overlap at which it loses stability) reads

$$\delta_{crit} = \left(\frac{\alpha_1 k_1}{\alpha_2 k_2}\right)^{\frac{1}{\alpha_2 - \alpha_1}}. \tag{64}$$

where $\delta \geq \delta_{crit}$ is mandatory for an ever-stable contact-adhesion interaction, which is analogous to the expression (59). Note that the critical overlap is always smaller than the equilibrium overlap, due to $\alpha_2 > \alpha_1$, with the relation between the two being

$$\delta_{crit} = \left(\frac{\alpha_1}{\alpha_2}\right)^{\frac{1}{\alpha_2 - \alpha_1}} \delta_{eq}\,. \tag{65}$$

For overlaps smaller than the critical, the attractive-repulsive interaction must not exist and, thereby, a bond cannot be established between the contacting pair. This implies that only the contact force (responsible to pull the particles apart to a non-contact position) shall act in this

overlap range. However, if $\delta \geq \delta_{crit}$ is satisfied and a certain bonding criterion is met[5], then the attractive-repulsive interaction arises and the bond is established, in which case it will evolve into a harmonic oscillation around the equilibrium configuration δ_{eq}. Such oscillation can be viewed as the motion of a one degree of freedom mass-spring oscillator governed by the following second-order differential equation, (see also Figure 15)

$$m^*(\delta - \delta_{eq})^{\cdot\cdot} = -f(\delta - \delta_{eq}), \text{ or } m^*\ddot{x} = -f(x), \tag{66}$$

where $-f$ is the (nonlinear) restoring force provided by the spring on m^*, which is given through equation (22), and with $x = \delta - \delta_{eq}$. Note that this force is always restoring, since $\delta \geq \delta_{crit}$ is satisfied (or, equivalently, since $x \geq -(\delta_{eq} - \delta_{cr})$) by construction.

Figure 15 – Attractive-repulsive interaction as a harmonic oscillation. For $\delta_{cr} < \delta < \delta_{eq}$, the net force on m^* is attractive (which means towards δ_{eq}), whereas for $\delta > \delta_{eq}$ it is repulsive (which also means towards δ_{eq})

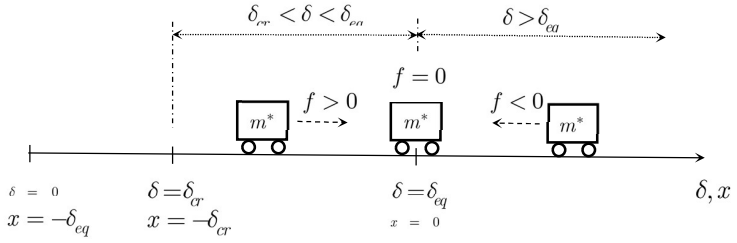

Source: Author.

Remark 3. One should notice from equations (62) and (64) that, the greater the stiffness of the adhesion or the smaller the stiffness of the contact, the greater δ_{eq} and δ_{crit} will be. Conversely, the smaller the stiffness of the adhesion or the greater the stiffness of the contact, the smaller δ_{eq} and δ_{crit} will be. Similar considerations can be drawn for the exponents: the closer the adhesion exponent is to the contact one, the greater δ_{eq} and δ_{crit} will be, and the pair will attain its equilibrium in a rather overlapped way,

[5] For bonding criterion here we mean, e.g., the temperatures of the particles reaching a certain critical temperature, like their sintering or melting temperature, or the concentration of chemical substances reaching a certain critical concentration, for significant sticking or gluing effects to develop. In the context of modeling AM processes, as we shall see later in this work, attaining the sintering temperature is the criterion to be used.

whereas the smaller the adhesion exponent is as compared to the contact one, the smaller δ_{eq} and δ_{crit} will be and the pair will its attain equilibrium in a less overlapped way.

3.2.1 Special case 1: Hertzian contact

A special case of the repulsive part of equation (61) is that of Hertzian contact (see Johnson [95]), which can be obtained by setting

$$k_2 = \frac{4}{3} E^* \sqrt{r^*} \quad \text{and} \quad \alpha_2 = \frac{3}{2}, \tag{67}$$

It follows that the equilibrium overlap is

$$\delta_{eq} = \left(\frac{k_1}{\frac{4}{3} E^* \sqrt{r^*}} \right)^{\frac{1}{3/2-\alpha_1}}, \tag{68}$$

whereas the critical overlap is

$$\delta_{crit} = \left(\frac{\alpha_1 k_1}{2E^* \sqrt{r^*}} \right)^{\frac{1}{3/2-\alpha_1}} \qquad \text{with} \qquad \alpha_1 < \frac{3}{2}, \tag{69}$$

and the relation between δ_{eq} and δ_{crit}, reads

$$\delta_{cr} = \left(\frac{2}{3} \alpha_1 \right)^{\frac{1}{3/2-\alpha_1}} \delta_{eq}. \tag{70}$$

3.2.2 Special case 2: JKR adhesion

The attractive part of equation (61) can be particularized to JKR adhesion theory (see Johnson, Kendall and Roberts [99]) by setting

$$k_1 = 2\sqrt{2\pi E^* W_{adh}} r^{*3/4} \quad \text{and} \quad \alpha_1 = \frac{3}{4}, \tag{71}$$

where W_{adh} is the so-called work of adhesion of the particles under a fluid, or the free energy change needed to separate a unit contact area of the pair in a given fluid medium. This parameter may be computed as the difference between the interfacial surface energies of the particles with the fluid and of the particles with themselves (or the particles with an object and each with the fluid), i.e.,

$$W_{adh} = \gamma_{if} + \gamma_{jf} - \gamma_{ij} \,, \tag{72}$$

It follows that the equilibrium overlap is

$$\delta_{eq} = \left(\frac{2\sqrt{2\pi E^* W_{adh}} r^{*3/4}}{k_2} \right)^{\frac{1}{\alpha_2 - 3/4}} , \tag{73}$$

whereas the critical overlap is

$$\delta_{crit} = \left(\frac{\frac{3}{2}\sqrt{2\pi E^* W_{adh}} r^{*3/4}}{\alpha_2 k_2} \right)^{\frac{1}{\alpha_2 - 3/4}} \quad \text{with} \quad \alpha_2 > \frac{3}{4}, \tag{74}$$

and the relation between δ_{eq} and δ_{crit}, reads

$$\delta_{crit} = \left(\frac{3}{4\alpha_2} \right)^{\frac{1}{\alpha_2 - 3/4}} \delta_{eq} \,. \tag{75}$$

3.3 The bond model for DEM advanced manufacturing applications

Based on equations (61) and (67) the bond model herein proposed has the following expression for the elastic part of the interaction (i.e., the spring force):

$$\boldsymbol{f}_{ij}^{bond,el} = -\frac{4}{3} E^* \sqrt{r^*} \delta_{ij}^{3/2} \boldsymbol{n}_{ij} + k_{adh} \delta_{ij}^{\alpha_{adh}} \boldsymbol{n}_{ij} \,, \tag{76}$$

where $\boldsymbol{f}_{ij}^{bond,el}$ is the bond elastic force that acts on i due to its attraction-repulsion with j, δ_{ij} is the overlap between i and j, $\boldsymbol{n}_{ij}$ is the unit vector that points from the center of i to the

center of j, k_{adh} and α_{adh} are the stiffness and the exponent of the adhesion part of the force, respectively. Let us now define a normalized overlap or deformation

$$\varepsilon_{ij} = \frac{\delta_{ij}}{r^*}. \tag{77}$$

in which r^* is the effective radius of the pair, as given in equation (19). Accordingly, the bond elastic force on i can be rewritten as

$$\begin{aligned} \boldsymbol{f}_{ij}^{bond,el} &= -\frac{4}{3}E^* r^{*2}\varepsilon_{ij}^{3/2}\boldsymbol{n}_{ij} + k_{adh} r^{*\alpha_{adh}}\varepsilon_{ij}^{\alpha_{adh}}\boldsymbol{n}_{ij}, \\ \text{or} \quad \boldsymbol{f}_{ij}^{bond,el} &= -\overline{k}_{con}\varepsilon_{ij}^{3/2}\boldsymbol{n}_{ij} + \overline{k}_{adh}\varepsilon_{ij}^{\alpha_{adh}}\boldsymbol{n}_{ij}\ , \end{aligned} \tag{78}$$

where

$$\overline{k}_{con} = \frac{4}{3}E^* r^{*2} \quad \text{and} \quad \overline{k}_{adh} = k_{adh} r^{*\alpha_{adh}}\ . \tag{79}$$

From equation (78), the equilibrium and critical deformations read

$$\varepsilon_{ij,\mathrm{eq}} = \left(\frac{\overline{k}_{adh}}{\overline{k}_{con}}\right)^{\frac{1}{3/2-\alpha_{adh}}} \text{ and } \quad \varepsilon_{ij,\mathrm{crit}} = \left(\frac{2}{3}\alpha_{adh}\frac{\overline{k}_{adh}}{\overline{k}_{con}}\right)^{\frac{1}{3/2-\alpha_{adh}}}. \tag{80}$$

and their corresponding overlaps are $\delta_{ij,eq} = \varepsilon_{ij,eq} r^*$ and $\delta_{ij,crit} = \varepsilon_{ij,crit} r^*$. The relation between $\varepsilon_{ij,eq}$ and $\varepsilon_{ij,crit}$ is

$$\varepsilon_{ij,crit} = \left(\frac{2}{3}\alpha_{adh}\right)^{\frac{1}{3/2-\alpha_{adh}}}\varepsilon_{ij,eq}\,, \quad \text{with} \quad \varepsilon_{ij,crit} < \varepsilon_{ij,eq} \tag{81}$$

Remark 4. In phenomenological mass-spring models, the value of the adhesion stiffness is usually not determined from (or directly related to) the particles′ material properties, as is, e.g., the contact stiffness in Hertzian contacts. Instead, it is often defined upon judicious considerations on the problem at hand, almost always involving some calibration—which is sometimes problematic and invariably problem-dependent. In that sense, with a previous qualitative knowledge on the material properties of the particles and on the problem under consideration, the approach proposed here may help in the selection of proper parameters values (such as, but not only, the stiffness of the

bond). Accordingly, one easy and very convenient way to obtain the value of $\overline{k}_{adh}$ (and therefrom k_{adh}) without needing to resort to calibration is to set the equilibrium deformation ($\varepsilon_{ij,eq}$) to a predefined value (e.g., a fraction of the effective radius, say, 10%, which means that the equilibrium overlap would be $\delta_{ij,eq} = 0.1r^*$) and then obtain the corresponding value through equation $(80)_1$. One important aspect that must be highlighted is that the value of $\overline{k}_{adh}$ (or k_{adh}) is not at all connected to whether the particles will or will not stick (i.e., establish a bond) once they come into contact. In this latter aspect, what makes the particles stick (i.e., establish the bond) is having $\varepsilon_{ij} \geq \varepsilon_{ij,crit}$ while at the same time fulfilling the bonding criterion (like having the particles′ temperatures attaining a certain critical temperature, as said before), irrespective of $\overline{k}_{adh}$ (or k_{adh}).

According to Hertz's contact theory, the maximum penetration of two contacting spheres of approaching velocity $\boldsymbol{v}_{ij,rel}$ (i.e., pre-collision relative velocity) in the absence of external forces is

$$\delta_{ij,\max} = \left(\frac{15 m^* v_{ij,\mathrm{rel}}^2}{16 E^* \sqrt{r^*}} \right)^{\frac{2}{5}}, \tag{82}$$

which follows from integration of the differential equation that describes their relative motion. By enforcing $\delta_{ij,\max} \geq \delta_{ij,crit}$, we have

$$v_{ij,\mathrm{rel}} \geq \left[\left(\frac{16 E^* \sqrt{r^*}}{15 m^*} \right)^{\frac{2}{5}} \left(\frac{\alpha_{adh} k_{adh}}{2 E^* \sqrt{r^*}} \right)^{\frac{1}{3/2-\alpha_{adh}}} \right]^{\frac{5}{4}}. \tag{83}$$

The equation (83) is a necessary (although not sufficient) condition for the bond to be established. Interestingly, for particles consisted of the same mass-density $\rho_i = \rho_j = \rho$, it reduces to

$$v_{ij,rel} \geq \sqrt{\frac{E^*}{5\pi\rho}} \left[\left(\frac{2}{3} \alpha_{adh} \right)^{\frac{1}{3/2-\alpha_{adh}}} \varepsilon_{ij,eq} \right]^{5/4} = \sqrt{\frac{E^*}{5\pi\rho}} \varepsilon_{ij,crit}^{5/4}, \tag{84}$$

which is independent of the particles' radii for a given $\varepsilon_{ij,eq}$.

3.3.1 Viscous dissipation upon bonding

Additionally to the elastic force given by equation (76) a viscous term is introduced in our model, which essentially represents a damper in the mass-spring oscillator, allowing the particles to dissipate their energy in the central direction once the bond is formed. Considering a damper of damping constant d^*, we write this dissipative term as

$$\boldsymbol{f}_{ij}^{bond,d} = -d^*\dot{\delta}_{ij}\boldsymbol{n}_{ij} , \tag{85}$$

where $\dot{\delta}_{ij}$ is the relative velocity of the particles in their central direction. In analogy with the equation of motion of a linear mass-spring-damper oscillator of mass m^*, stiffness k^* and damping d^* (see Figure 16), we take

$$d^* = 2\xi^{bond}\sqrt{m^*k^*} , \tag{86}$$

in which ξ^{bond} is the damping rate of the oscillation, which is a model parameter that must be given. For the spring stiffness that enters the above equation, we take

$$k^* = -\frac{d}{d\delta_{ij}} f_{ij}^{bond,el} = 2E^*\sqrt{r^*}\delta_{ij}^{1/2} - \alpha_{adh}k_{adh}\delta_{ij}^{\alpha_{adh}-1}, \tag{87}$$

where $f_{ij}^{bond,el} = \left\| \boldsymbol{f}_{ij}^{bond,el} \right\|$ is the magnitude of the force on the spring. We note that equation (87) renders an ever-positive stiffness for $\delta > \delta_{crit}$ (since the force on the spring is always restoring in the stable range of the interaction), and this guarantees that the square root in equation (86) always exists when the bond is established. We draw the attention to the fact that, for a spring model to work, the viscous term must be able to stop the particles´ relative motion very rapidly once the bond is established. If this is not accomplished, the particles will initiate their oscillation around δ_{eq} but it may happen that the corresponding amplitude is high enough (depending on the collision´s initial conditions) to surpass the stable range of the interaction. In such case, the particles will acquire a motion with $\delta < \delta_{crit}$ at the end of their first vibration period, which will consequently break the bond and therefrom drive them apart shortly. The simplest way to enforce such requirement is to adopt a very high damping ratio in the model (ideally, $\xi^{bond} \to 1$).

Figure 16 – Schematic linear mass-spring-damper oscillator

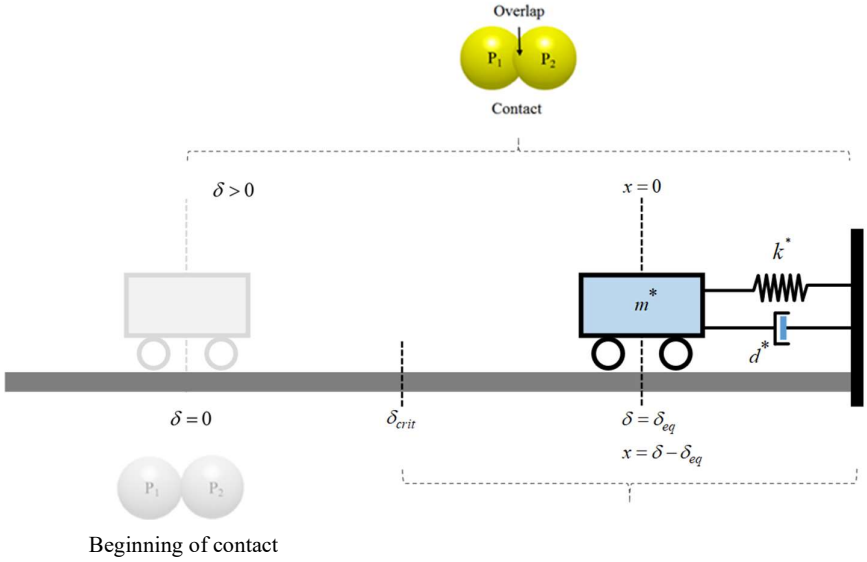

Source: Author.

3.3.2 Total interaction force

From the above considerations, the total interaction force in this model reads

$$\boldsymbol{f}_{ij}^{tot} = \begin{cases} \boldsymbol{f}_{ij}^{con,el} + \boldsymbol{f}_{ij}^{con,d}, & IF\ \delta \leq \delta_{crit} \\ \boldsymbol{f}_{ij}^{bond,el} + \boldsymbol{f}_{ij}^{bond,d}, & IF\ \delta > \delta_{crit} \end{cases} \quad \text{and the bond criterion is met.} \tag{88}$$

where $\boldsymbol{f}_{ij}^{con,el}$ is the contact force in case there is no bonding, herein given by purely Hertzian expression corresponding to the first term of equation (18), and $\boldsymbol{f}_{ij}^{con,d}$ is the dissipative (viscous damping) and second term of the same equation, given by

$$\boldsymbol{f}_{ij}^{con,d} = -d^{con}\dot{\delta}_{ij}\boldsymbol{n}_{ij} \quad \text{with} \quad d^{con} = 2\xi^{con}\sqrt{2E^{*}m^{*}\sqrt{r^{*}}\delta_{ij}^{1/4}}\,. \tag{89}$$

Here ξ^{con} is the corresponding contact damping rate (i.e., the rate for purely contact interactions), which must be given. At the implementation level, similarly as it happens for damped, purely contact interactions, one should always check the consistency of the sign of the total interaction force. Accordingly, for $\delta_{ij} \leq \delta_{ij,crit}$, if $\boldsymbol{f}_{ij}^{tot} \cdot \boldsymbol{n}_{ij} > 0$ then one must set

$\boldsymbol{f}_{ij}^{tot} = \boldsymbol{0}$, as to avoid an attractive contact force, which obviously makes no sense. For the same reason, for $\delta_{ij} > \delta_{ij,crit}$, if $\delta_{ij} > \delta_{ij,eq}$ and $\boldsymbol{f}_{ij}^{tot} \cdot \boldsymbol{n}_{ij} > 0$, then $\boldsymbol{f}_{ij}^{tot} = \boldsymbol{0}$, whereas if $\delta_{ij} < \delta_{ij,eq}$ and $\boldsymbol{f}_{ij}^{tot} \cdot \boldsymbol{n}_{ij} < 0$, then $\boldsymbol{f}_{ij}^{tot} = \boldsymbol{0}$ (this ensures an ever-restoring total interaction force for the bond), see Figure 15. For more details we refer the interested reader to Campello and Quintana-Ruiz [100].

Remark 5. In the discrete element method formulation of Chapter 2, when adhesion is considered, the sum of $\boldsymbol{f}_i^{adh}$ with $\boldsymbol{f}_i^{con}$ in equation (17) must be substituted by $\boldsymbol{f}_{ij}^{tot}$ from equation (88). Moreover, the bonding between particles and flat rigid surfaces (or "walls") may be considered as a special case of that between particles. Accordingly, and as we stated in Remark 1, rigid surfaces can be treated as particles with infinite radius, stiffness and mass. By setting $r_j \to \infty$, $E_j \to \infty$ and $m_j \to \infty$ in the expressions (19) and (22), one arrives at $r^* = r_i$, $E^* = E_i$ and $m^* = m_i$.

3.4 Validation and illustration

Let us illustrate the outcomes of the above bond model by analyzing a few simple numerical examples. First, we show some validation results and parametric studies on the interaction between two particles. Then, we analyze two more general, multi-particle examples. As it was previously mentioned, in this Chapter we will restrict ourselves to the central (normal) direction of the bond, while the tangential and rotational bonds will be included in the examples of Chapter 5. For time integration, we adopt the explicit (forward Euler) version of the solution scheme, as presented in subsection 2.4.1 (Algorithm 2). We select the time step size according on the following criterion:

$$\Delta t \leq \frac{\delta t_{con}}{20}, \qquad \delta t_{con} \cong 2.87 \left(\frac{m^{*2}}{r^* E^{*2} v_{rel}} \right)^{1/5}, \tag{90}$$

where δt_{con} is the duration of the shortest possible contact or collision for the problem at hand and v_{rel} is the relative (approaching) velocity of the corresponding contacting pair in the pair´s

central direction immediately before the contact or collision is initiated. This is based on Hertz's contact theory (see Johnson [95]) and, according to our experience, allows for a good accuracy in the computation of the contact forces. Contact detection is performed through the binning algorithm, presented in subsection 2.5.

3.4.1 Bonding of two particles in central collision

Let us consider two same-sized particles with radii $r = 1$ mm approaching each other at a relative (central) velocity of 2.6 m/s (this is slightly greater than the bonding velocity that follows from equation (83) and, thereby, should trigger the bond). The mass-density of the particles is $\rho = 2000$ kg/m^3 and their elastic properties are $E = 1$ GPa and $\nu = 0$, along with $\xi^{con} = 0$ for the purely-contact part of the interaction (i.e., perfectly elastic contact). The equilibrium deformation is set to $\varepsilon_{ij,eq} = 0.1$ (which means that the equilibrium overlap is $\delta_{ij,eq} = 0.00005$ m), from which the adhesion stiffness $k_{adh} = 1.05 \times 10^5$ N/m follows (the adhesion exponent adopted is $\alpha_{adh} = 1$). The time-step size adopted in the time numerical integration was $\Delta t = 5 \times 10^{-7}$ s, whereas the final simulation time was $t = 0.005$ s. In Figure 17, we plot the evolution of the particles´ overlap in time for different values of ξ^{bond} (only the relevant time interval is represented).

Figure 17 – Bonding of two particles in a central collision

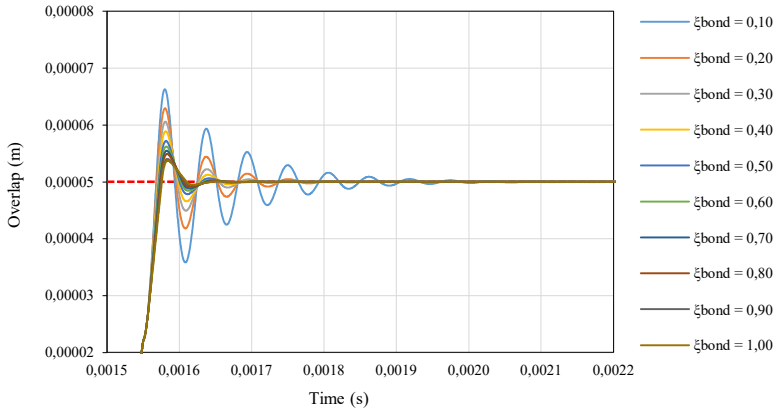

Source: Author.

We observe that not only the bond is established for all values of ξ^{bond}, but also the overlap converges to the predefined equilibrium overlap $\delta_{ij,eq}$ irrespective of the value of ξ^{bond}

in all cases. We can see, too, that for lower values of ξ^{bond} a greater amplitude around the equilibrium overlap is observed in the earlier stages of the interaction, which then progressively diminishes towards a static "stick" configuration. One should be careful with such great amplitudes because, if exaggerated, they may overcome the stable range of the interaction and thereby trigger instabilities and, in the extreme case, even lead to a loss of contact. This may be easily overcome in the model by adopting a sufficiently high value for ξ^{bond}, which will damp the oscillation from the beginning. In Figure 18, we investigate the outcomes of a central collision in terms its coefficient of restitution (e) for varying mass densities of the particles through a parametric study. The geometrical and material data are the same as from the previous example (except for the mass density), as well as the time-step size and the final simulation time. A critically damped bond ($\xi^{bond} = 1$) is assumed for all cases. As we see from Figure 18a, the particles stick to each other irrespective of their mass density. For each mass-density case, the necessary impact velocity for the bond to be formed, or "bonding velocity", attains a different value, which follows from equations (83) or (84) and is depicted in Table 1.

Results from Figure 18b, shows the coefficient of normal restitution against the normalized impact velocity (the normalizer here is the bonding velocity of the case), wherein it can be seen that all graphs virtually collapse to one. There is always perfect restitution $(e = 1)$ for impact velocities smaller than the bonding velocity, and always perfect sticking $(e = 0)$ for impact velocities greater than the bonding velocity, irrespective of the particles´ mass-density. Results for other values of elastic properties and bond model parameters (i.e., the bond's exponent and equilibrium deformation) are qualitatively the same and will not be reported here for conciseness.

Figure 18 – Restitution coefficient *e* plotted as a function of the impact velocity

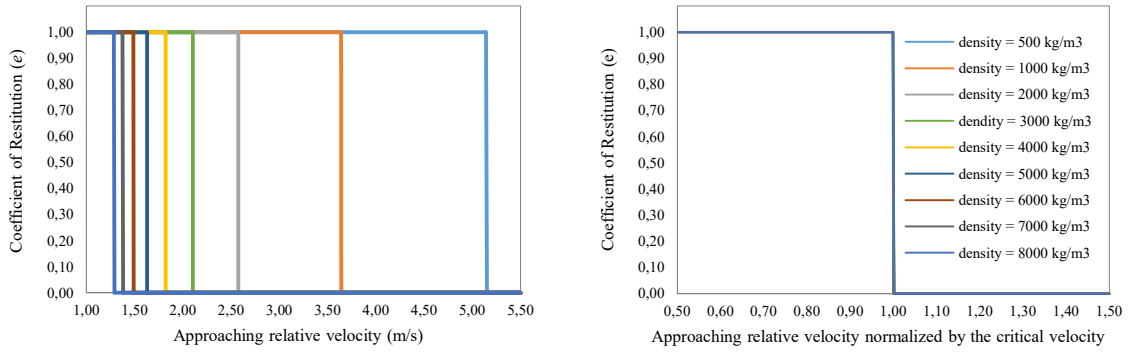

(a) (b)

Source: Author.

Table 1. Bonding velocity for several mass-density cases

Density (kg/m^3)	Bonding velocity (m/s)
500	5.15
1000	3.64
2000	2.57
3000	2.10
4000	1.82
5000	1.63
6000	1.49
7000	1.38
8000	1.29

Source: Author

3.4.2 Deposition of a droplet of particles onto a rigid surface

This example is taken from Campello [11] and Zohdi [12], wherein an electrically charged particle droplet is driven to (and deposited onto) a rigid surface due to the action of an attractive electric field. Here, we will consider it by replacing the electric field by a driving droplet velocity, and expect that upon impact the deposition be sustained entirely by the bond model – provided that the droplet is given enough kinetic energy as to activate the bonds. The droplet is spherical with diameter 1.2 cm, with its center being located at $(x, y, z) = (0, 0, 0)$ at $t = 0$. The particles are randomly placed within it (we use the random sequence addition algorithm of Campello and Cassares [102]) and have their radii following a Gaussian distribution with mean $\overline{r} = 0.25$mm and standard deviation (std. dev.) $\sigma_R = 0.05$mm (the distribution is truncated at three std. dev. from the mean, such that all radii fall in the interval [0.1mm, 0.4mm]). The rigid surface is flat and located at coordinate $X = +4$ cm. The problem is illustrated in Figure 19, top left. We want to investigate the outcomes of the deposition at different levels of impact energy. To this aim, a circle of diameter $D = 1.2$cm and center at $C = (4, 0, 0)$ cm is defined as a target region for deposition. The following figures of merit are defined to assess the process (wherein N_P is the total number of particles within the droplet):

i. mean distance of the particles w.r.t. the center of the target region at the end of the deposition:

$$\bar{d} = \frac{1}{N_P}\sum_{i=1}^{N_P}\sqrt{y_i^2 + z_i^2}\ ; \tag{91}$$

ii. mean height of the particles w.r.t. the rigid surface at the end of the deposition (i.e., difference between coordinate $X = +4\,\text{cm}$ of the surface and coordinates $\boldsymbol{x}_i$ of the particles):

$$\bar{h} = \frac{1}{N_P}\sum_{i=1}^{N_P}(X - x_i)\,; \tag{92}$$

iii. percent deposition within the target region, defined as the number of particles that satisfy the condition $d_i \leq 0.5D$ with $d_i = \sqrt{y_i^2 + z_i^2}$ and are bonded to the surface and/or to other particles, divided by the total number of particles N_P. Other data are as follows:

- particles′ elastic properties and mass-density: $E = 1$ GPa, $\nu = 0$ and $\rho =$ 2000 kg/m^3;
- particles′ friction coefficients: $\mu =$ 0.2 (particle-particle) and $\mu =$ 1.0 (particle-rigid surface);
- particle′s damping ratios: $\xi^{con} = 0$ and $\xi^{fric} = 0.9$;
- particles′ bond parameters: $\alpha_{adh} = 1$, $\varepsilon_{eq} = 0.1$ and $\xi^{bond} = 0.9$;
- total number of particles within the droplet: $N_P =$ 1650 (packing ratio is roughly 0.15);
- gravity is not considered;
- the time-step adopted was: $\Delta t = 2.0\times10^{-7}$ s.

From equations (83) or (84) the necessary impact velocity for bonds to form between particles is about $v_{rel} \geq 2.6$ m/s, whereas for bonds between particles and the rigid surface it is about $v_{rel} \geq 7.3$ m/s. Based on this estimates, we consider the following cases of droplet velocity: $v_{drop} =$ 1, 2, 4, 8 and 16 m/s. Figure 19 depicts a sequence of snapshots of the system's configuration at selected time instants as obtained with our simulation for the case with $v_{drop} = 8$ m/s. As it can be seen, once the droplet hits the surface the particles start to agglomerate (as a result of activated bonds) and form a rather coherent layer in the shape of a spherical cap. The deposition is successful, in the sense that most of the particles adhere (both

to the surface and to each other) and remain bounded within the target region. Figure 20 shows the results for the other velocity cases (only their final configurations are depicted for conciseness). One can see that the deposition is successful for $v_{drop} \geq 8$ m/s and unsuccessful otherwise. To compute the figures of merit, for each velocity case we performed ten simulations, each corresponding to a different initial droplet (the droplets are all of the same size and consisted of the same particles, but differ from each other w.r.t. the particles´ positions, which are random). Expressions (91)-(92) were then computed for each run and in the end the results were averaged for the case. The upshots are summarized in Table 2.

Figure 19 – Deposition of a droplet of particles onto a rigid surface. Problem definition (top left) and sequence of snapshots at selected time instants as obtained for the case with $\boldsymbol{v}_{drop}$ = 8 m/s

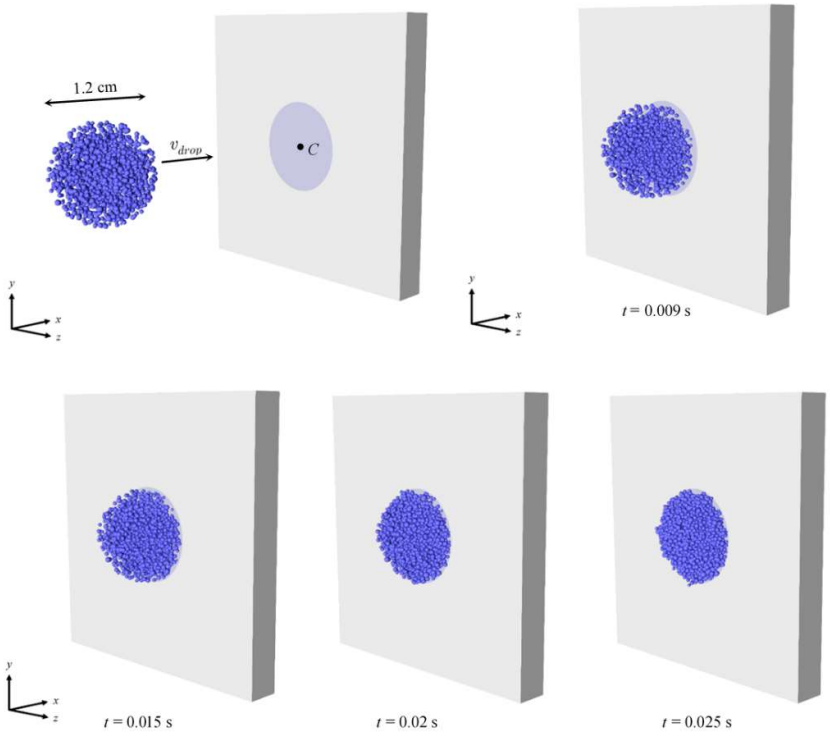

Source: Author.

As we can see in Figure 20, (i) for $v_{drop} \leq 2$ m/s, since the particles are not able to bond but instead rebound after impact, the mean distance and mean height are quite large, and the percent deposition is zero; (ii) for $v_{drop} = 4$ m/s, since some particles are able to stick to others (but not to the surface) and thereby form chunks that likewise rebound and spread laterally, the mean distance and mean height are still large (but smaller than before), and the

percent deposition is minimal; (iii) $v_{drop} \geq 8$ m/s, since all bonds are activated, nearly full deposition is seen and the mean distance and mean height are markedly smaller, with the percent deposition being virtually 100%.

Figure 20 – Final configurations. From top to down: $\boldsymbol{v}_{drop}$ = 1, 2, 4, 8 and 16 m/s. The final time instant for each case are 0.1 s, 0.08 s, 0.06 s, 0.04 s and 0.02 s, respectively

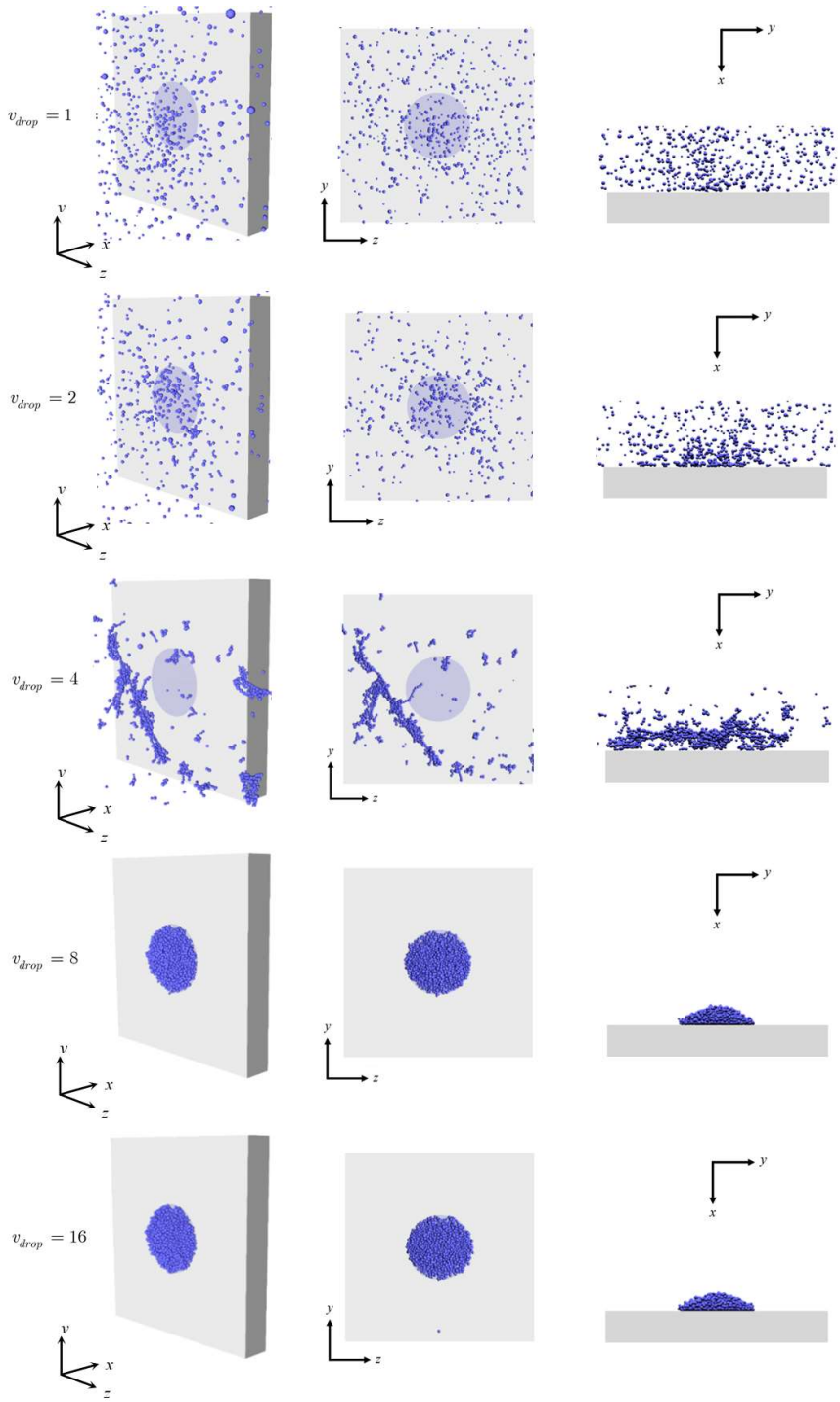

Source: Author.

We draw the attention to the very small values of the std. dev. in all figures and cases. This is an indication that the model, though applied to randomly different (yet generated from the same parameters) droplets, renders results that are satisfactorily repeatable. If we compute the coefficient of variation for each case (i.e., the ratio of the std. dev. to the mean, which provides a non-dimensional measure of dispersion of the results or, in other words, a zeroth-order estimate of the extent to which variabilities in the input parameters propagate to the output results), we will find, too, very small values, which further supports this conclusion. The computation time required for a typical simulation in this analysis is about 2 min per each 0.01s of the problem´s duration, in a standard, single processor laptop computer (at 2.00 GHz) with no parallelization nor usage of the graphics processing unit.

Table 2. Figures of merit (std. dev. in parentheses). Results were computed for the final time instant of the corresponding case

Drop velocity	Final time instant	Mean distance $\bar{d}$	Mean height $\bar{h}$	Percent deposition within target region
1 m/s	0.1s	5.12 cm (0.25 cm)	1.65 cm (0.26 cm)	0% (0)
2 m/s	0.08s	4.68 cm (0.13 cm)	1.96 cm (0.08 cm)	0% (0)
4 m/s	0.06s	2.41 cm (0.16 cm)	0.69 cm (0.04 cm)	9.8% (0.9%)
8 m/s	0.04s	0.34 cm (0.004 cm)	0.11 cm (0.01 cm)	99.3% (0.3%)
16 m/s	0.02s	0.35 cm (0.005 cm)	0.10 cm (0.003 cm)	99.1% (0.1%)

Source: Author

3.4.3 Particle jet deposition

This is a variation from the previous example in the sense that we now consider a jet of particles (instead of a droplet) with a screening (downwards) velocity, as illustrated in Figure 21, top left. We want to assess the deposition features (sharpness, compactness and dimensions of the deposited layer) for varying levels of impact energy and screening speeds. The jet has length L = 10 cm and square cross-section 1 cm × 1 cm, being consisted of $N_P = 5000$ particles of the same size, material properties and bond parameters as from the previous example, randomly generated. Accordingly, we set the jet velocity to $v_{jet} = 8$ m/s (as to guarantee bonding with the surface) and consider the following cases for the screening speed:

v_{screen} = 2, 4, 5, 8 and 10 m/s. Figure 21 depicts a sequence of snapshots of the system's configuration at selected time instants as obtained with our simulation for the case with v_{screen} = 4 m/s. As it can be seen, as the jet hits the surface, the particles begin to agglomerate and form a well-defined layer that evolves in the screening direction.

The deposition is successful, in the sense that most of the particles adhere (both to the surface and to each other) and nicely fill in the screened area. Figure 22 shows the results for the other cases of screening speeds (only their final configurations are depicted for conciseness). Likewise the previous case, for each case of screening speed, we performed ten simulations, each corresponding to a different initial jet (the jets are all of the same size and consisted of the same particles, but differ from each other w.r.t. the particles´ positions, which are random).

Figure 21 – Particle jet deposition. Problem definition (top left) and sequence of snapshots at selected time instants as obtained for the case with $\boldsymbol{v}_{screen}$ = 4 m/s

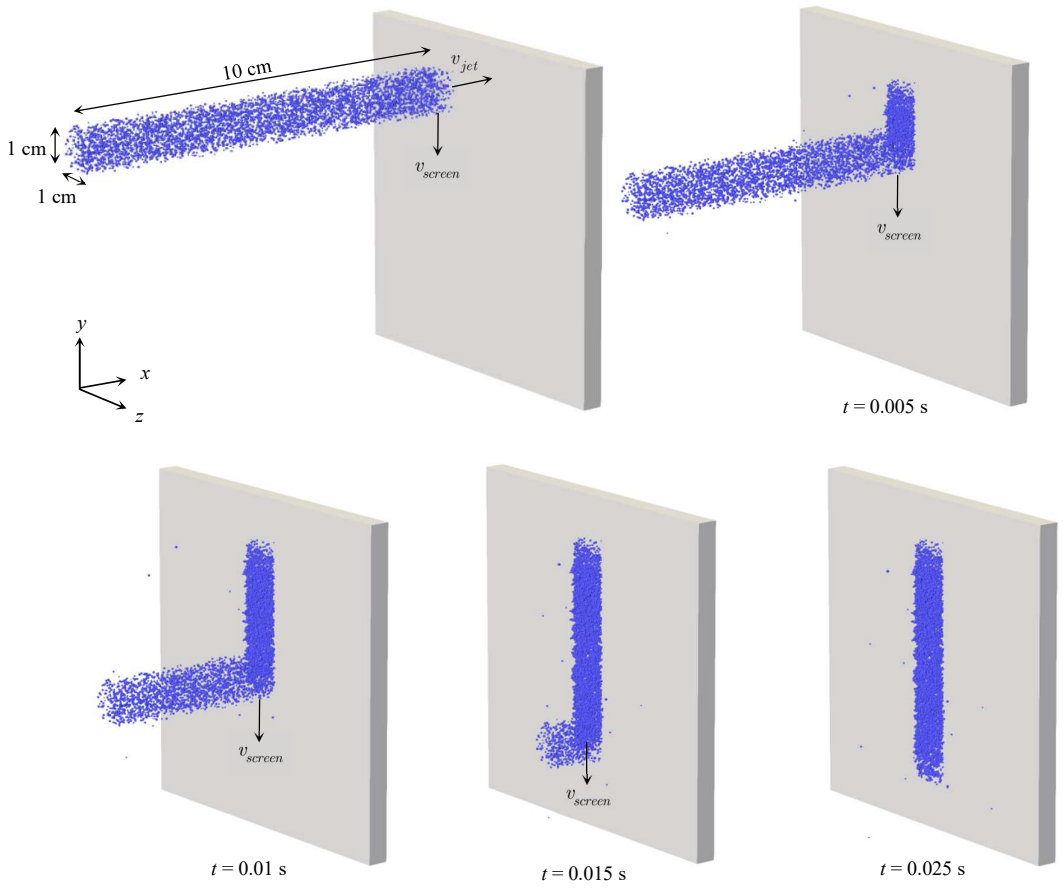

Source: Author.

Figure 22 – Particle jet deposition. From left to right: v_{screen} = 2, 4, 5, 8 and 10 m/s. The time instant are 0.1 s, 0.08 s, 0.07 s, 0.04 s and 0.03 s, respectively

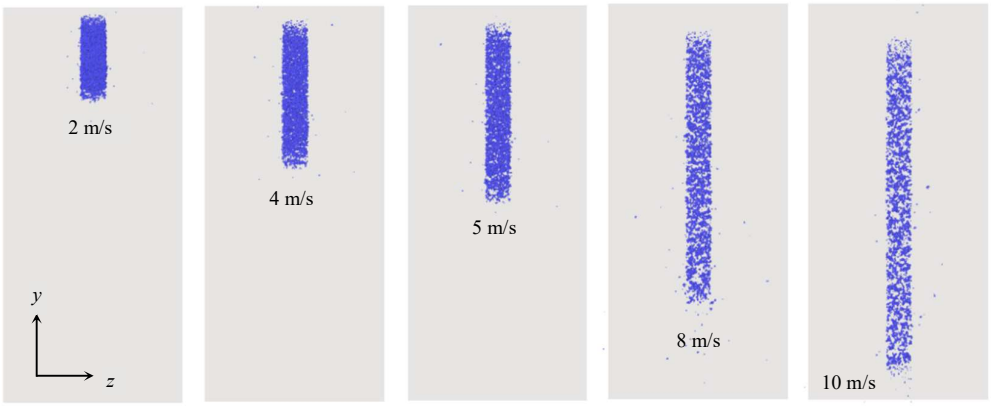

Source: Author.

Table 3. Figures of merit (std. dev. in parentheses). Results were computed for the final time instant of the corresponding case

Screening velocity	Final time instant	Mean width	Mean length	Mean height
2 m/s	0.1s	1.05 cm (0.01 cm)	3.29 cm (0.04 cm)	0.13 cm (0.007 cm)
4 m/s	0.08s	1.04 cm (0.02 cm)	5.85 cm (0.07 cm)	0.09 cm (0.006 cm)
5 m/s	0.07s	1.03 cm (0.03 cm)	7.11 cm (0.07 cm)	0.09 cm (0.007 cm)
8 m/s	0.04s	1.02 cm (0.04 cm)	10.93 cm (0.11 cm)	0.05 cm (0.0005 cm)
10 m/s	0.03s	1.02 cm (0.04 cm)	13.42 cm (0.12 cm)	0.05 cm (0.0005 cm)

Source: Author

The figures of merit were computed for each run and in the end the results were averaged for the case. Table 3 summarizes the results. As general conclusions, we observe that: (i) the mean width is practically the same for all cases, with a remarkably small std. dev. all over; (ii) the mean length increases with the screening speed, as expected, but likewise displays a very small std. dev. in all cases; and (iii) the mean thickness decreases with increasing screening speeds, as also expected, and the std. dev. once again remains very small. Overall, we find the results to be qualitatively plausible and quantitatively very well repeatable. By means of simulation set-ups of the type as shown here, many particle deposition processes may be studied, such as industrial coating technologies and material jetting techniques in additive manufacturing. General trends can be identified, the relevance of certain parameters may be ascertained and what-if scenarios may be drawn, thereby helping to consistently improve

process performance. The computation time required for a typical simulation in this analysis is about 2 min per each 0.01s of the problem´s duration, in a standard, single processor laptop computer (at 2.00 GHz) with no parallelization nor usage of the graphics processing unit.

Chapter 4

Consideration of thermal effects

In this Chapter, we develop our strategy to incorporate thermal effects into the DEM formulation of Campello [9] [10] [11]. It follows the same general framework as that from Zohdi [12] [13], but has some distinguished features: (i) we adopt a fully consistent stick–slip friction model for arbitrarily rotational particles (this is the friction type that is most frequently observed in dry granular media, Duran [14]) and (ii) we take rolling resistance as well as (iii) convective and radiative effects into account. Another distinction is that our model makes use of contact and heat conduction parameters that are well grounded on physical models, in contrast to Zohdi's model, which adopts general parameters that, although formally competent, require problem-dependent calibration for proper parameter values. The thermo-mechanical model presented in this Chapter is a step forward of a previous work published by the authors, see Quintana-Ruiz and Campello [103].

4.1 First law of thermodynamics

Following the same discrete particle approach as for the mechanical fields, we assume here that the temperatures are uniform within the particles (ignoring temperature gradients). This corresponds to a lumped thermal model and is valid as long as the Biot number is small[6] (smaller than one). The Biot number for spheres is the quotient between the particle volume (V) and the particle surface area (A_s):

[6] It refers to when the surface area of a body is large enough in relation to its interior volume as to allow for a rapid exchange of heat with the surrounding medium – which is the case here.

$$\frac{V}{A_s} = \frac{\frac{4}{3}\pi r_i^3}{4\pi r_i^2} = \frac{r_i}{3}. \tag{93}$$

As we are interested here in the simulation of AM processes, which tipically employs small particles (of the order of a few microns or mostly fractions of millimeters), the Biot's number will be always small (much smaller than one).

From the first law of thermodynamics, the energy balance for the i^{th} particle reads

$$\dot{K}_i + \dot{U}_i^{int} = P_i^{ext} + \dot{Q}_i^{cond} + \dot{Q}_i^{conv} + \dot{Q}_i^{rad} + \dot{Q}_i^{ext}, \tag{94}$$

where K_i is the particle´s kinetic energy, U_i^{int} is the particle´s internal (or stored) (mechanical plus thermal) energy, P_i^{ext} is the mechanical power due to the external forces, Q_i^{cond} is the particle´s heat flow due to conduction (amount of heat that flows through the particle by conduction upon contact with other particles and objects), Q_i^{conv} is the particle´s heat flow due to convection by its surroundings (amount of heat that flows from or to the particle due to convection by the surrounding environment), Q_i^{rad} is the particle´s heat flow due to radiative effects and Q_i^{ext} is the particle´s heat input from external devices (e.g., fire nozzles, burners, laser beams, electric currents, etc.). The kinetic energy is given by

$$K_i = \frac{1}{2} m_i \boldsymbol{v}_i \cdot \boldsymbol{v}_i, \tag{95}$$

with its time derivative being

$$\dot{K}_i = m_i \dot{\boldsymbol{v}}_i \cdot \boldsymbol{v}_i. \tag{96}$$

Consistent with the DEM assumptions, the particle´s deformations (due to contacts with other particles and objects) are assumed to be very small, such that the mechanical part of the internal or stored energy is negligible. There remains only its thermal part, which means that

$$U_i^{int} = m_i C_i \theta_i, \tag{97}$$

where C_i is the specific heat of the particle (heat capacity per unit mass, which is assumed constant[7]) and θ_i is the particle´s temperature. The time derivative of equation (97) yields

[7] In the presence of phase transformation, this value can vary as a function of temperature and phase, as it will be seen in Chapter 5.

$$\dot{U}_i^{int} = m_i C_i \dot{\theta}_i \,, \tag{98}$$

The power due to external forces is

$$P_i^{ext} = \boldsymbol{f}_i^{tot} \cdot \boldsymbol{v}_i \,, \tag{99}$$

where $\boldsymbol{f}_i^{tot}$ is the total force vector acting on the particle, which is the sum of all forces on the right-hand side of equation $(17)_1$. From the balance of linear momentum on the particle, one has $m_i \dot{\boldsymbol{v}}_i = \boldsymbol{f}_i^{tot}$, and if this is inserted into equation (96) it follows that

$$\dot{K}_i = P_i^{ext} \,, \tag{100}$$

implying that these two terms cancel out each other in equation (94). As a consequence, and taking equation (98) into account, the energy balance of the particle reads

$$m_i C_i \dot{\theta}_i = \dot{Q}_i^{cond} + \dot{Q}_i^{conv} + \dot{Q}_i^{rad} + \dot{Q}_i^{ext} \,. \tag{101}$$

This expression is formally identical to equation (17), except that it is now a scalar equation. It is the governing equation for the system´s thermal field. Each one of its heat power (or heat flow per unit time) contributions is described in the subsections that follow.

4.2 Heat power due to conduction

Heat flow through conduction takes place whenever the particle contacts another particle or object, see Figure 23. It is a function of the temperature gradient between the contacting pair, the contact area between the pair and the pair´s individual thermal conductivities. To model this phenomenon, we follow the discrete form of Fourier´s law for conduction across interfaces, and adopt the following expression for the conduction heat flow on particle i :

$$\dot{Q}_i^{cond} = \sum_{j=1}^{N_i^C} \dot{Q}_{ij}^{cond} \,, \quad \text{with} \quad \dot{Q}_{ij}^{cond} = k_{ij} \frac{\theta_j - \theta_i}{\left\| \boldsymbol{x}_j - \boldsymbol{x}_i \right\|} A_{ij}^C \,, \tag{102}$$

where Q_{ij}^{cond} is the conduction heat flow on particle i due to its contact with particle (or object) j, N_i^C is the number of particles and objects that are in contact with particle i, k_{ij} is the effective thermal conductivity of the $i-j$ contacting pair (which is a function of the individual thermal conductivities of i and j and, possibly, the thermal resistance at their interface, as

shown shortly below) and A_{ij}^{C} is the contact area between the pair. This latter is computed by assuming that the area is circular with radius a_{ij}, which in turn may be obtained through solution of the following geometrical problem (see Figure 24) which gives:

Figure 23 – Particle-particle heat conduction

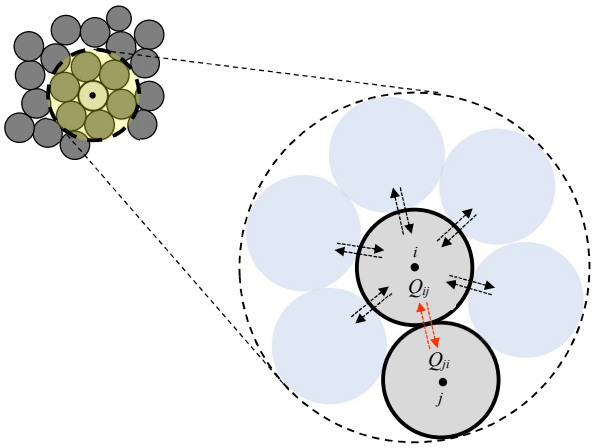

Source: Author.

Figure 24 – Geometrical representation of two contacting particles allowing for the solution to obtain L_i

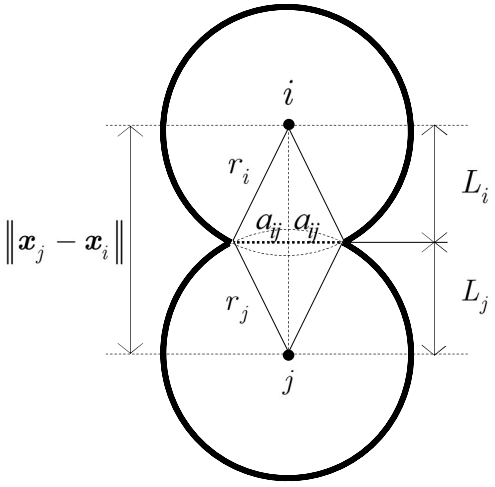

Source: Author.

$$\begin{aligned} a_{ij}^2 + L_i^2 &= r_i^2 \\ a_{ij}^2 + L_j^2 &= r_j^2 \\ L_i + L_j &= \|\boldsymbol{x}_j - \boldsymbol{x}_i\|, \end{aligned} \tag{103}$$

$$\begin{aligned} L_i &= \frac{1}{2}\left(\|\boldsymbol{x}_j - \boldsymbol{x}_i\| - \frac{r_j^2 - r_i^2}{\|\boldsymbol{x}_j - \boldsymbol{x}_i\|}\right) \quad \Rightarrow a_{ij}^2 = r_i^2 - L_i^2 \Rightarrow \\ A_{ij}^C &= \pi a_{ij}^2 = \pi(r_i^2 - L_i^2). \end{aligned} \tag{104}$$

We draw the attention of the reader to the fact that Hertz contact theory predicts $A_{ij}^C = \pi(r^* \delta_{ij})$ (with r^* and δ_{ij} given respectively by equations (19) and (20)) but this is valid only for very small overlaps. Expression (104), on the contrary, is general and holds for any overlap magnitude. The pair's effective thermal conductivity may be computed from

$$\frac{r_i + r_j}{k_{ij}} = \frac{r_i}{k_i} + \frac{r_j}{k_j}, \tag{105}$$

where k_i and k_j are the thermal conductivities of the materials of i and j, respectively, and r_i and r_j their radii. If the particles have adsorbed material onto their surfaces, one extra term may be added to the above expression to account for the corresponding thermal resistance (namely, the term would be t_{mat}/k_{mat}, where t_{mat} is the material's thickness and k_{mat} its corresponding thermal conductivity). Expression (105) is based on the assumption that the individual thermal resistances of the contacting pair may be summed up to provide the effective resistance of the pair, the reciprocal of which furnishes the pair's effective conductivity.

An alternative approach is the so-called thermal pipe network model, proposed by Feng et al. [104], which is a simplified version of the DTEM model (see Feng et al. [65]). Here, the model is based on the thermal conductances of the contacting particles (rather than on their thermal conductivities) and consider a formation of a "heat pipe-network" between the particle centre with their contact interface associated with the particle. Accordingly, if α_i is the angle (measured from the particle's center) that defines the particle's contact interface with another particle or object, the thermal conductance κ_i of the particle may be satisfactorily approximated by

$$\kappa_i \cong \frac{\pi k_i}{-\ln \alpha_i + 3/2 + \alpha_i^2/36 + \alpha_i^4/2700}. \tag{106}$$

This result is based on the two-dimensional solution of the steady-state heat problem within a 2D circular domain to which heat is provided across an interface defined by α_i. A similar expression holds for the thermal conductance of particle j. The effective conductance of the contacting pair is then obtained as the reciprocal of the effective resistance, similarly to equation (105). The three-dimensional version of this model is yet to appear. Recently, another version of DTEM was proposed by Liang [105], based on the series solution instead of a particular solution for the Laplace equation for the same boundary value problem. Other possible approaches, also based on conductances rather than on conductivities, are as suggested by Radjaï and Dubois [51] and Vargas-Escobar [70]. We remark that we prefer to work with the conductivity rather than with the conductance, since the former is a material property, whereas the latter is a component-based one. The thermal conductivities of the particles are assumed to be constant with temperature in this work[8] (although we could easily consider temperature-varying ones, in the lines of what is done for the mechanical properties in subsection 4.6). This is a reasonable approximation for a wide range of engineering materials and operating temperatures – at least as long as the particles remain in the same phase – but needs to be updated with the phase change of the material. Note that expressions (102) and (104) stand for a source of coupling between the thermal and mechanical fields, as it had been previously mentioned in a remark at the bottom of section 2.3.

4.3 Heat power due to convection

The surrounding environment (e.g., the environmental air) may exchange heat with the particle through convection. The corresponding heat flow on the particle may be computed through the classical Newton´s law of cooling. We adopt the following expression

$$\dot{Q}_i^{conv} = h_i(\theta_E - \theta_i)A_i^s \,, \tag{107}$$

where h_i is the convection (or film) coefficient of the particle w.r.t its surrounding environment, θ_E is the environment´s temperature at the particle´s location (which must be known) and

[8] Likewise the specific heat, this value can vary as a function of temperature and phase of the particle, as it will be seen Chapter 5.

$A_i^s = 4\pi r_i^2$ is total surface area of the particle. We assume that the convection coefficient is independent (or only marginally dependent) of the temperature difference between the particle and the environment. By resorting to the Nusselt number $\left(\mathrm{Nu}\right)$ of the environment around the particle (ratio between its heat transfer of convection to heat transfer of conduction), the convection coefficient may be given by

$$\mathrm{Nu} = \frac{h_i L}{k_E} \quad \Rightarrow \quad h_i = \frac{\mathrm{Nu}\, k_E}{L}, \tag{108}$$

where $L = 2r_i$ is the length scale and k_E is the environment´s thermal conductivity. For general applications, in which the particle may be traveling in the environment instead of being stationary, the Nusselt number may be related to the Reynolds number and Prandtl number through the well-known heat transfer expression for flows past single spheres (see Whitaker [106])

$$\mathrm{Nu} \approx 2 + \left(0.4\,\mathrm{Re}^{1/2} + 0.06\,\mathrm{Re}^{2/3}\right)\mathrm{Pr}^{0.4}\left(\frac{\mu_E}{\mu_{E,s}}\right)^{0.25}, \tag{109}$$

with

$$\mathrm{Re} = \frac{2\rho_{air} r_i \left\| \boldsymbol{v}_i - \boldsymbol{v}_{air} \right\|}{\eta_{air}} \quad \text{and} \quad \mathrm{Pr} = \frac{C_E \mu_E}{k_E}, \tag{110}$$

where Re is the Reynolds number, η_{air} is the viscosity of the air, ρ_{air} is the mass-density of the air and, Pr is the Prandtl number (wherein C_E is the environment´s specific heat), μ_E is the environment´s fluid viscosity and $\mu_{E,s}$ its viscosity at the particle´s surface temperature (we assume $\mu_{E,s} \approx \mu_E$ throughout this work). Expression (109) is a semi-empirical relation, and allows for a realistic estimate to the convection coefficient of smooth spheres for a wide range of heat transfer and fluid flow regimes . For nearly stationary particles within calm (stagnant) environments, as is the case for most AM processes we are interested in this work, as the Reynolds number tends to zero, and consequently the Nusselt number to two, from equation (108) one has $h_i \cong k_E / r_i$. This resembles natural (i.e., free) convection situations, and will be adopted throughout this work (unless otherwise stated, where then equation (108) with (109) would hold). We remark that the above model is a “one-way” type of model, in the sense that the environment´s temperature affects the particles but the particles´ temperatures do not affect

the environment. This may seem a rather rough approximation, but suffices for the purposes of this work. Besides, it is consistent with the small particles assumption. More elaborate approaches, e.g. solving for both the environment´s and particle´s temperatures in a large-scale CFD (computational fluid dynamics) coupled analyses, are obviously possible, but not considered here (this is outside the scope of this thesis).

4.4 Heat power due to radiation

Heat flow by radiative effects may be relevant if the particle´s surrounding environment (e.g. the environmental air) has a significantly different temperature as compared to the particle´s own temperature. In many applications, the particles are severely heated, whereas its surroundings remain (at least in an average sense) at a much lower temperature. In such condition, the amount of electromagnetic thermal radiation that is emitted by a particle may be significantly larger than that absorbed by it from the environment, creating an outward net energy flow from the particles that ultimately promotes overall cooling of the system. We follow the Stefan-Boltzmann law to account for this energy transfer mechanism, and adopt the following expression:

$$\dot{Q}_i^{rad} = \varepsilon_i B(\theta_E^4 - \theta_i^4)A_i^s \,, \tag{111}$$

where $0 \leq \varepsilon_i \leq 1$ is the particle´s radiative cooling efficiency or material emissivity, which must be known, $B =$ 5.670367×10^{-8} W/m^2·K^4 is the Stefan-Boltzmann constant, θ_E is the environment´s temperature at the particle´s location (which must also be known) and $A_i^s = 4\pi r_i^2$ is the particle´s surface area. Again, the environment´s temperature, besides being known (i.e., given), is assumed to be unaffected by the particle´s temperature (a "one-way" model). We once again acknowledge that this may be a rather rough approximation, but it suffices for the purpose of this work (besides, it is likewise consistent with the small particles assumption). Radiative heat transfer between particles is also possible to consider, since it could potentially have a significant contribution in the overall heat transfer of the system. This, however, has not been included in the present work and is left as a matter for future investigations.

4.5 Heat power due to external devices

In the present work, we are focusing on external devices such as fire nozzles, burners, laser beams, electric currents, etc. where the heat power can be described through given (ad-hoc) expressions according to the type of device that is heating up the system.

Figure 25 – Representation of external device´s heat penetration within a granular material. The depth of a particle w.r.t. the device´s striking position is measured by z_i, whereas the device's maximum penetration (or heating reach) is d_{max}

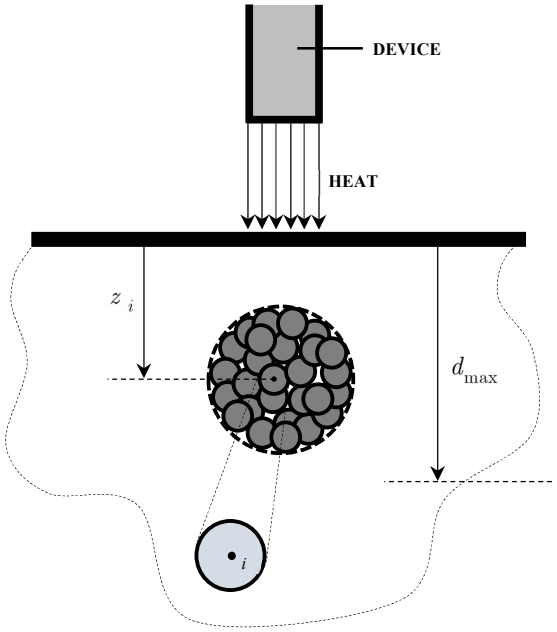

Source: Author.

A general expression is

$$\dot{Q}_i^{ext} = a_i I_i^{dev}, \tag{112}$$

where $0 \leq a_i \leq 1$ is the particle´s absorptance (or absorptivity, ratio of the absorbed to the incident heat power, ascertaining the effectiveness of the particle´s surface in absorbing heat), which must be known, and I_i^{dev} is the device's input power at the particle's location, which must also be known. For, e.g., fire nozzles, one possible expression for I_i^{dev} is

$$I_i^{dev} = I_0 A_i \left(1 - \frac{z_i}{d_{\max}}\right), \tag{113}$$

where I_0 is the nozzle´s nominal input intensity (power per unit area of the nozzle´s cross-section, which must be known), $A_i = \pi r_i^2$ is the particle´s frontal area (i.e., the area that is exposed to the nozzle´s power), $d_{\max}$ is the maximum penetration (or heating reach) of the nozzle within the bulk of the material (which must also be known) and $0 \leq z_i \leq d_{\max}$ is the particle´s depth with respect to the nozzle´s striking position (measured along the nozzle´s path-length, as indicated in Figure 25). This is based on the assumption that the nozzle´s power attenuates linearly inside the material until the maximum depth $d_{\max}$ is reached. If, e.g., the nozzle is such that its power affects only the surface of the material, not penetrating its interior, one must set $d_{\max} = r_i^{top}$, with r_i^{top} as the radius of the top-layer particles, implying that only these particles will be directly heated by the nozzle (all sub-surface heating will be accomplished by conduction from the top layer).

Figure 26 – Schematic representation of the laser beam, $\boldsymbol{x}_{dev}$ is the striking position of the external heating device (or position vector of the device's cross-section center) and $\boldsymbol{d}_i$ is the distance between particle *i* and the device's striking position

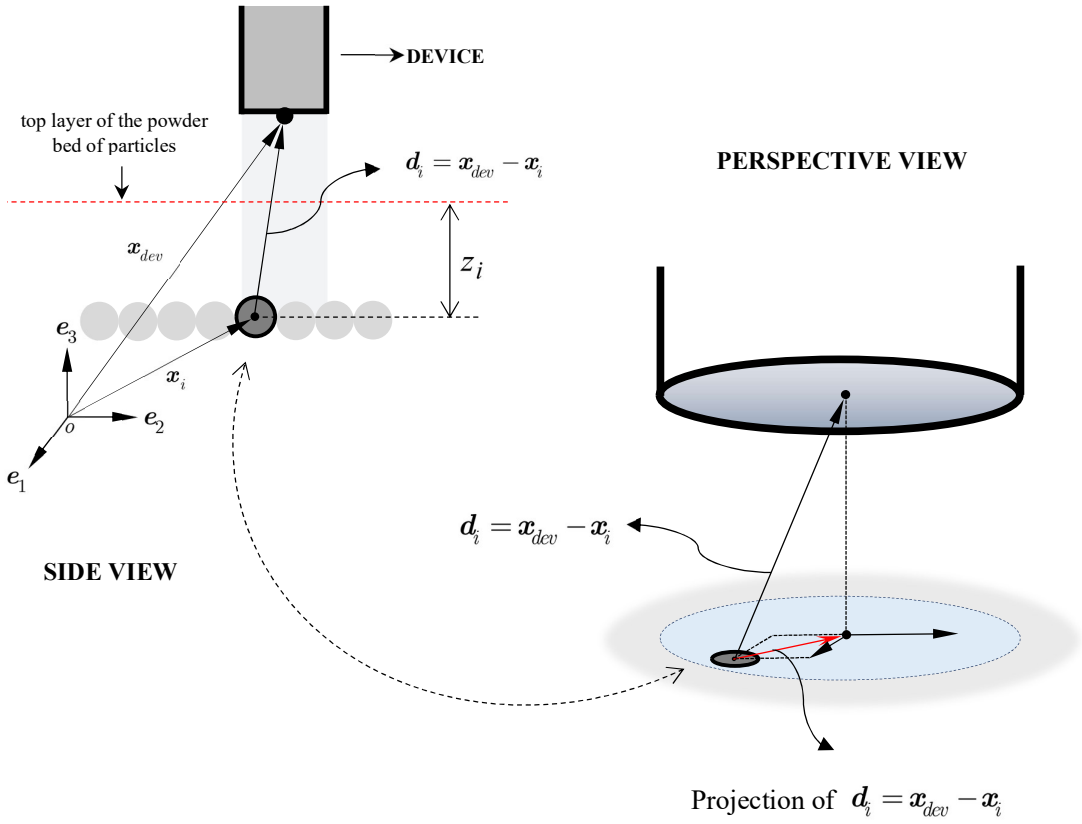

Source: Author.

For laser beams, in turn, one possible expression for I_i^{dev} may be derived from the Lambert-Beer law, which states that the attenuation of incident light through a material (by both absorption and scattering) is exponentially dependent on the material′s thickness (or, more precisely, optical depth) and its attenuation coefficient. Accordingly, we write

$$I_i^{dev} = I_0 A_i e^{-\mu z_i}, \tag{114}$$

where I_0 is the laser′s input intensity (power per unit area of the beam′s cross section, which must be known), $A_i = \pi r_i^2$ is the particle′s frontal area, μ is the material′s attenuation coefficient (a bulk property determining how much the radiant power of the beam is reduced as it passes through the bulk of the material, with units of m^{-1}) and z_i is the particle′s depth w.r.t. the beam′s striking position (measured along the beam′s path-length). This expression is obtained by assuming uniform attenuation in the Lambert-Beer law, in the sense that μ does not vary throughout the path-length of the beam. A schematic representation of the laser beam can be seen in the Figure 26.

We remark that consideration of the transmittance of the laser through the interior of the material is of utmost importance. Otherwise, only the surface layer remains hit by the beam, leaving all deeper (sub-surface) heating to be accomplished solely by conduction from the top layer – a scenario that is far too conservative for laser devices. Considering the penetration of the heat source through the bulk of the material allows the deeper parts to be heated up more rapidly, effectively and represents the physical process in a more reliable way.

Figure 27 – Schematic view of the intensity as a function of depth and radii

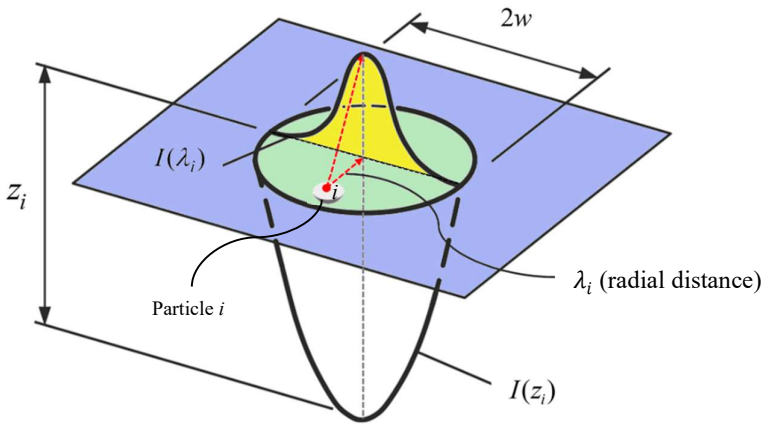

Source: Adapted from Wessels et al. [107].

A particular type of laser beam, very often observed in the types of lasers that are used in SLS, is the so-called Gaussian laser beam. In this case, the laser's input power varies over the beam's cross-section according to a Gaussian function, as measured from the axis of the beam. Accordingly, the energy that hits a particle may be computed by an intensity function depending on the particle's position w.r.t. the laser center. This function is as follows:

$$I_i^{dev}(\lambda_i, z_i) = I_0 A_i e^{-\mu z_i} e^{(-2\lambda_i^2/w^2)}, \tag{115}$$

where I_0 is the peak intensity (whose expression will be shown shortly below), λ_i is the radial distance between the center of the laser beam and particle i (see Figure 27, Wessels et al. [107]), μ is the attenuation coefficient (the same as introduced previously in equation (114)), which gives a measure of how quickly an electromagnetic wave attenuates in the material, and w is the beam spot size (or the radius of the laser beam itself).

For the peak intensity, we write equation (116) where P_0 is the power of the laser in (W) and f is the distribution factor (i.e., a factor such that the energy becomes more focused with a higher value of f, see Figure 28, DebRoy et al. [108]).

$$I_0 = \frac{fP_0}{\pi w^2}. \tag{116}$$

Figure 28 – Distribution factor of Gaussian laser beam

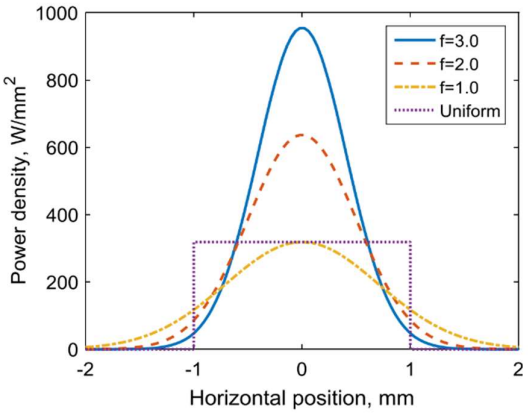

Source: DebRoy et al. [108].

For powders and granular materials, the attenuation coefficient may be computed according to the theory of Gusarov et al. [90] [109]. It can be found in the literature by the name of optical extinction coefficient (β). For spherical powder particles this value can be approximated as

$$\beta = \frac{3}{2}\frac{1-\phi}{\phi}\frac{1}{D}. \tag{117}$$

where ϕ is the porosity of the powder bed of particles, and $D = 2r_i$ is the dimension of a typical particle. Other expressions for the device′s input power may be adopted, according to the problem at hand.

4.6 Thermal softening of mechanical properties

Most materials have their mechanical properties degraded with increasing temperature. To incorporate such softening effects into the particles′ dynamics, one straightforward way is to consider temperature-dependent mechanical properties (e.g., by means of given input curves), instead of constant-valued ones. Accordingly, we adopt the following expression for the particles′ elasticity modulus:

$$E_i = \hat{E}_i(\theta_i) = \min\left\{E_0, E_0 e^{1-\frac{\theta_i}{\theta^*}}\right\}, \tag{118}$$

where E_0 is the modulus′ ground or reference value (e.g., the value at room temperature, or at a temperature interval around the room temperature) and θ^* is the critical temperature at which it starts to degrade. A threshold value $E_{\min}$ may also be introduced, as to prevent indefinite softening. Figure 29 depicts (qualitatively) the general behavior implied by this relation for a ground modulus of $E_0 = 1$ MPa and a critical temperature of $\theta^* = 400\,\mathrm{K}$.

Expression (118) may also be modified as to include a degrading rate coefficient, which would multiply the temperature term on the exponent. This would allow one to fine-tune the strength or mildness of the decaying rate, and thereby approximate other softening behaviors such as linear and hyperbolic softening (as commonly observed for many metals and ceramic materials). One should notice that thermal softening affects not only the particle′s normal stiffness (and therefrom its normal contact forces), but also its tangential stiffness (and thus its friction forces and rolling resistance moments), since the elasticity modulus enters the expression of the particle′s shear modulus.

The thermal softening of many common engineering materials may be satisfactorily approximated by expression (118). Other ad-hoc relations (e.g., multilinear or more elaborate laws) are likewise possible to be incorporated. Moreover, others mechanical properties such as the friction coefficient or the damping rates can be considered too as a temperature-dependent property of the material, but this will not be considered in the present work. We will restrict here to the particles´ elasticity modulus and the properties that depend on it.

Figure 29 – Schematic illustration of the thermal degradation of a particle´s elasticity modulus as implied by the proposed relation. Other mechanical properties may likewise vary with temperature, such as the friction coefficient and the adhesion stiffness

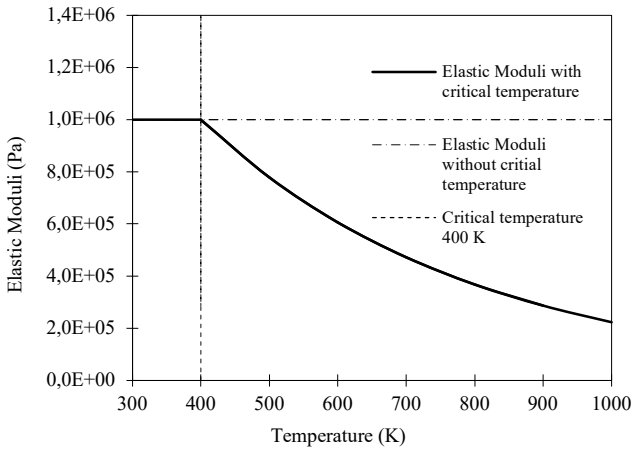

Source: Author.

Remark 6. The consideration of other heat sources and energy transfer mechanisms, such as heating or cooling due to internal chemical reactions (triggered, e.g., by reactive thin films adsorbed onto the particles´ surface, which may be activated by inter-particle collisions), is entirely possible, but not considered here. The onset and subsequent progress of such reactions may be represented through simple evolution laws that capture their overall influence on the mechanical and thermal states of the particles. Also, heat dissipated through inelastic impacts, as well as induced by dragging effects (due to friction with the surrounding environment at high speeds), are likewise possible, but will not be considered here (for a straightforward way to deal with drag-induced heating, see e.g. Campello [110]).

4.7 Thermal expansion

According to Driver [111], in studies with scientists of Lawrence Livermore National Laboratory (LLNL), reported that the thermal expansion can be potentially significant during the SLS process due to the large amplitude of operating temperatures. This, of course, depends on the particle sizes involved and on the thermal properties of the particles´ constituent material. Also, Ji and Liu [72] stated that the variation of the particles' temperature, producing thermal expansion or contraction of the particle, strongly affects the macroscopic properties of the particles. One of the possible causes could be the thermal expansion of the material that occurs when the laser runs across the powder bed, such that, if the particles are overconstrained (i.e., have their motion restrained somehow), they may pop out of the basin, as illustrated in Figure 30. To account for this effect, here we assume that the radius of a particle r_i is a linear function of the particle´s temperature:

$$r_i(t + \Delta t) = r_i(t)\left[1 + \alpha_i \Delta\theta\right], \tag{119}$$

where $r_i(t + \Delta t)$ is the updated radii of the particle, $\Delta\theta = \theta_i(t + \Delta t) - \theta_i(t)$ is the temperature gradient of the particle between two configurations and, α_i is the thermal expansion coefficient of the particle´s constituent material, which must be known.

Figure 30 – Set of particles without thermal expansion (left). With thermal expansion (right)

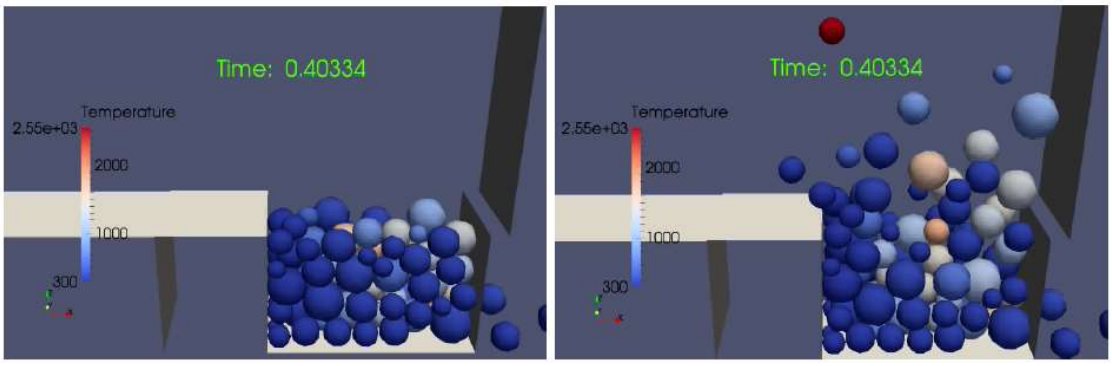

Source: Driver [111].

4.8 Phase change

In many AM processes, such as (but not only) SLS, the particles are purposely heated up to their fusion or melting point. This means that phase transformations are inherently observed, and thereby have to be incorporated into the model somehow. To capture this physical phenomenon, or at least the most essential parts of its effects, one of the simplest approaches is the so-called Apparent Heat Capacity method, Bonacina et al. [112] and Muhieddine et al. [113]. According to Zeneli et al. [114], the work of Hashemi and Sliepcevich [115] was the first to propose this technique, distributing the latent heat over a finite temperature interval to deal with numerical instabilities arising from strong discontinuities in specific heat capacity values during the phase change. In this method, the energy necessary to put forth the phase change is considered by gradually and continuously raising the specific heat of the material in a small interval of temperature ($\Delta\theta$) around the melting or vaporization temperature, while keeping the original governing equations of the problem.

Accordingly, the required increase in the specific heat may be computed from the latent heat of the material for the corresponding phase transformation. The strategy used here, as adapted from Ganeriwala and Zohdi [116], is summarized as follows and is schematically illustrated in Figure 31.

$$C_i = \begin{cases} C_{i,solid} & \theta_i < \theta_{i,m} - \dfrac{\Delta\theta}{2} \\ \dfrac{C_{i,solid} + C_{i,liquid}}{2} + \dfrac{L_{i,m/s}}{\Delta\theta} & \theta_{i,m} - \dfrac{\Delta\theta}{2} \le \theta_i \le \theta_{i,m} + \dfrac{\Delta\theta}{2} \\ C_{i,liquid} & \theta_{i,m} + \dfrac{\Delta\theta}{2} < \theta_i < \theta_{i,v} - \dfrac{\Delta\theta}{2} \\ \dfrac{C_{i,liquid} + C_{i,gas}}{2} + \dfrac{L_{i,v/c}}{\Delta\theta} & \theta_{i,v} - \dfrac{\Delta\theta}{2} \le \theta_i \le \theta_{i,v} + \dfrac{\Delta\theta}{2} \\ C_{i,gas} & \theta_i > \theta_{i,v} + \dfrac{\Delta\theta}{2} \end{cases}, \quad (120)$$

where $C_{i,solid}$ is the specific heat in the solid phase, $C_{i,liquid}$ is the specific heat in the liquid phase, $C_{i,gas}$ is the specific heat in the gas phase, $\theta_{i,m}$ is the melting temperature, $\theta_{i,v}$ is the vaporization (or boiling) temperature, $L_{i,m/s}$ is the latent heat of melting or solidification, and

$L_{i,v/c}$ is the latent heat of vaporization (or condensation). In this simplified model, the small temperature interval $\Delta\theta$ over which the specific heat is increased must be specified. Typically, a small fraction of the melting and vaporization temperatures is considered, e.g., 10% (see Xin et al. [117], Wessels [118]). In this work, we adopt this suggested value.

Figure 31 – Apparent Heat Capacity method. a) Heat capacity as a function of temperature. b) Temperature as a function of heat input

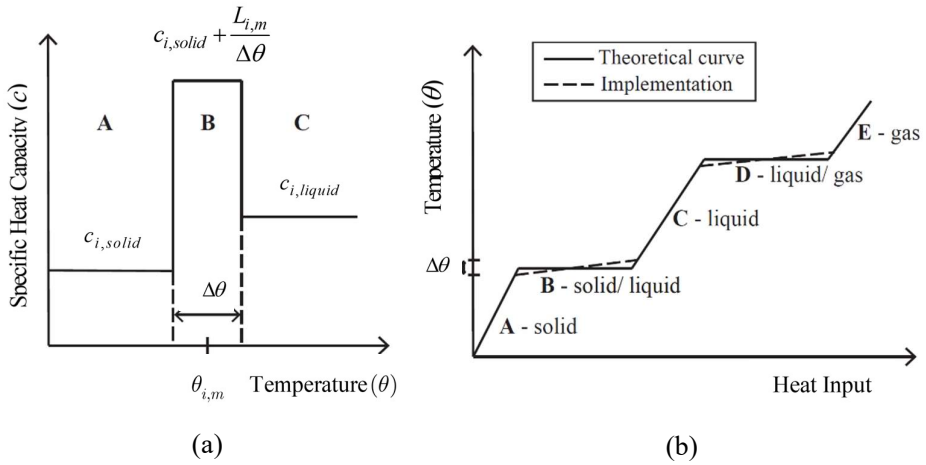

Source: Ganeriwala and Zohdi [116].

4.8.1 Molten particles

In a DEM model with phase change, the treatment of molten particles (that is, of particles that were once solid and thus had well defined shape and volume until then, but now are liquid) has to be done in ad-hoc (and often roughly approximate) ways. Different approaches are available in the literature, as described, e.g., by Zohdi [13]. One of them consists in braking up the original particle into smaller (molten) particles, which will behave like a “fluid” and would be governed by different interaction rules. However, and despite of the quite realistic simulations this technique can offer, it is highly computationally expensive. Another alternative is to consider the phase-transformed part of the material as a continuum and run the simulations through a hybrid discrete element-continuum approach. In this option, the computational cost might be very significative too, but in return and likewise the previous approach, the results are

potentially very realistic. More details of this option can be found in Galindo-Torres [119] and Wellman and Wriggers [120].

Another simpler (ad hoc) approach is to keep the melted particles as solid particles but assign them a different set of properties (e.g., reduce their elasticity modulus), and remove from the simulation those particles with temperature greater than the boiling temperature (i.e., the gas phase). In this work, the author opted for this latter approach, since our objective here is only having an approximate model able to capture only the basic phenomena involved, with which we may enable a rapid simulation tool for qualitative (and also roughly quantitative) assessment of process performance. The author acknowledges that more sophisticated (coupled discrete-continuum) approaches are superior, but they are left outside the scope of the present work. Yet, despite the simplicity, the adopted approach may render useful results for real applications, and is indeed also followed by many other authors (see, e.g., Xin et al. [117], Ganeriwala and Zohdi [116] [121]).

4.9 Numerical solution method

For the thermal states of the particles we follow the same approach as for the mechanical part presented in subsection 2.4. Accordingly, to solve the governing equation of the thermal field represented by equation (101), we discretize the time interval of the analysis (t_0, t_F) into time instants $\left\{t_0, t_1, t_2, ..., t_i, t_{i+1}, t_F\right\}$, and perform time integration of equation (101) between two consecutive time instants, arriving at (with the aid of the generalized trapezoidal rule)

$$\begin{aligned}\theta_i(t+\Delta t) &= \theta_i(t) + \frac{1}{m_i C_i}\int_t^{t+\Delta t} \underbrace{\left(\dot{Q}_i^{ext} + \dot{Q}_i^{cond} + \dot{Q}_i^{conv} + \dot{Q}_i^{rad}\right)}_{\dot{Q}_i^{total}} dt \\ &\approx \theta_i(t) + \frac{\Delta t}{m_i C_i}\left[\left(1-\phi\right)\dot{Q}_i^{total}(t) + \phi\dot{Q}_i^{total}(t+\Delta t)\right],\end{aligned} \tag{121}$$

where, if we take $\phi = 0$ (forward Euler scheme), we have

$$\theta_i(t+\Delta t) \approx \theta_i(t) + \frac{\Delta t}{m_i C_i}\left(\dot{Q}_i^{ext}(t) + \dot{Q}_i^{cond}(t) + \dot{Q}_i^{conv}(t) + \dot{Q}_i^{rad}(t)\right). \tag{122}$$

4.9.1 Two-field solution algorithm

The solution method adopted for the thermo-mechanical problem is the explicit (forward Euler) scheme of the mechanical problem with the addition of the thermal equations. The author has decided to employ this approach for the same reason as for the mechanical part. The scheme for the two-field (thermal and mechanical) problem is a staggered solution strategy that consists in firstly computing the mechanical part, while freezing the thermal part, and then resolving the thermal part, while freezing the mechanical part but using the mechanical values that have been just updated. The scheme is very straightforward and is summarized in the Algorithm 3 below.

Algorithm 3.

1. Initialize time variables and get initial conditions:

   $t = 0,\ \Delta t = \text{given}\,,\ t_F = \text{given}\,,\ \phi = \text{given}$

   $\boldsymbol{x}_i(0),\ \boldsymbol{v}_i(0),\ \boldsymbol{\omega}_i(0),\ \boldsymbol{\alpha}_i(0),\ \theta_i(0) = \text{given}$

2. WHILE $t \leq t_F$, loop over particles: FOR $i = 1,...,N_P$ DO
   i. Compute forces and moments at time t via equations (18), (23)-(29), (32) and (33)-(38) taking (118) into account.
   ii. Compute heat powers at time t via equations (112), (102), (107) and (111). If appropriate, take into account equations (120) and (119).
   iii. Freeze thermal field and update velocities, spins, positions and incremental rotations via equations (43) and (46) (we recall that we adopt $\phi = 0$).
   iv. Freeze mechanical field and update temperatures through equation (122).
   v. Save updated variables and move to next time step:

   $\boldsymbol{v}_i(t) \leftarrow \boldsymbol{v}_i(t + \Delta t),$

   $\boldsymbol{\omega}_i(t) \leftarrow \boldsymbol{\omega}_i(t + \Delta t),$

   $\boldsymbol{x}_i(t) \leftarrow \boldsymbol{x}_i(t + \Delta t),$

   $\boldsymbol{\alpha}_i(t) \leftarrow \boldsymbol{\alpha}_i(t + \Delta t),$

   $\theta_i(t) \leftarrow \theta_i(t + \Delta t),$

   $t \leftarrow t + \Delta t.$

3. GOTO 2.

4.10 Validation and illustration

This section illustrates the usage of the above model through a few numerical examples. First, we show one simple validation problem involving only a single particle (we remark that extensive validation of the model has been conducted in a separate study, and will not be reported here for conciseness). Next, we analyze more general, multi-particle model-problems. As in Chapter 3, we select the time step size in each example according to the following criterion, which is based on the expected duration of the particles´ contacts or collisions:

$$\Delta t \leq \frac{\delta t_{con}}{20}, \quad \delta t_{con} \cong 2.87 \left[\frac{(m^*)^2}{r^* (E^*)^2 v_{rel}} \right]^{1/5}, \tag{123}$$

where δt_{con} is the duration of a typical contact or collision and v_{rel} is the relative velocity of a typical contacting pair in the pair´s central direction immediately before the contact or collision is initiated. This is based on Hertz´s contact theory (see Johnson [95]) and, according to our experience, allows for a good accuracy in the integration of the contact forces. Contact detection is performed through the binning algorithm, presented in the subsection 2.5. For another type of contact detection (i.e., a hybrid global-local search method where both domain subdivision cells and nearest-neighbors lists ("Verlet lists") are combined), we refer the interested reader to Campello [11]. Adhesion forces are not considered in this Chapter.

4.10.1 Interaction between a particle and thermal base

This example is analyzed to investigate the behavior of the basic ingredient of a thermo-mechanical particle system, namely, the interaction between two contacting entities. For simplicity, we consider here a single particle in contact with a thermal floor, with arbitrarily different initial temperatures. We want to assess some of the features of our scheme under simple idealized conditions, such that we may better highlight its coupled thermal-mechanical aspects. In particular, we want to evaluate the evolution of the particle´s temperature and its subsequent effect upon the particle´s elastic stiffness and contact force. Let us consider a

particle with radius $r = 1$ mm, placed tangentially over a thermally-active base, as shown in Figure 32. Gravity acts downwards.

Figure 32 – Single particle under gravity placed over thermally active floor

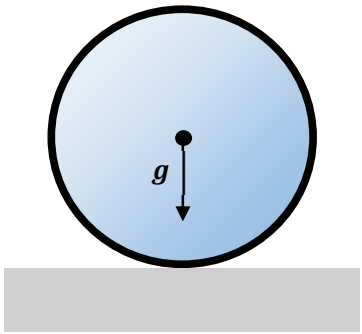

Source: Author.

The particle has an initial temperature $\theta(0) = 300$ K and is made of a material with thermal conductivity $k = 60$ W/m.K, specific heat $C = 100$ J/kg.K, mass-density $\rho = 3000$ kg/m^3 an elastic properties at room temperature $E_0 = 1.0$ MPa and $\nu = 0.3$, with critical degrading temperature $\theta^* = 400$ K. Critically damped contact is considered ($\xi^{con} = 1$). The floor is assumed to have infinite mass and zero conductivity (i.e. it does not change its thermal state over time), with a constant temperature of $\theta_{floor} = 700$ K. The surrounding environment is not considered (i.e., it does not absorb nor provide heat to the particle). As gravity drives the particle towards the floor, they make contact and the particle starts to receive heat through conduction, since it is at a smaller temperature than the floor. Eventually, the particle attains mechanical and thermal equilibrium with the floor. Figure 33a-f depict the evolution of the particle´s temperature with time, along with time histories of its elastic moduli, overlap, contact area and contact force. As we can see in Figure 33a, thermal equilibrium is reached at around $t \approx 12$ s. The elastic moduli is clearly seen to degrade (Figure 33b), and the overlap consequently is seen to increase until thermal equilibrium with the floor is reached (Figure 33c). Another interesting aspect, as a consequence of the increase in the overlap, is the increment of the contact area (Figure 33d), of about 63%, if compared to the area when thermal softening is not considered. This implies an increase in the amount of conduction heat flow between both objects, as it can be seen in Figure 33e. Therein, a reference line at $t \approx 6$ s is plotted in the graph, for which the temperature of the particle is seen to be about 7% higher than that in the

case without thermal softening. Larger differences could be observed, depending on the thermal properties that are adopted.

Figure 33 – Interaction between a particle and a thermal base. Analysis results

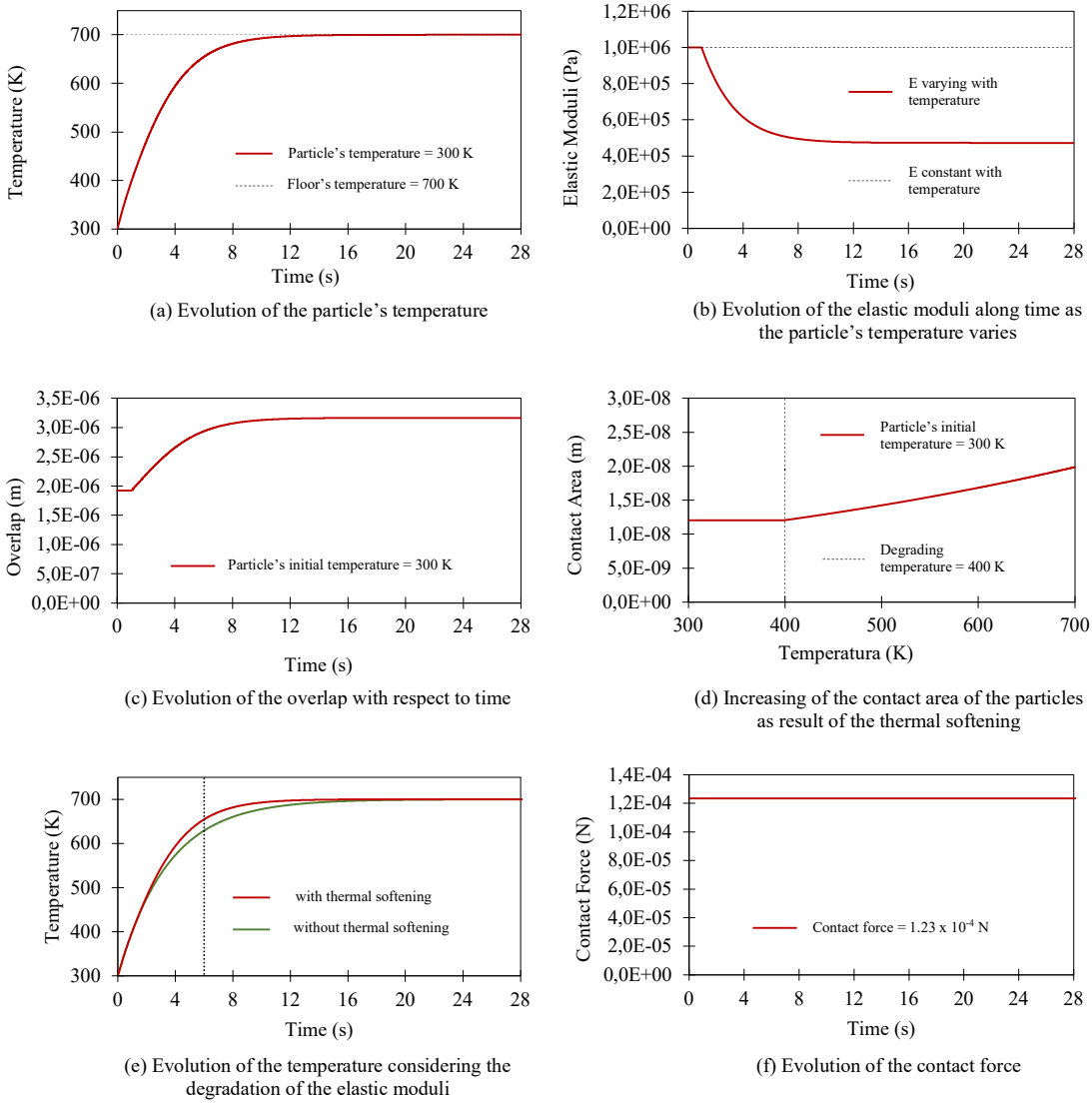

(a) Evolution of the particle's temperature

(b) Evolution of the elastic moduli along time as the particle's temperature varies

(c) Evolution of the overlap with respect to time

(d) Increasing of the contact area of the particles as result of the thermal softening

(e) Evolution of the temperature considering the degradation of the elastic moduli

(f) Evolution of the contact force

Source: Author.

Also, with thermal softening thermal equilibrium is reached faster than in the case without softening (~12 s against ~18 s). With regards to the contact force, the change in elastic modulus and overlap would make one to expect that the contact force also varies in time; however, it is seen from the graph in Figure 33f that this does not happen: after mechanical equilibrium is attained (this occurs very rapidly at the beginning, and cannot be seen from the

adopted graph scale), the force is perfectly constant in time, with a value of 1.23×10^{-4} N. It turns out that the decrease in stiffness is exactly compensated by the increase in the overlap, and the force remains constant thereby. Indeed, this is consistent with static equilibrium arguments, since the only external force acting upon the particle is the gravity force, which is constant. The time step size adopted in this simulation was $\Delta t = 2 \times 10^{-5}$ s whereas the final time was $t = 40$ s.

4.10.2 Heated and vibrated extended granular medium

This example has been originally proposed by Campello [11], however without consideration of heat. At the time, the author was interested in the purely mechanical part of the problem, namely, the onset of surface instabilities followed by the formation of well-marked surface waves. This interesting phenomenon may be observed if an extended (i.e., shallow) granular stack is vibrated vertically under certain frequencies. It has been studied through physical experiments by Clément et al. [122] and Duran [14], among others, and their results were numerically reproduced in Campello [11]. Here, instead, we want to analyze a thermo-mechanical version of the problem, by heating up the granular medium while it is being vibrated, with the aim to investigate the evolution of its thermal states and the role of conduction and convection.

Figure 34 – Heated and vibrated extended granular medium. Problem definition. The initial temperatures of the particles are 300 K

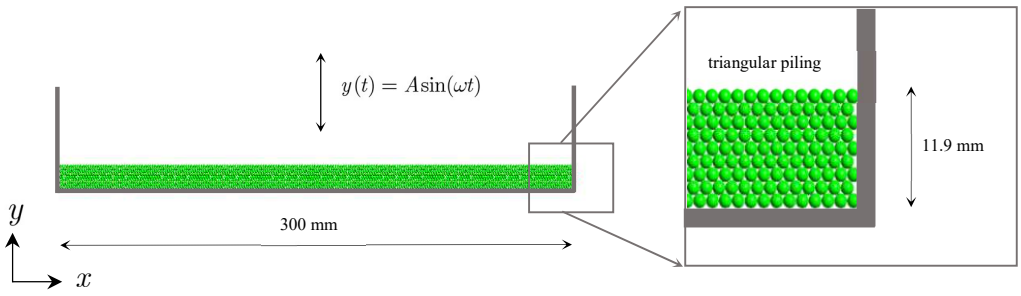

Source: Campello [11].

Accordingly, nine layers of particles with diameter 1.50 mm and initial temperatures 300 K are disposed at the bottom of a rectangular cell of 300 mm width, as shown in Figure 34

(the same setting as in the original example). The layers are piled in a regular triangular arrangement, such that the total height of the stack at rest is 11.9 mm. The problem is mounted in a bi-dimensional setting, as to facilitate visualization of results. The cell is shaken vertically according to the displacement function, with given amplitude and angular frequency. A normalized acceleration measure $\Gamma = A\omega^2 / g$ (with $g = 9.8$ m/s^2 as the gravity acceleration), is taken as a control parameter. At $t = 0$, the cell walls are given an initial temperature of 1000 K, which is then held constant throughout the simulation. The air´s temperature, in turn, is taken as 273 K. Other data are as follows:

- mass-density of the particles: $\rho = 2700$ kg/m^3;
- elastic properties of the particles: $E_i = 700$ MPa and $\nu_i = 0$;
- friction and rolling resistance coeff. between particles: $\mu_s = \mu_d = 0.5$ and $\mu_r = 0.01$;
- friction and rolling resistance coeff. between particles and walls: $\mu_s = \mu_d = \mu_r = 0$;
- friction and rolling resistances damping rates: $\xi^{con} = \xi^{fric} = 0.16$ and $\xi^{rol} = 0.01$;
- thermal properties of the particles: $k_i = 500$ W/m.K and $C_i = 5$ J/kg.K;
- thermal properties of the air $k_{air} = 0.025$ W/m.K and $C_{air} = 1000$ J/Kg.K;
- normalized acceleration parameter: $\Gamma = 3.4$;
- total number of particles: $N_P = 1796$;
- time-step size: $\Delta t = 5 \times 10^{-6}$ s.

Radiative effects and thermal softening are not considered (this allows us to concentrate solely on the effects of conduction and convection here). Figure 35 shows two sequences of snapshots as obtained with our simulation for the case with an excitation frequency of $f = 7.8$ Hz (which corresponds to a shaking amplitude of $A = 13.9$ mm). The left sequence is obtained by considering both conduction and convection, whereas for the right one the convection contribution is turned off. One can see that heat transfer through convection is particularly dominant here, not allowing the particles to heat up significantly even after they have made tens of thousands of contacts with the walls at $t = 60$ s. If convection is not considered, the particles´ temperatures steadily grow as the bottom and lateral layers are heated due to multiple contacts with the walls, and from them the other layers are heated through inter-particle

conduction. The particles are clearly seen to approach the walls´ temperature with increasing time.

Figure 35 – Heated and vibrated extended granular medium. Simulation results for the case with f = 7.8 Hz. Left sequences considers both conduction and convection: right sequences has convection turned off. Snapshots are taken at t = 1 s, 3 s, 6 s, 8 s, 10 s, 13 s, 20 s, 30 s, 40 s and 60 s

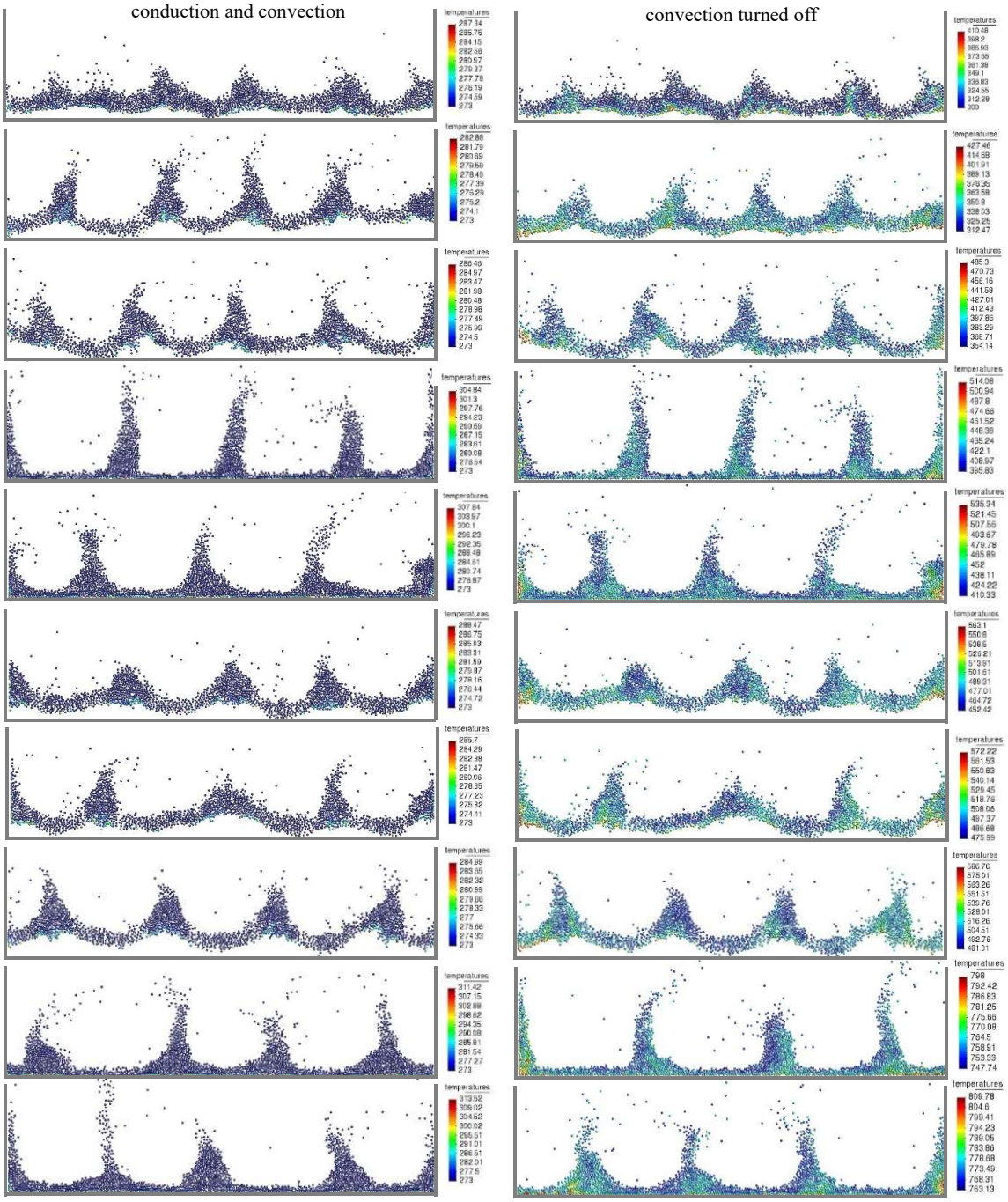

Source: Author.

Figure 36 – Heated and vibrated extended granular medium. Simulation results for the case with f = 12 Hz. Left sequences considers both conduction and convection: right sequences has convection turned off. Snapshots are taken at t = 1 s, 3 s, 6 s, 8 s, 10 s, 13 s, 20 s, 30 s, 40 s and 60 s

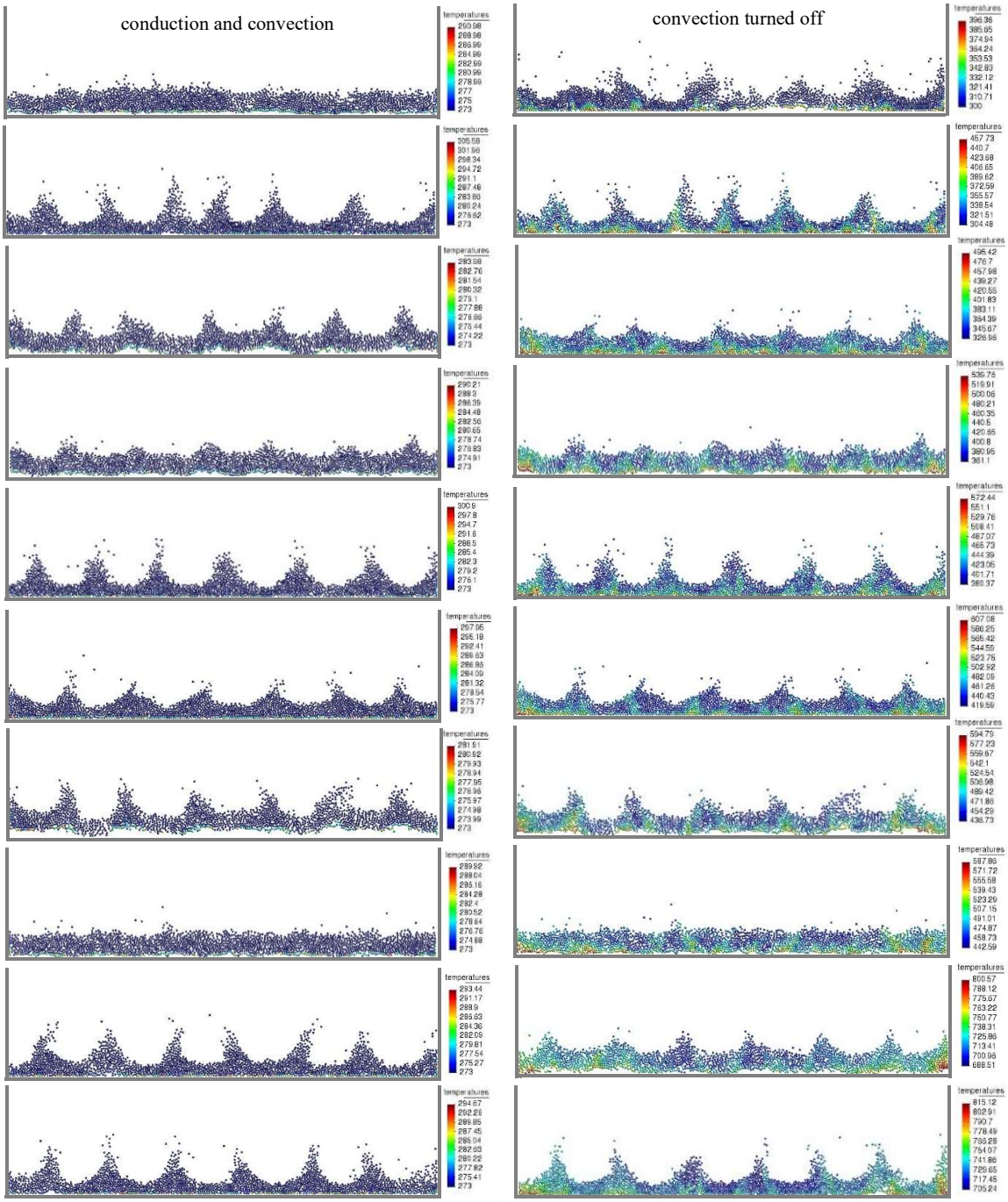

Source: Author.

Figure 36 displays the corresponding results for the case with an excitation frequency of $f = 12$ Hz (which corresponds to a shaking amplitude of $A = 5.9$ mm). The same overall behavior is observed, except that here the waves have a rather smaller height, and as consequence the heat transfer paths are different, leading to a different exchange of heat between particles and between particles and the environment. For this reason, the temperature distributions are slightly different as compared to the previous case.

4.10.3 Heated and vibrated extended granular medium (3D version)

Here we consider a 3D version of the previous problem. This type of problem is of major concern in many physics and engineering fields, ranging from foods to mineral processing, and has gained considerable attention because of its complex rheological behavior.

Figure 37 – Heated and vibrated extended granular medium. Problem definition. a) Side view b) top view c) isometric view

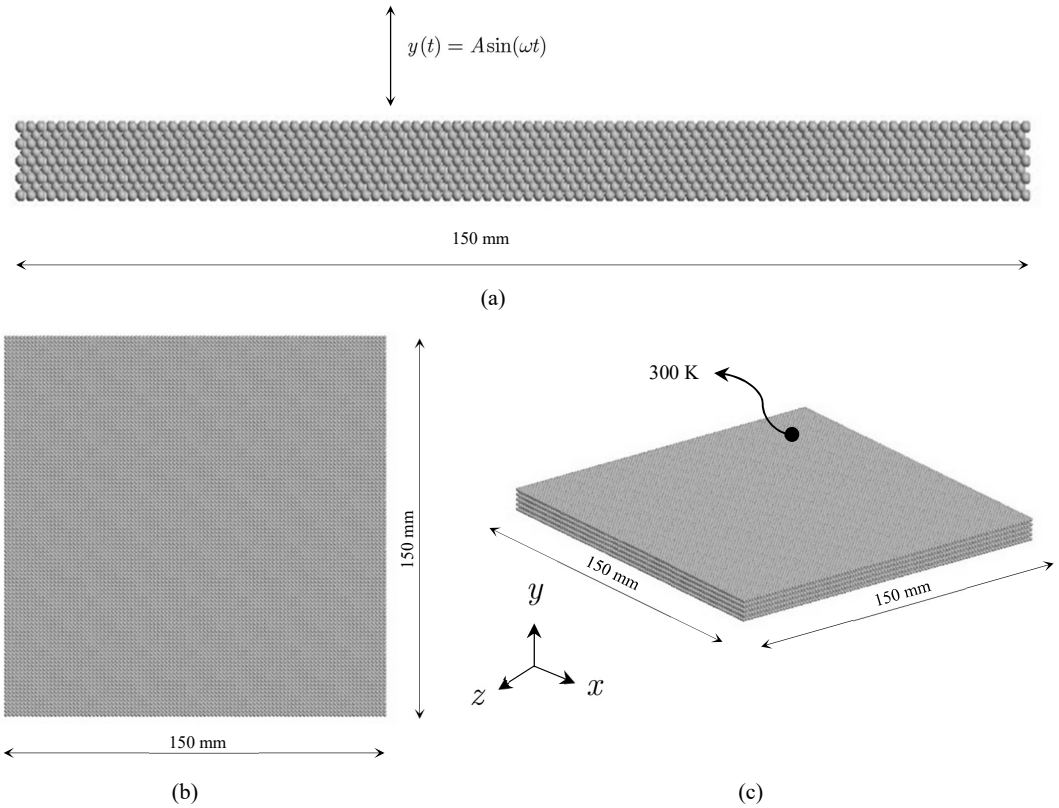

Source: Author.

Moreover, phenomenon like granular segregation can be present affecting the flow behavior of the granular system, some of them with somewhat curious effects like the Brazil Nut Problem (BNP) and Reverse Brazil Nut Problem (RBNP), Dolgunin et al. [123]. An assembly of $N_P = 89204$ particles are disposed at the bottom of a square box of 150 mm. Initial conditions and materials properties follows the very same of those of example 4.10.2, as well as the initial particles arrangement, see Figure 37.

Figure 38 – Surface patterns, top view. Gray color represents absence of temperature. Figures with blue color temperature is considered. a-d) t = 0.5 s, e-h) t = 1.0 s. Conduction, convection and radiation its on

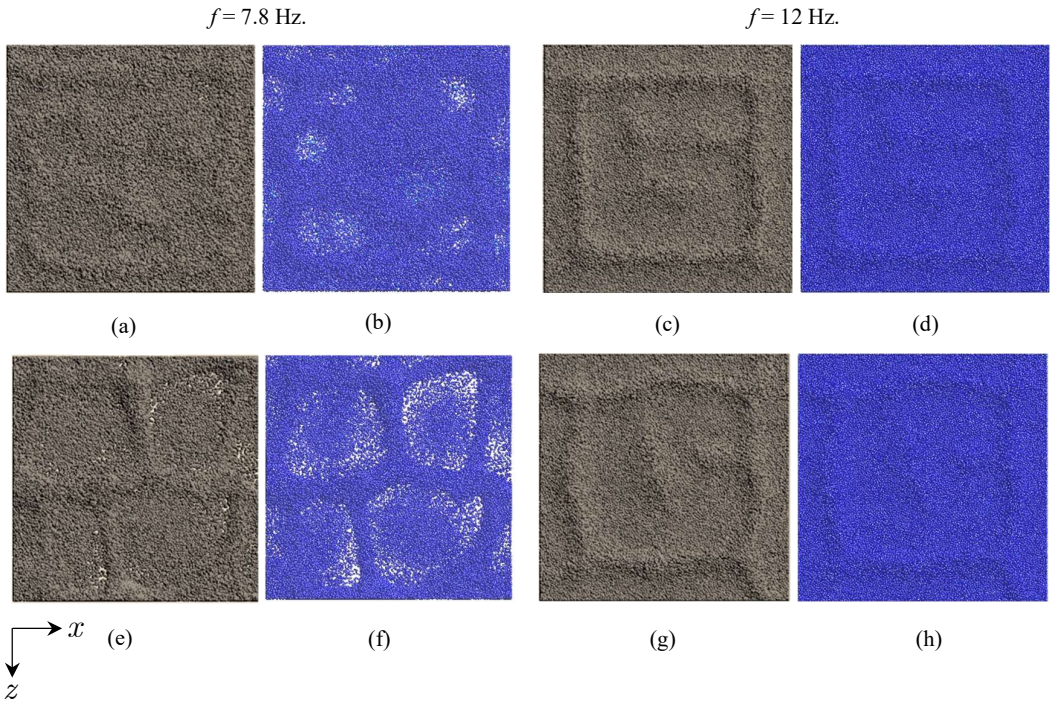

Source: Author.

As we can see in Figure 38, upon excitation the granular materials can show different surface patterns, and clearly this phenomenon is controlled by the frequency and the amplitude of the vibration. Apparently, the thermal coupling does not significantly affect in the waves' patterns formations, but this could change with the incorporation of a degrading thermal coefficient or with the phase transformation of the material, which would affect the mechanical properties like the elastic modulus, as mentioned in the subsection 4.6 , and therefrom affect the interparticle contact interactions.

Figure 39 – Surface patterns with an excitation frequency of f = 7.8 Hz (a-b) and f = 12 Hz (c-d). Bottom (left) and isometric (right) view. a) t = 0.5 s only conduction b) t = 0.5 s convection and radiation turned on c) t = 1.0 s only conduction d) t = 1.0 s convection and radiation turned on

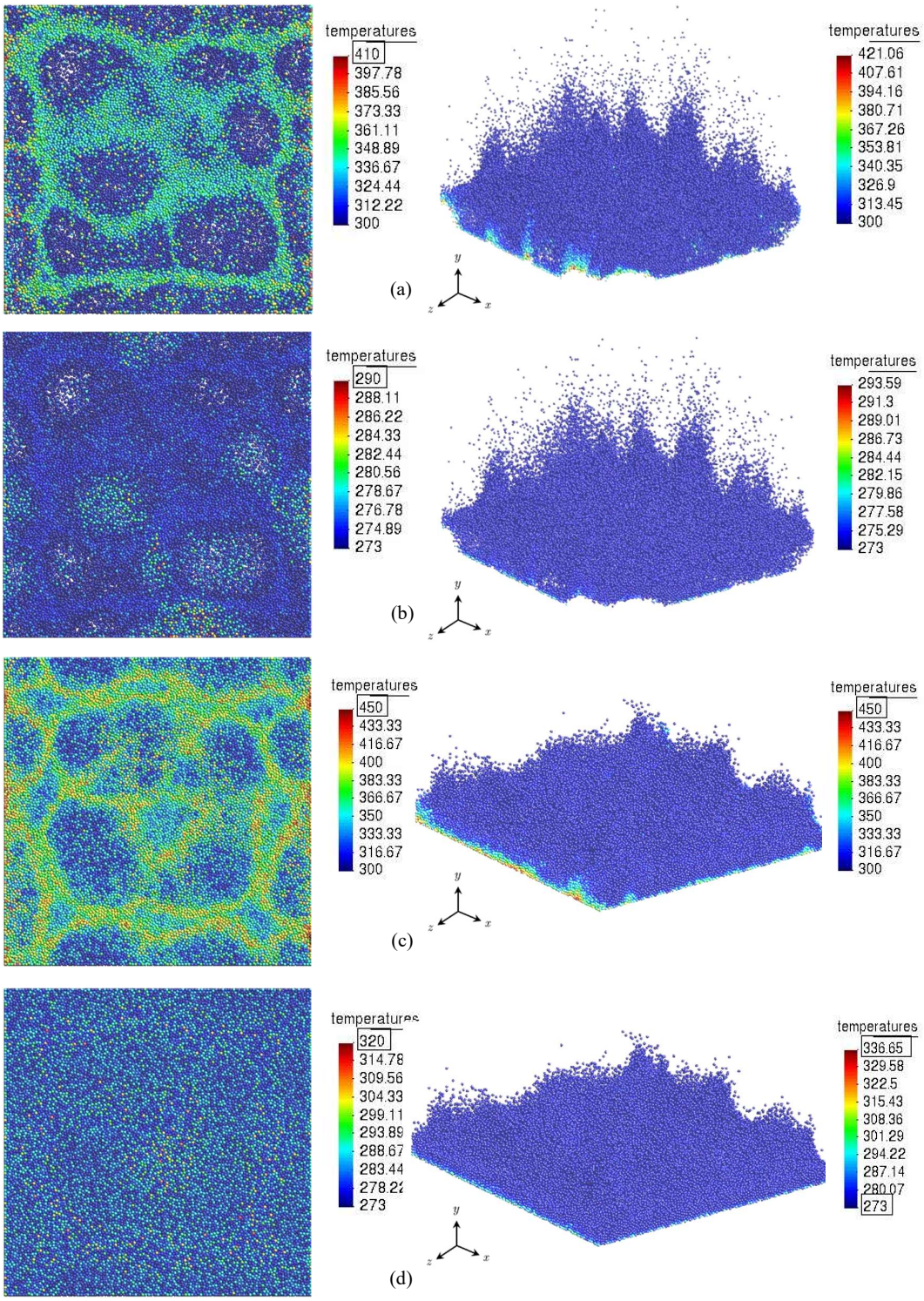

Source: Author.

Figure 39 shows sequences of snapshots as obtained with our simulation for the case with an excitation frequency of $f = 7.8$ Hz and $f = 12$ Hz. With respect to the temperature distribution, like in the two-dimensional example, heat transfer through convection (and radiation) did not allowed the particles to heat up significantly. Notice that the particles located at the lowest layers directly absorb the largest heat flux, whereas the particles at the upper layers exchange more heat with the environment and consequently present a lower temperature distribution (in the case wherein convection and radiation are turned on).

4.10.4 Conduction through a 3D particle assembly

We consider here a three-dimensional particle assembly consisted of $N_P = 10000$ particles randomly packed under gravity within a cubic box, subjected to a temperature gradient of 700 K in its x direction, as depicted in Figure 40.

Figure 40 – Conduction through a 3D particle assembly

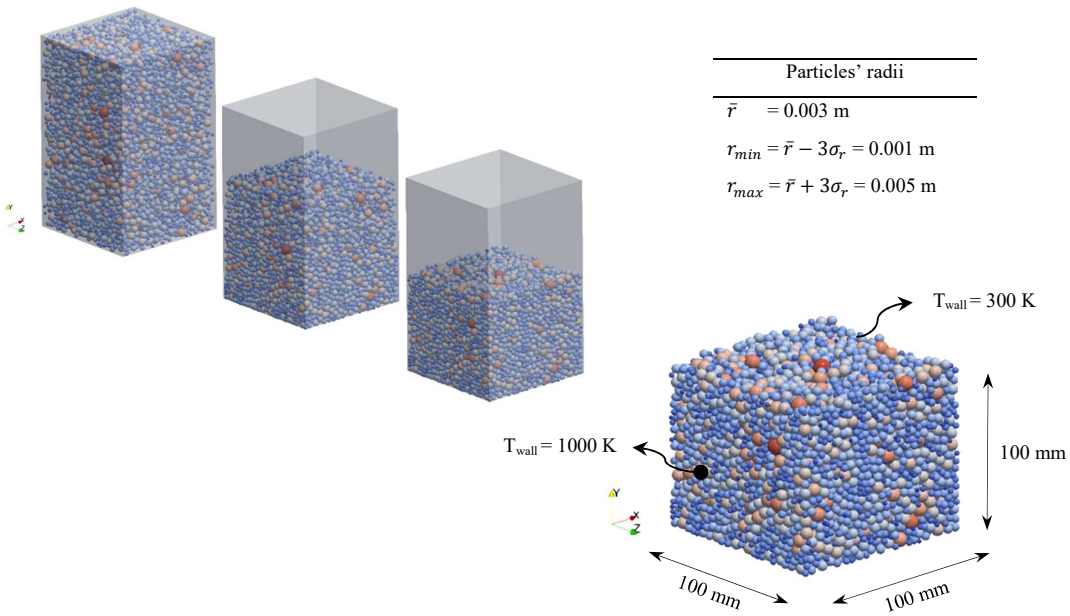

Source: Author.

The box has side dimensions of 100 mm, whereas the particles have radii following a Gaussian distribution with mean $\overline{r} = 3$ mm and std. dev. of 0.6666 mm (the distribution is

truncated at three std. dev. from the mean). The volume fraction of particles within the assembly is 0.54. The thermal gradient is enforced by holding the temperatures of the two opposite walls of the box in the x direction at 1000 K and 300 K indefinitely, respectively, with the particles′ initial temperatures being set at 300 K. By releasing the system at $t = 0$ and computing the evolution of heat flow over time, we are able to ascertain the effective (i.e., bulk) thermal conductivity of the assembly, which is obviously not the same of the individual constituent particles. Convection and radiation are not considered as to isolate the conduction problem and allow for a better estimate. Other data are as follows:

- mass-density of the particles: $\rho =$ 1000 kg/m^3;
- elastic properties of the particles: $E_i =$ 1 MPa (no degrading temp.) and $\nu =$ 0.3;
- friction and rolling resistance coeff. between particles: $\mu_s = \mu_d =$ 0.05 and $\mu_r =$ 0.2;
- friction and rolling resistance coeff. between particles and walls: $\mu_s = \mu_d = \mu_r =$ 0;
- friction and rolling resistances damping rates: $\xi^{con} = \xi^{fric} =$ 1.0 and $\xi^{rol} =$ 0.2;
- thermal properties of the particles: $k_i =$ 100 W/m.K and $C_i =$ 100 J/kg.K;
- time-step size: $\Delta t =$ 2 × 10^{-4} s.

The effective conductivity of the assembly in the $x-$direction, then, may be obtained by $k^* = \Delta Q \big/ \left(\nabla T A \Delta t \right)$, where $\nabla T = 700 \big/ 0.1 = 7000$ K/m is the applied thermal gradient, $A = 0.1 \times 0.1 = 0.01\,\mathrm{m}^2$ is the cross-sectional area to the flow and $\Delta t =$ 350 s is the time interval considered. From this, it follows $k^* =$ 6.2 W/m.K. In order to check the consistency of this result, let us resort to the well-known Hashin-Shtrikman bounds (Hashin and Shtrikman [124] [125] and Hashin [126]) on effective responses for two-phase solid mixtures. For linear heat transfer applications, for a mixture of two isotropic materials, each with known thermal conductivities k_1 and k_2 and volume fractions v_1 and v_2, the bounds for the effective bulk conductivity are

$$k_1 + \frac{v_2}{\dfrac{1}{k_2 - k_1} + \dfrac{1 - v_2}{3k_1}} \leq k^* \leq k_2 + \frac{1 - v_2}{\dfrac{1}{k_1 - k_2} + \dfrac{v_2}{3k_2}}, \tag{124}$$

wherein it is implicitly assumed that $k_1 \leq k_2$. Phase 1 is the matrix (in our case, void) material, whereas phase 2 is the particle one. Provided that the volume fractions and constituent conductivities are the only known information about the mixture′s microstructure, the Hashin-Shtrikman expressions are the tightest bounds for the overall effective responses of two-phase

media, where both constituents are isotropic. One should notice that the lower bound is more accurate for mixtures composed of highly conductive particles surrounded by a lowly conductive matrix (which is the case here), whereas the upper bound is more accurate for mixtures of a highly conductive matrix surrounding lowly conductive particles. For the conductivities adopted here ($k_1 = 0$ and $k_2 = 100$ W/m.K), the above expression renders a lower bound of $k^{*,-} = 0$, and an upper bound of $k^{*,-} = 44.6$ W/m.K. This is entirely consistent with the value derived from our simulation: not only our numerical estimation lies within the bounds, but also it is much closer to the lower (more accurate) one.

Figure 41 – Conduction through a 3D particle assembly. Simulations results

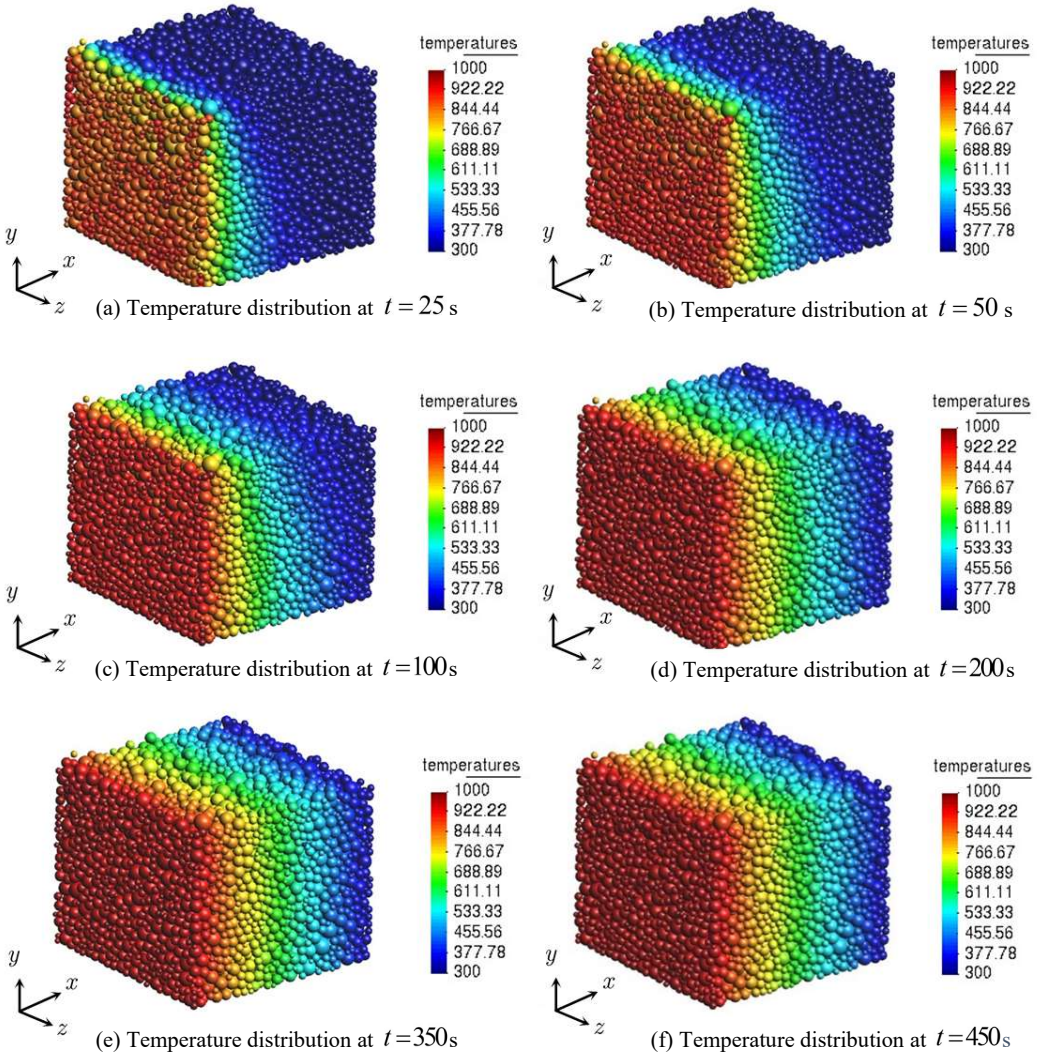

(a) Temperature distribution at $t = 25$ s (b) Temperature distribution at $t = 50$ s

(c) Temperature distribution at $t = 100$ s (d) Temperature distribution at $t = 200$ s

(e) Temperature distribution at $t = 350$ s (f) Temperature distribution at $t = 450$ s

Source: Author.

Figure 41a-f shows snapshots of the system′s configuration at selected time instants as obtained with our simulation. Thermal equilibrium is established at around $t \approx$ 350 s, wherein the particles′ temperatures no longer change significantly between consecutive time steps. From the thermal field thus obtained, the total heat that is provided to the system (ΔQ) until then may be computed by summing up the change in the particles′ individual thermal energies w.r.t. the initial configuration, i.e., $\Delta Q = \sum m_i C_i \Delta\theta_i$. One additional explanation to the fact that the assembly′s effective conductivity shall be closer to the lower bound in this example is that the particles, though occupying roughly 54% of the assembly′s total volume, interact with their neighboring ones through minute contact areas, such that the conductivity paths, although existing within the entire assembly, are of very small cross-sectional size at the particles′ interfaces, thus affecting the conduction rates severely. To further check the consistency of our proposed scheme, we have run one additional simulation of the assembly, now considering thermal softening of the elasticity modulus, in an attempt to increase the particles′ contact areas and thus improve the overall conductivity of the assembly.

By considering a degrading temperature of $\theta^* =$ 300 K, the new thermal field obtained at the time of thermal equilibrium (i.e., when the particles′ temperatures no longer change significantly between consecutive time steps) leads to $k^* =$ 7.4 W/m.K. This is entirely consistent, since it is higher than the first estimate, however still closer to the lower bound. It is important to mention that the increase k^* in this case is indeed expected to be small, since the softening adopted is rather mild. More pronounced increases may be accomplished by softening the particles more severely. At any rate, any estimate to the effective conductivity to this problem shall be biased to the lower bound. The proposed methodology provides a simple and useful way to ascertain the effective thermal conductivity of dry powders and other particulate media used in industrial processes and advanced engineering applications. A similar approach to effective responses, though in the rather different context of particle infiltration into porous media, has been developed by Zohdi and Campello [127].

4.10.5 Laser-sintering of a bed of particles

Let us here validate our model in a laser-sintering application against a reference solution. We consider a model problem of a sintering bed of particles proposed by Ganeriwala and Zohdi [121]. Accordingly, a laser beam with an uniform intensity throughout its cross-sectional area moves following a zig-zag pattern in the $z-$direction across the domain (see Figure 42). To be consistent with the abovementioned reference, no convection, radiation, and thermal softening of the particles´ elasticity modulus will be considered. Moreover, adhesion force as well as thermal interaction of the particles with the base were not considered. A sample of metallic powder consisting of $N_P = 4000$ particles were randomly generated with sizes following a normal distribution with a mean diameter of $\bar{d} = 50$ μm with a std. dev. of 20 μm where the distribution is truncated non-symmetrically w.r.t. $\bar{d}$ (1.5 std. dev. to the left and 2.5 std. dev. to the right) such that all diameters lie in the interval [20μm, 100μm]. The particles were deposited by gravity onto a rigid surface and allowed to settle, as to form a bed with side dimensions of 2 mm × 2 mm.

Figure 42 – Laser-sintering of a bed of particles. Problem definition

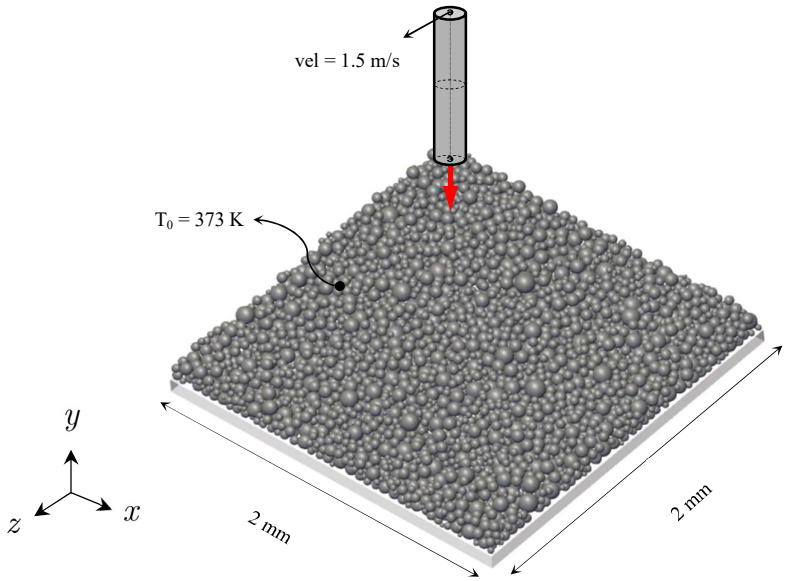

Source: Author.

Other properties used in the simulation as derived from the reference work are summarized in Table 4, except for the material absorptivity and the temperature amplitude of

phase transformation, which were not reported in [121] but could be inferred from the other data provided (these allowed to identify the material as a common metallic powder). It is important to remark that the mechanical part of the reference work, differently from ours, does not take into account the particle's rotations; its contact force is based on a simple linear-spring model (with ad-hoc, manually calibrated stiffness) and the friction model is not fully consistent for stick-slip friction (it does not track the friction history). Nevertheless, this reference serves for comparison purposes, since the particles are somewhat still in this example (meaning that the mechanical fields play a rather secondary role), allowing us to keep the focus on the thermal part of the problem.

Table 4. Laser-sintering of a bed particles. Values used in the simulation

Nº	Parameter	Values
1	Particle´s diameter (mean)	50 μm
2	Number of particles	4000
3	Particles´ initial temperatures	373 K
4	Particles´ material density	7800 kg/m^3
5	Particles´ elastic modulus (solid) and Poisson coeff.	193 GPa and 0.26
6	Particles´ elastic modulus (liquid phase)	1.70×10^{-6} GPa
7	Particles´ damping rates	1.0
8	Friction and rolling resistance coeff. between particles	$\mu_s = \mu_d = 0.1$ and $\mu_r = 0.01$
9	Friction and rolling resistance coeff. between particles and walls	$\mu_s = \mu_d = 0.1$ and $\mu_r = 0.01$
10	Bed´s lateral dimensions	2 mm x 2 mm
11	Laser power	200 W
12	Laser beam diameter	0.5 mm
13	Laser beam velocity	1.5 m/s
14	Melting and vaporization temperature	1800 K and 3500 K
15	Material absorptivity and coeff. of thermal expansion	0.96 and 1.56×10^{-5} K^{-1}
16	Temperature amplitude of phase transformation	180 K (10% of melting temperature)
17	Particles´ thermal conductivity (solid, liquid)	40 W/m K, 60 W/m K
18	Particles´ specific heat (solid, liquid)	600 J/kg K, 900 J/kg K

Source: Ganeriwala and Zohdi [116] [121]

The time-step size adopted, considering that the particles are very stiff, was of $\Delta t = 2\times10^{-8}$ s for the initial deposition stage and of $\Delta t = 5\times10^{-9}$ s for the laser sintering

stage, taking into account that we are considering phase transformation of the material. The total simulation time was of $t_F = 6.8 \times 10^{-3}$ s.

Figure 43 – Laser-sintering. a) 8.5×10^{-4} s b) 2.55×10^{-3} s c) 4.59×10^{-3} s d) 6.8×10^{-3} s. Temperature range from 400 to 3000 K

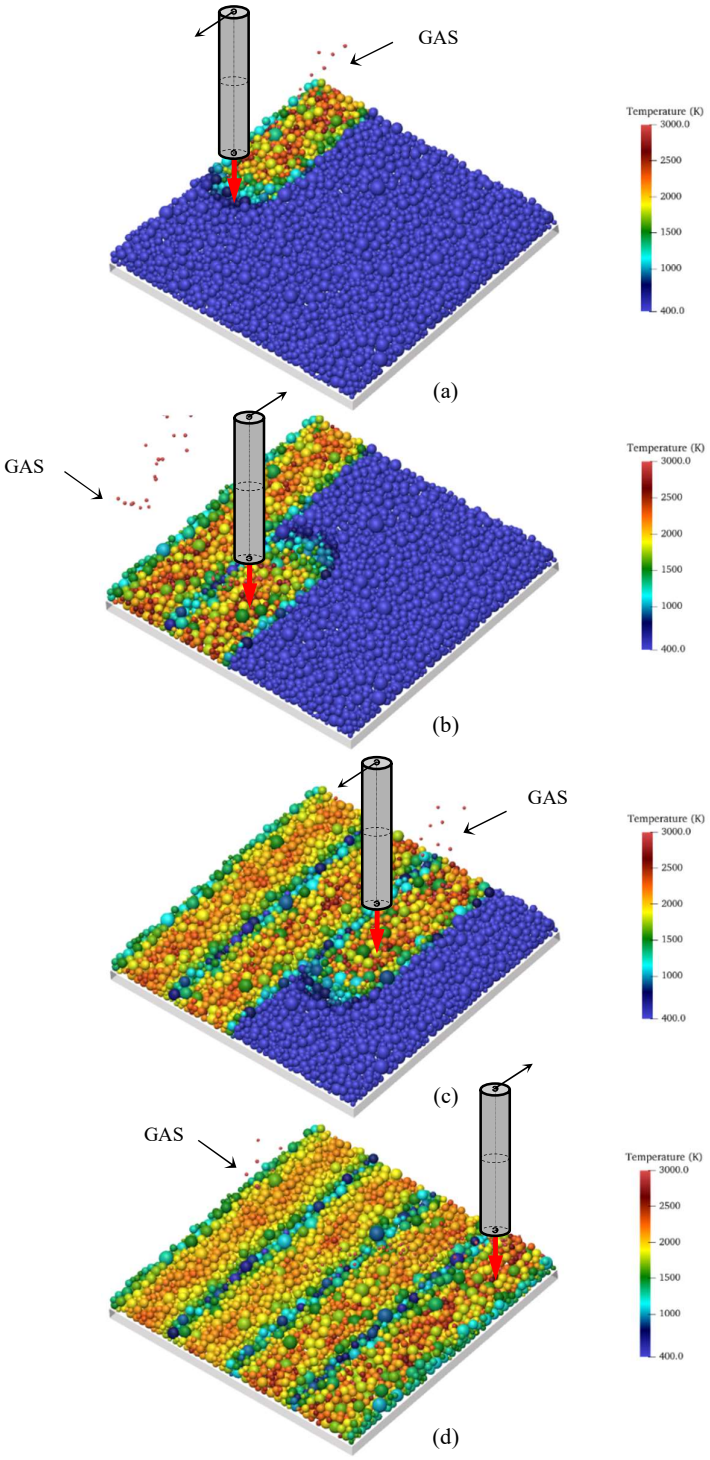

Source: Author.

Figure 43 shows a sequence of screenshots at selected time instants as obtained with our simulation. From this figure, it can be seen that those particles located near the boundaries of the beam´s path-length heat up less than those further within the path, due to conduction with the cooler neighboring particles. Moreover, some particles are seen to be severely heated and reach the vaporization temperature (especially the smaller particles), turning into gas. According to our strategy, they "boil up" out of the bed to the environment and no longer participate in the sintering process (these particles are given a small upward velocity as to escape from the bed, they can be seen in the Figure 43 with the legend "GAS"). Figure 44a display the average temperature of the entire bed of particles as a function of time as compared with the reference work, showing a pretty good agreement between them. Note that short periodic plateaus are observed, corresponding to the occasions when the laser passes out of the domain before it reverses direction and re-enters the bed.

Figure 44 – Temperature distribution as a function of simulation time. a) Comparison of average temperature of entire powder bed with reference work. b) Influence of thermal expansion

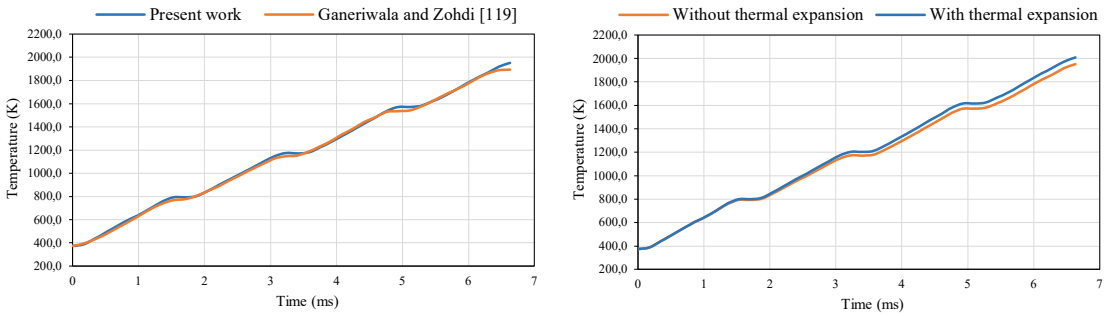

Source: Author.

As a curiosity, we have run one more simulation of the assembly, using the results of our previous simulation as reference, but now considering thermal expansion (or contraction) of the particles in an attempt to analyze the influence of this parameter in the thermal field of the entire powder bed. As we can see in Figure 44b, as a result of small rearrangements in the bed´s structure due to the particles´ expansion, only a small increment on the overall average temperature is observed (~3% at the final time).

Chapter 5

Numerical simulation of AM processes: selective laser sintering

In this chapter, we provide some numerical simulations to illustrate how our model can be applied to the simulation of AM processes and, in particular, selective laser sintering. Firstly, we calibrate the particles´ properties with a simple example from the literature, for which both numerical and experimental results are known. Then, we proceed to analyze more general examples, using the model parameters that have been just calibrated in the first example. Differently from the last example of Chapter 4, here we are including adhesion forces between the particles (using the model introduced in Chapter 3) and a Gaussian laser beam for the external heating device (this is the type of laser that is most frequently used in industrial selective laser sintering processes). For the time integration, we adopt the forward Euler version of the scheme $(\phi = 0)$, in which the time step is given by equation (90). The chosen material for the metallic powder particles is 316L stainless steel (316L SS), which is usually adopted by manufacturers in SLS processes.

5.1 Calibration and preliminary studies

Let us calibrate the particles´ properties using the results of Ganeriwala and Zodhi [116], which in turn is a recreation of an experiment conducted by Khairallah and Anderson [91]. Accordingly, a layer of metallic powder consisting of $N_P = 600$ 316L SS particles were randomly generated with sizes following a Gaussian distribution with a mean diameter of

$\overline{d} = 27$ µm and std. dev. of 3.5 µm (the distribution is truncated at three std. dev. such that all diameters lie in the interval [16.5µm, 37.5µm]).

Table 5. Material properties for 316L SS as a function of temperature

Temperature (K)	Specific heat (J/kg K)	Thermal conductivity (W/m K)	Density (kg/m^3)	Elasticity modulus (GPa)
293	452	13.3	7952	198
366	485	14.3	7919	194
478	527	15.9	7877	185
589	548	17.5	7831	177
700	565	19.0	7786	167
811	573	19.8	7739	157
922	586	21.9	7692	148
1033	615	23.2	7640	137
1144	649	24.6	7587	129
1255	690	26.2	7537	120
1700 (liquid)	815	32.4	7300	1.70×10^{-6}

Source: AK Steel [128] and INCO [129]

Table 6. Values used in the simulation

Nº	Parameter	Values
1	Particles´ elastic modulus (room temperature) and Poisson's ratio	198 GPa and 0.26
2	Particles´ friction and rolling resistance coeffs.	0.1
3	Particles´ damping rates	0.1
4	Convection (or film) coefficient	40 W/m^2 K
5	Melting and boiling temperature	1700 K and 3130 K
6	Latent heat of melting	2.99×10^5 J/kg
7	Latent heat of vaporization	6.09×10^6 J/kg
8	Material emissivity and absorptivity	0.33
9	Laser power and distribution factor (f)	200 W and 2
10	Laser scan speed	2.0 m/s
11	Laser spot size	54 µm
12	Powder bed porosity	0.57
13	Preheat particles´ temperature	363 K
14	Environment temperature	363 K
15	Temperature amplitude for phase transformation	170 K (10% of melting temperature)

Source: Ganeriwala and Zohdi [116]

The particles were dropped and deposited into a 1.0 mm × 0.5 mm domain and allowed to settle by gravity for 0.1 s, see Figure 45. The process begins with a Gaussian laser beam of cross-sectional diameter 0.108 mm scanning over the layer in a single pass from a normal direction (orthogonal to the $x-z$ plane) along the $x-$coordinate. The material properties (mechanical and thermal) for 316L SS as a function of temperature and phase are depicted in Table 5 (values in between the specified ranges are obtained through Lagrangian interpolation). Other parameters used in the simulation are given in Table 6 (these are the same as adopted by Ganeriwala and Zohdi [116]). According to the reference example, adhesion force, thermal expansion, as well as thermal interaction of the particles with the base were not considered.

Figure 45 – Deposition of particles and problem definition

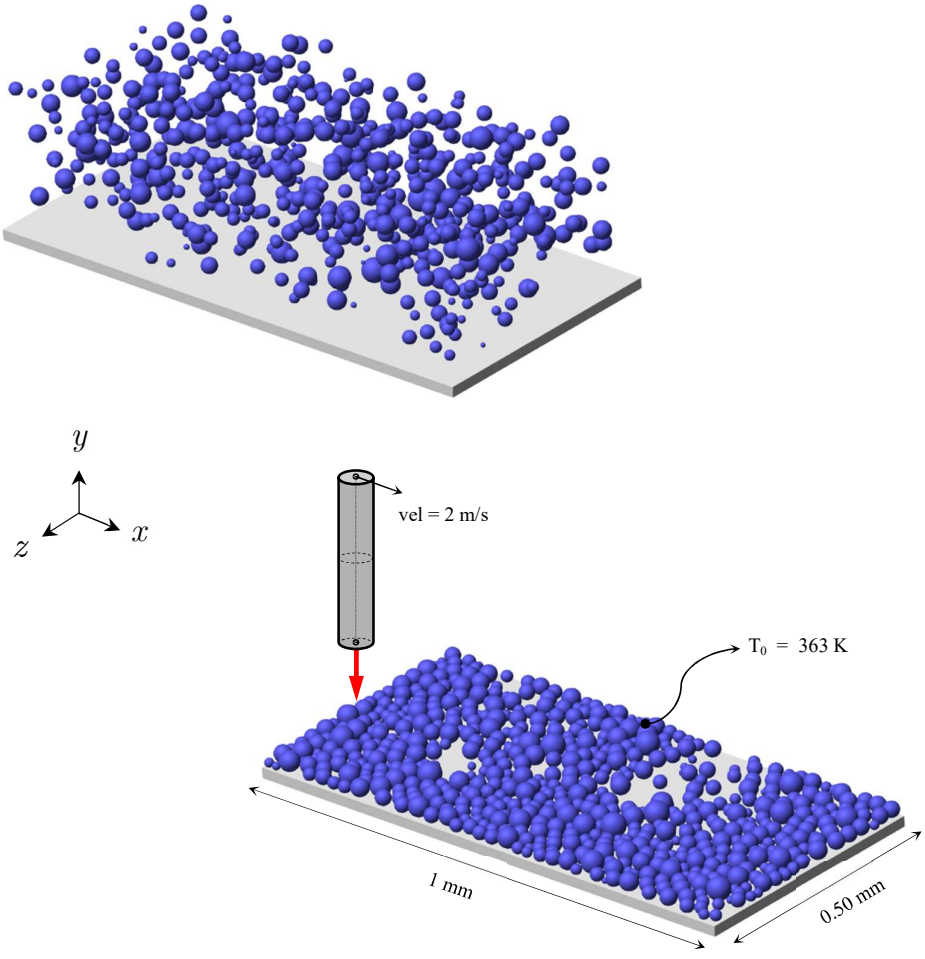

Source: Author.

Figure 46 shows the temperature distribution of the particles as obtained from our simulation just after the laser has passed (time instant $t =$ 0.0005 s). We used the melt pool width as a reference to compare our results, and in accordance with the reference work, measured in the middle of the domain $x = L_x/2 =$ 0.5 mm to avoid the boundary conditions effects. The melt pool width is an important parameter in AM processes because it determines how the overlapping conditions can affect the microstructure of an AM part. In this sense, in Figure 47 we show a comparison between the present and the reference work of the melt pool width varying the laser power at a constant speed. A very good correlation is observed, which testifies that the model parameters are satisfactorily calibrated.

Figure 46 – Top view after the laser passed over. Laser power: 200 W

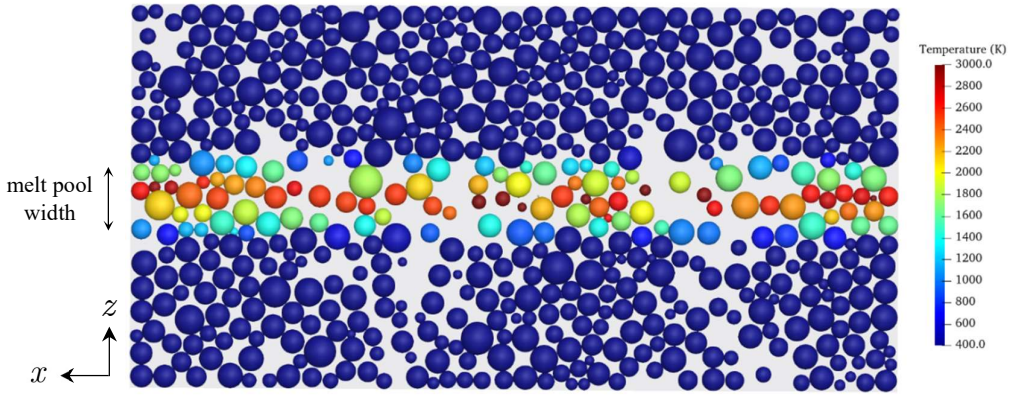

Source: Author.

Figure 47 – Comparison of the melt pool size as a function of laser power

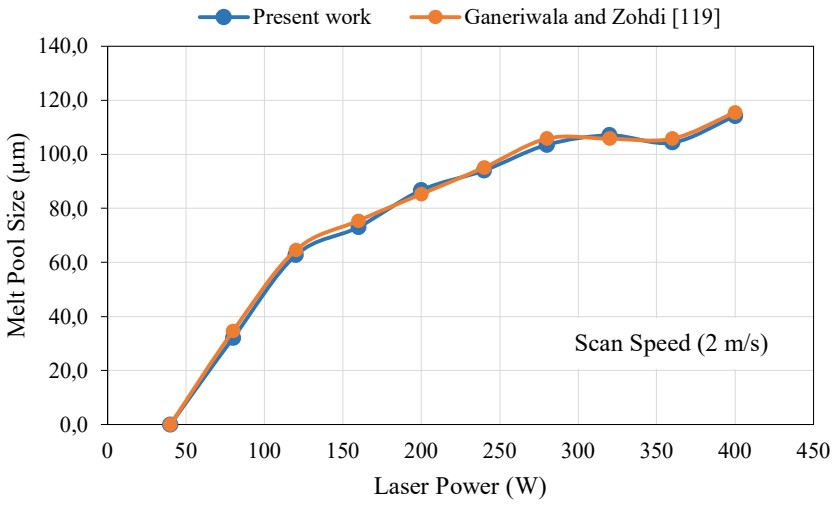

Source: Author.

5.2 Laser sintering of a bed of particles

In this example, we repeat the same problem setting as in example 4.10.5 of Chapter 4, however now taking the material properties of real metallic powders (varying as a function of temperature and phase) that are typically used in industrial PBF techniques (i.e., those from Table 5 and Table 6, except the diameter of the laser which is the same of the example 4.10.5), and considering the appropriate (i.e., Gaussian) type of laser. Our intention is to see the difference on the results (as compared to example 4.10.5) when the simulation is performed with real material properties and laser type as used in AM processes. The particle size distribution, as well as the std. dev. adopted are the same of the previous example[9], resulting in $N_P = 12000$ 316L SS particles for a 2 mm × 2 mm bed domain. As in the reference example, the laser moves in a zig-zag pattern across the length of the domain (see Figure 48). For the Gaussian laser beam, the value of the distribution factor considered was $f = 1.66$, which corresponds to the equivalent amount of energy of a laser with a uniform cross-sectional intensity distribution and same nominal power. Again, adhesion force, thermal expansion, as well as thermal interaction of the particles with the base were not considered, as to be consistent with example 4.10.5.

Figure 48 – Laser-sintering of a bed of particles. Problem definition

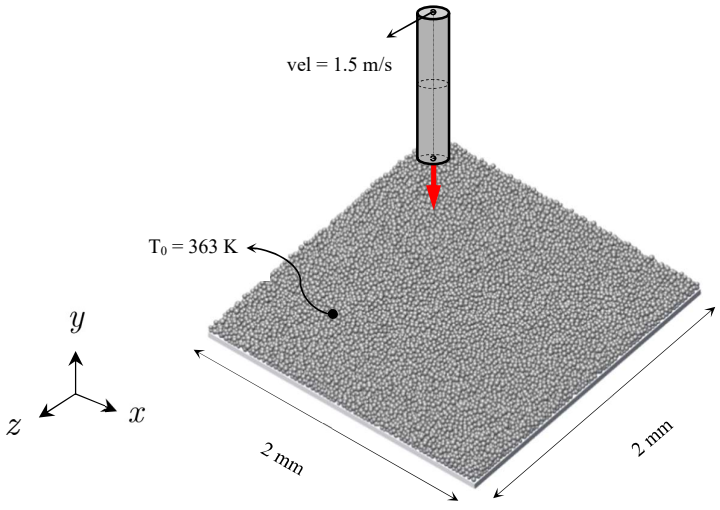

Source: Author.

[9] The particle size used in most PBF techniques are usually in the range of 10 to 60 μm, see Milewski [81].

Figure 49 – Temperature distribution as a function of simulation time. Comparison of average temperature of entire powder bed with reference work (example 4.10.5)

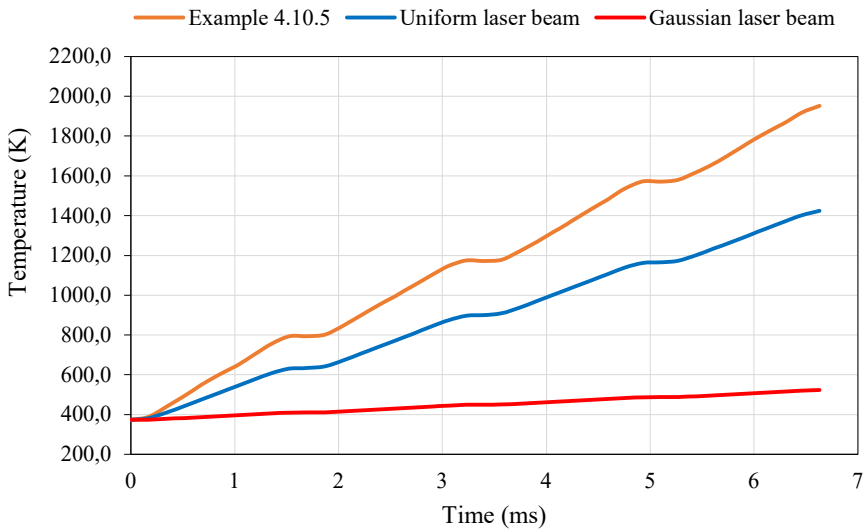

Source: Author.

Figure 49 shows the average temperature of the particles as obtained in the present simulation (red line), along with results obtained by considering a uniform laser beam of same nominal power and resultant energy (blue line). Results from example 4.10.5 are also shown for comparison. By adopting real material properties, a significant difference in the temperature distribution is observed when compared to 4.10.5, especially when the Gaussian laser beam is used, for which it can be seen that no particle reached the temperature criterion to change its phase from solid to another state. We found two main reasons that can explain this difference: firstly, the value of the absorptivity is much smaller here than in the reference example, so a less amount of energy is absorbed by the particles. Secondly, the intensity of the Gaussian laser beam decays to its sides in a nonlinear shape, in contrast to the uniform beam, so the energy is concentrated in a smaller region in each scan. When the intensity of the laser beam is assumed to be uniform, yet with the same resultant energy of the Gaussian beam, the average temperature increases quite markedly, as we can see in Figure 49 (blue line).

5.3 Simulation of a metal manufactured prototype ring using SLS process

In this example, with the calibrated model parameters as obtained in example 5.1, we simulate a sintering-based AM process to build a ring-like part of mean diameter $d =$ 1.0 mm (measured from the center to the circular axis, see Figure 50a). The particles´ dimensions are the same of the previous examples and the material properties are depicted in Table 5 and Table 7.

Table 7. Values used in the simulation

Nº	Parameter	Values
1	Particles´ elastic modulus (room temperature) and Poisson's ratio	198 GPa and 0.26
2	Particles´ friction and rolling resistance coeffs.	0.5
3	Particles´ damping rates	0.9
4	Adhesion parameters ξ^{bond}, α^{adh} and $\varepsilon_{ij,\mathrm{eq}}$	1.0, 1.0 and 0.01
5	Sintering, melting and boiling temperature	1200K, 1700 K and 3130 K
6	Latent heat of melting	2.99×10^5 J/kg
7	Latent heat of vaporization	6.09×10^6 J/kg
8	Material emissivity and absorptivity	0.33
9	Laser scan speed	4000 rad/s
10	Laser spot size	120 μm
11	Powder bed porosity	0.55
12	Preheat particles´ temperature	363 K
13	Environment temperature	363 K
14	Temperature amplitude for phase transformation	170 K (10% of melting temperature)

Source: Author

The type of laser used was the Gaussian laser beam with a cross-sectional diameter of $d =$ 0.24 mm scanning over the particle bed with a constant velocity of 4000 rad/s and following a circular pattern motion (see, Figure 50b). For the adhesion force, besides of the bonding in the normal direction, we include a tangential adhesion force and a rotational adhesion moment. Following the same framework of stick-slip friction (see equation (23)) we have

$$\boldsymbol{f}_{ij}^{bond,\tan} = k_{bond,\tan}\Delta\boldsymbol{x}_{ij}^{\mathrm{trial}} - d^{bond,\tan}\boldsymbol{v}_{ij,t}\ , \tag{125}$$

where $\boldsymbol{f}_{ij}^{bond,\tan}$ is the adhesion force in the tangential direction and $k_{bond,\tan}$ is the adhesion stiffness in the tangential direction. According to Xin et al. [117], this value can be taken as fraction of the adhesion stiffness in the normal direction, i.e., $k_{bond,\tan} = \eta k_{adh}$, where η is usually the Poisson's ratio of the granular assembly (an approach about how to consider the value of η can be found in Walton [130]), $\Delta \boldsymbol{x}_{ij}^{\text{trial}}$ is the pair´s trial adhesion deformation in the tangential direction and $d^{bond,\tan}$ is a friction tangential damping constant (analogous to d^{con} in equation $(22)_1$ and d^{fric} in equation (23)), such that

$$d^{bond,\tan} = 2\xi^{bond}\sqrt{m^* k_{bond,\tan}}. \tag{126}$$

where ξ^{bond} is the damping rate of the oscillation (the same used in equation (86)). For the rotational adhesion moment, following the same framework of the rolling resistance model, we have

$$\boldsymbol{m}_{ij}^{bond,rol,\tan} = -k^{bond,rol,\tan}\Delta\boldsymbol{\theta}_{ij}^{\text{trial}} - d^{bond,rol,\tan}\boldsymbol{\omega}_{ij}, \tag{127}$$

where $\boldsymbol{m}_{ij}^{bond,rol,\tan}$ is the rotational adhesion moment, $\Delta\boldsymbol{\theta}_{ij}^{\text{trial}}$ is the pair´s trial adhesion rotation (the same of equation (35)), $k^{bond,rol,\tan}$ is the stiffness of the rotational spring, and $d^{bond,rol,\tan}$ is a rolling damping constant (analogous to the rolling resistance constants in equations (34) and (36)), given by

$$k^{bond,rol,\tan} = k_{bond,\tan}(r^*)^2 \quad \text{and} \quad d^{bond,rol,\tan} = \xi^{bond}\sqrt{j^* k^{bond,rol,\tan}}. \tag{128}$$

According to Shi et al. [131], an appropriate scanning strategy contributes to reduce distortion, anisotropy and porosity on the final manufactured piece. Moreover, helps to define the proper hatch spacing (distance between laser passes), which is particularly important to avoid improper bonding between particles and undesired cooling and solidification. To assess some of these issues, we run a series of simulation varying the distribution factor f and the nominal power P_0 of the laser, while keeping the scanning speed fixed. Our interest is to find the ideal combination that will guarantee a proper bonding between particles, a coherent and uniform width of the ring, while ideally requiring less energy from the laser. The values of P_0 adopted in the simulation was: 50 W, 100 W, 150 W, 200 W and 250 W with f varying from 1 up to 4 for each value of P_0. The simulation time was $t =$ 0.00628 s which gives four laps of scanning of the laser.

Figure 50 – Laser-sintering of a prototype metal ring. Problem definition.
a) Top view b) isometric view

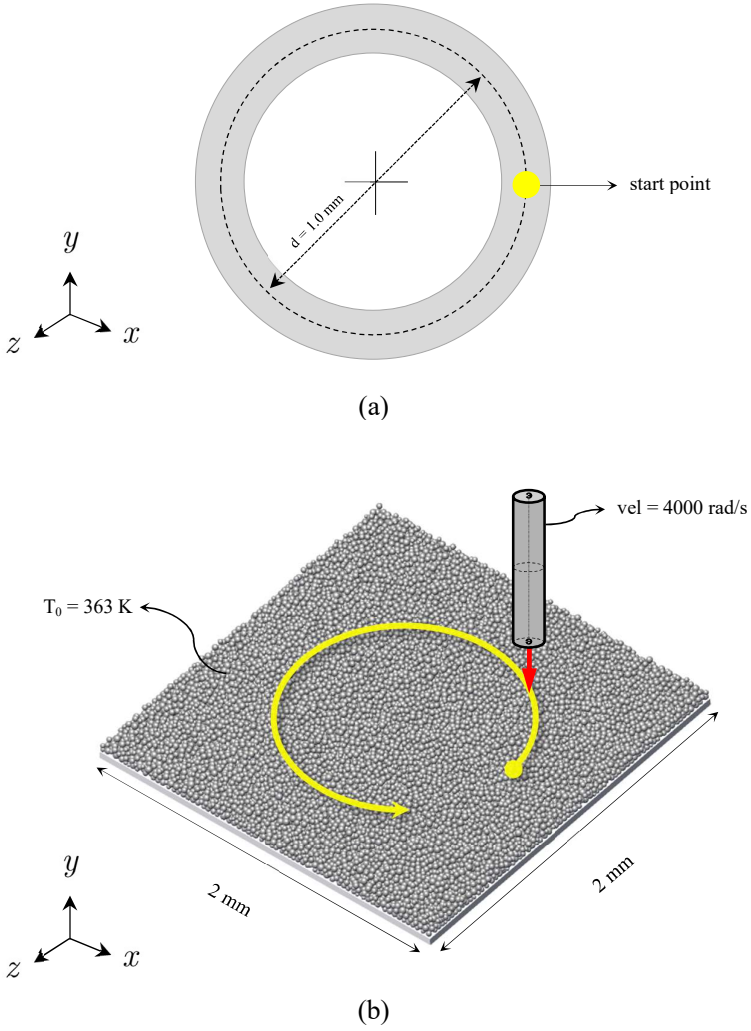

Source: Author.

An inert gas is considered as the surrounding atmosphere of the simulation, this is a typical practice in SLS processes to avoid oxidation that would affect the melting and consolidation of the metal particles. For the bonding criterion, besides those presented in Chapter 3, we include a temperature criterion, whereby for a contacting pair $i - j$ the temperatures of both particle i and particle j must be higher than a specified critical temperature value (which is the sintering temperature) for the bond to be activated between them[10].

[10] The same criterion is adopted by Xin et al. [117].

Figure 51 – Snapshots of temperature distribution at selected time instants as obtained with our simulation for the case with $P_0 = 250$ W and $f = 2$

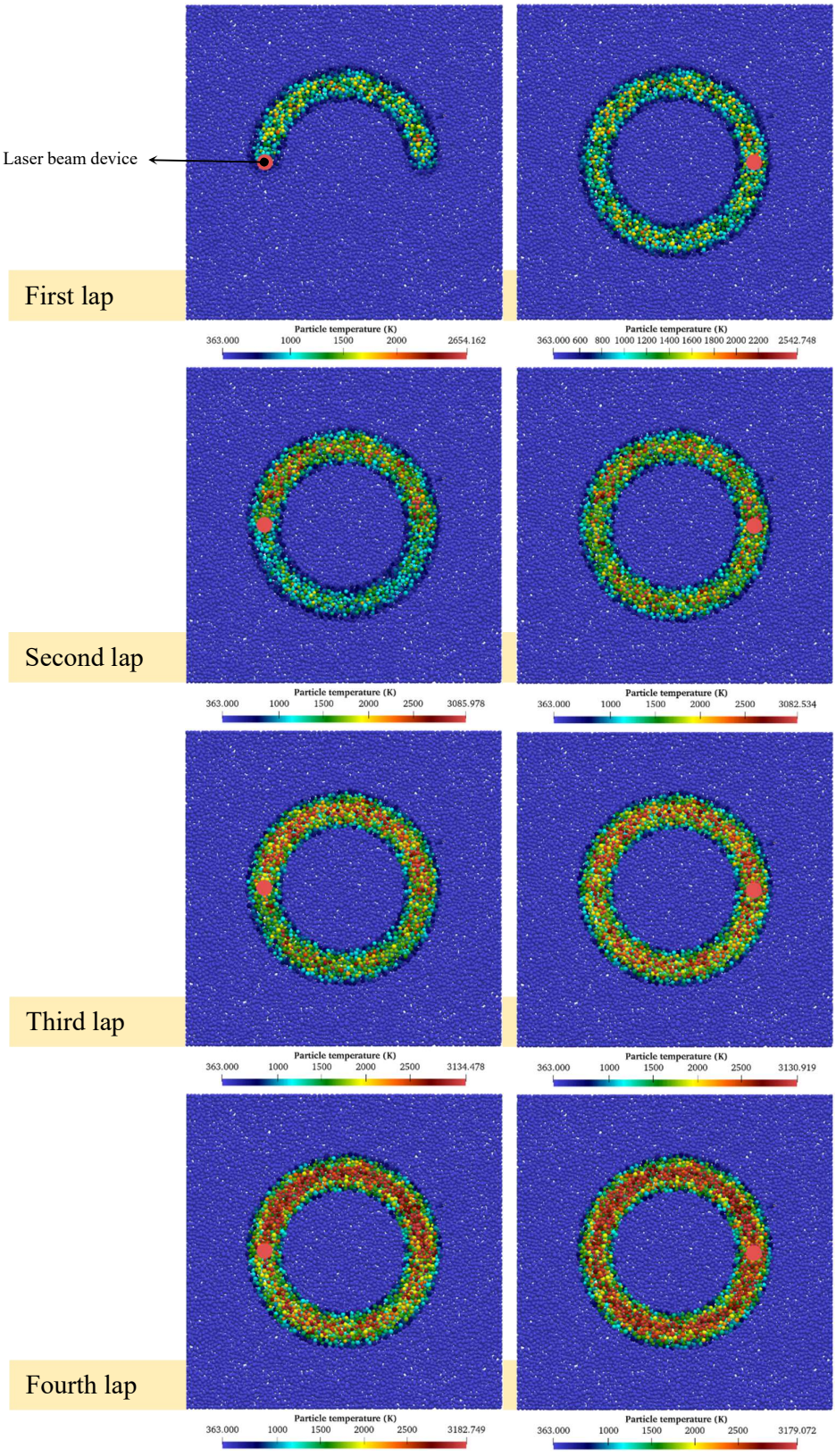

Source: Author.

Figure 52 – Temperature distribution as a function of laser nominal power and distribution factor at the end of the fourth lap (t = 0.00628 s)

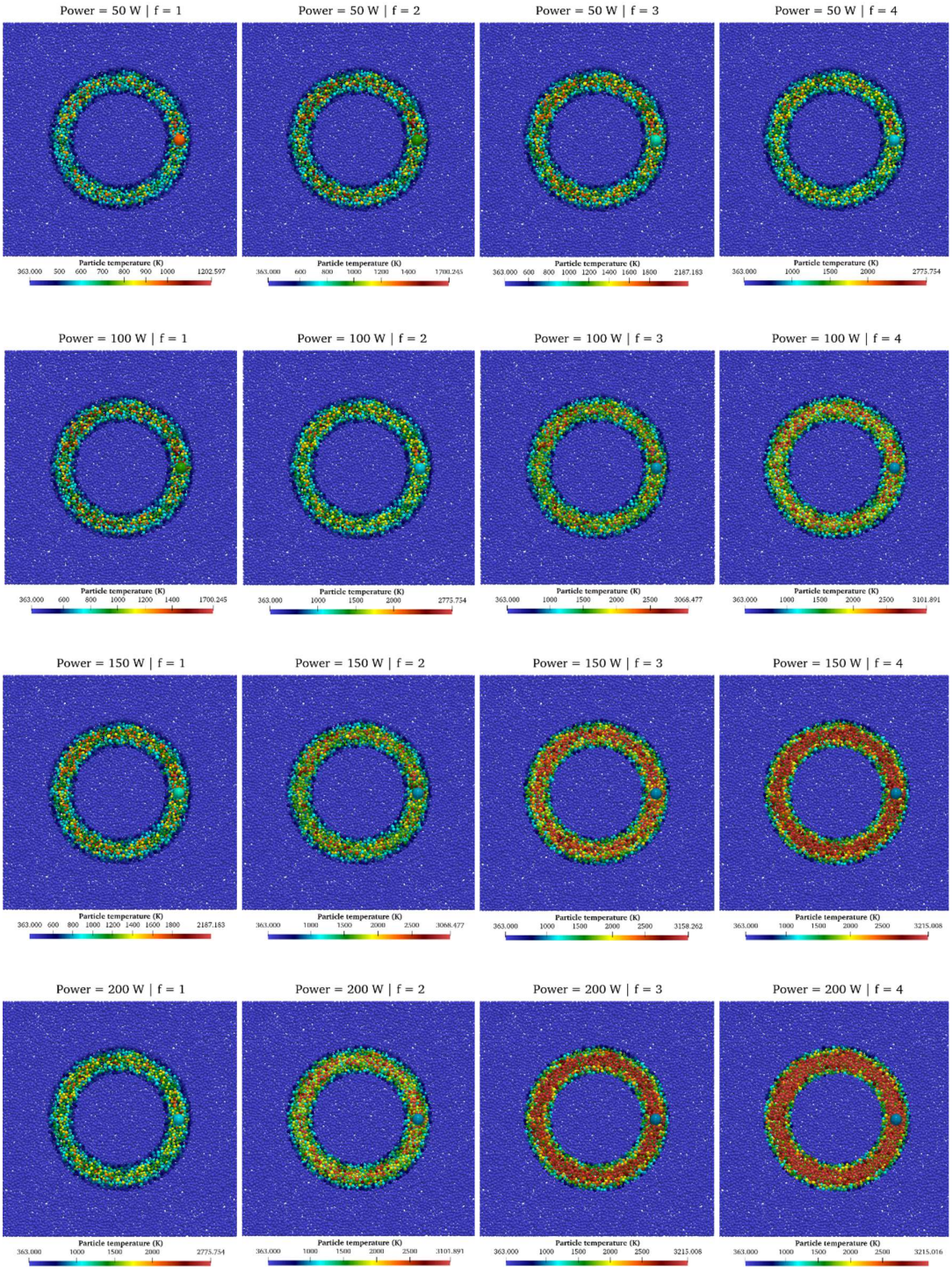

Source: Author.

Figure 53 – Temperature distribution as a function of laser nominal power and distribution factor at the end of the fourth lap (t = 0.00628 s)

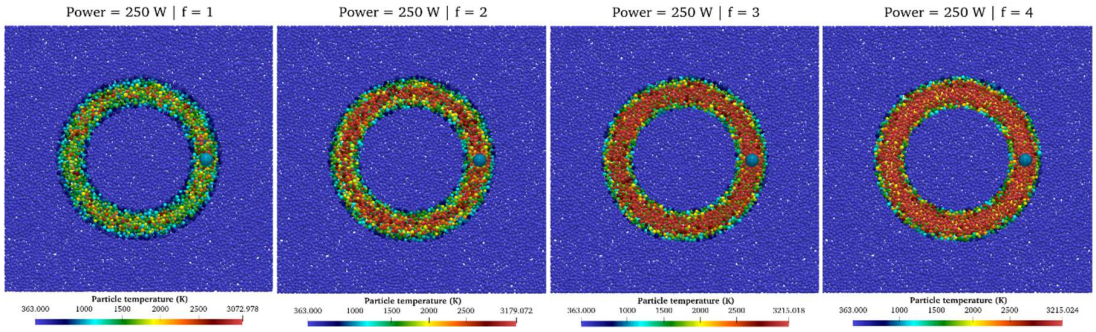

Source: Author.

Table 8. Summarized temperatures obtained in the simulation at the end of the fourth lap (t = 0.00628 s)

Power (W)	Distribution factor (f)	Temperature (K)	
		Average	Maximum
50	1	393.746	1202.597
	2	421.861	1700.245
	3	446.556	2187.183
	4	469.193	2775.754
100	1	421.861	1700.245
	2	469.193	2775.754
	3	510.517	3068.477
	4	544.580	3101.891
150	1	446.556	2187.183
	2	510.517	3068.477
	3	593.937	3158.262
	4	638.484	3215.008*
200	1	469.193	2775.754
	2	544.580	3101.891
	3	638.484	3215.008*
	4	676.584	3215.016*
250	1	515.539	3072.978
	2	610.789	3179.072
	3	668.344	3215.018*
	4	707.237	3215.024*

* Gas phase

Source: Author

If only one of the two criteria is satisfied (e.g., only the overlap criterion), there will be no adhesion and purely Hertzian contact force will act. Adhesion of the particles with the base is not considered, since this is an undesired effect in the manufacturing process. Cooling by convective and radiative heat transfer is computed only for the particles located in the top surface. Figure 51 shows a sequence of snapshots of the powder bed at selected time instants as obtained in a typical simulation (results shown are for the case with $P_0 = 250$ W and $f = 2$; other cases are omitted for conciseness). Figure 52 and Figure 53 shows the final configurations for each case after four laps ($t =$ 0.00628 s). Table 8 summarizes the average and maximum temperatures reached by the powder bed at the final lap. As we can see, values with equivalent intensity I_0 (i.e., according to equation (116), a power of 50 W with $f = 2$ is equivalent to a power of 100 W with $f = 1$) gives the same temperature distribution, as expected. According to our algorithm, the gas phase is reached when the temperature is higher than 3215 K. Figure 54 shows a side view of the bed at the end of the fourth lap for the cases where gas particles are observed (for the sake of conciseness we will not show results with equivalent I_0).

Figure 54 – Particles with gas phase

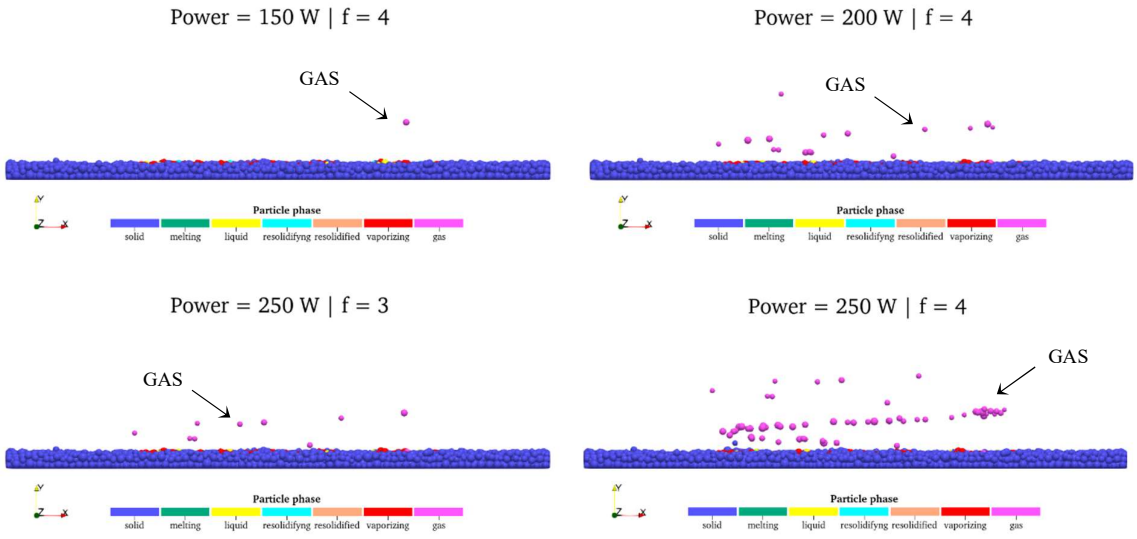

Source: Author.

Let us analyze quantitatively the results following the same criterion of laser power (W) and distribution factor (f). We are interested in finding which combination of parameters gives the best final sintered piece. Accordingly, we adopt as a parameter the mean width $\overline{w}$

and the mean height $\bar{h}$ of the ring measured at eight sections as shown in Figure 55 and computed according to equation (129).

$$\bar{w} = \frac{1}{8}\sum_{i=1}^{8} w_i \quad \text{and} \quad \bar{h} = \frac{1}{8}\sum_{i=1}^{8} h_i \,. \tag{129}$$

Figure 56, Figure 57, Figure 58 and Figure 59 shows snapshots of the sintered piece as obtained with our simulations for each case and Figure 60 summarizes the number of particles that satisfied the bonding criterion for each case. Again, for the sake of conciseness we will not show the results with equivalent I_0.

Figure 55 – Sintering ring-like part. Ring width and height definition

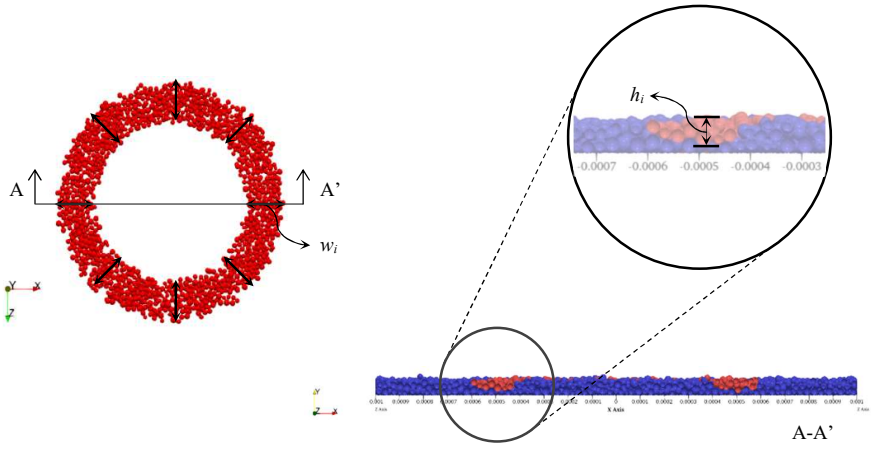

Source: Author.

Figure 56 – Final sintered piece after four laps for the case with P_0 = 50 W and f = 4. From left to right: top view of the particle bed, top view of the piece (only bonded particles shown), side view of the piece

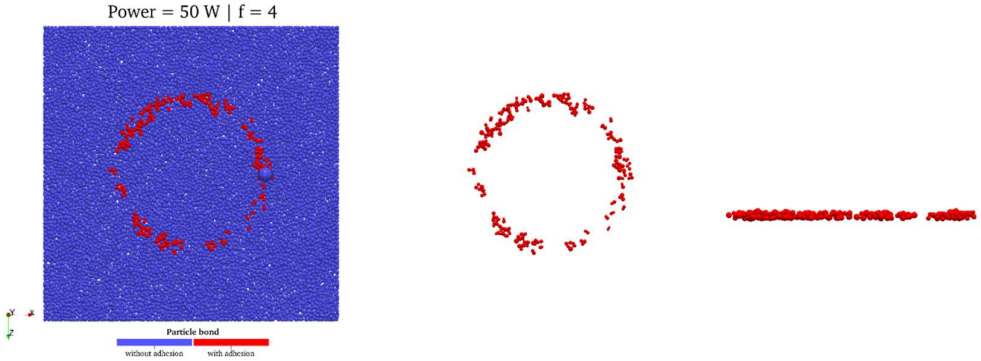

Source: Author.

Figure 57 – Final sintered piece after four laps for the cases with P_0 = 100 W, 150 W and f = 3 and f = 4. From left to right: top view of the particle bed, top view of the piece (only bonded particles shown), side view of the piece

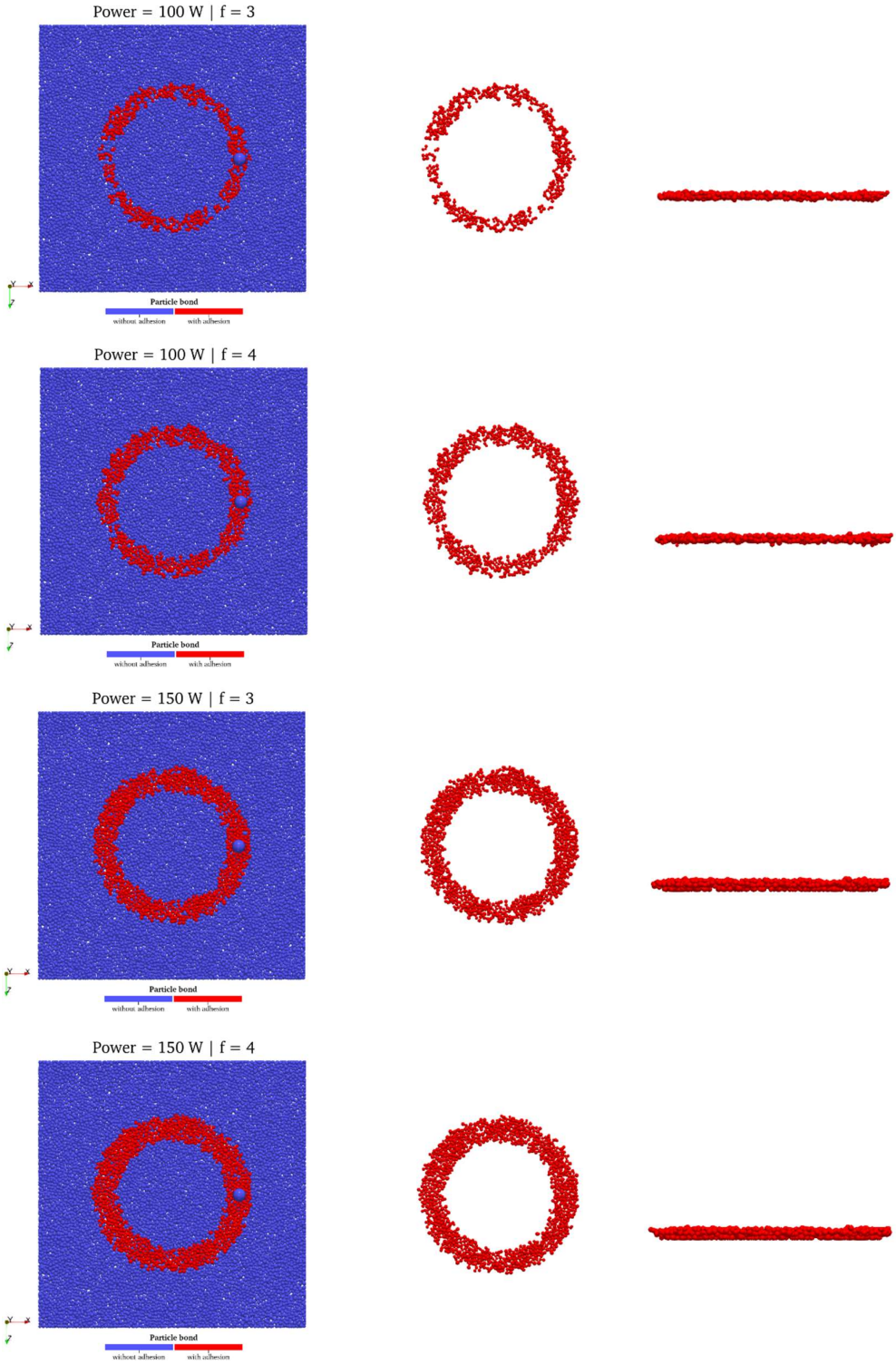

Source: Author.

Figure 58 – Final sintered piece after four laps for the cases with $P_0 = 200$ W and $f = 4$ and $P_0 = 250$ W and $f = 1$ up to $f = 3$. From left to right: top view of the particle bed, top view of the piece (only bonded particles shown), side view of the piece

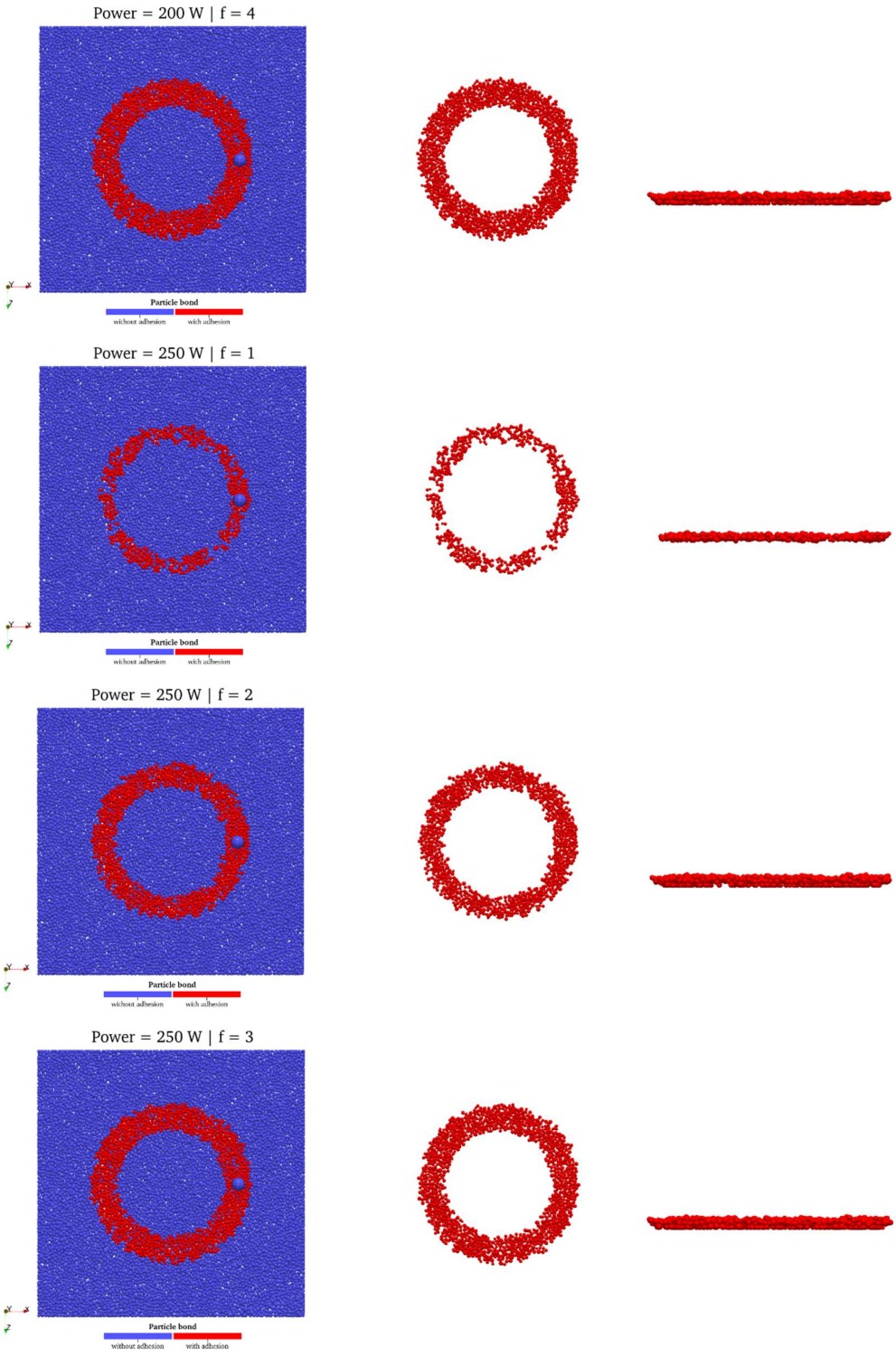

Source: Author.

Figure 59 – Final sintered piece after four laps for the case with $P_0 = 250$ W and $f = 4$. From left to right: top view of the particle bed, top view of the piece (only bonded particles shown), side view of the piece

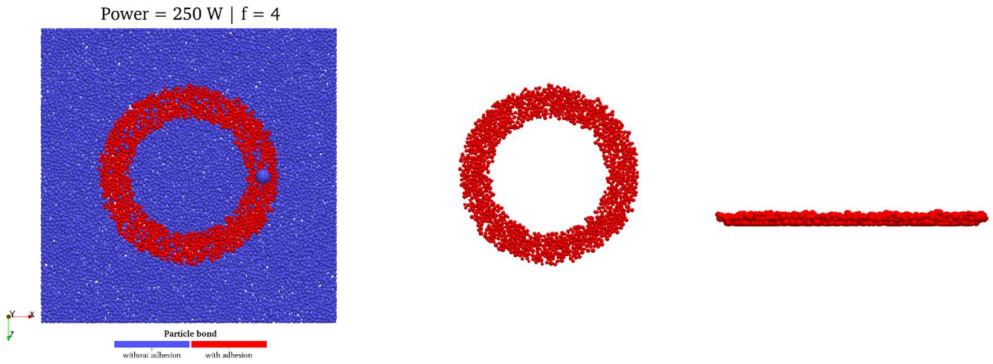

Source: Author.

Figure 60 – Summary of the number of particles with adhesion for each case

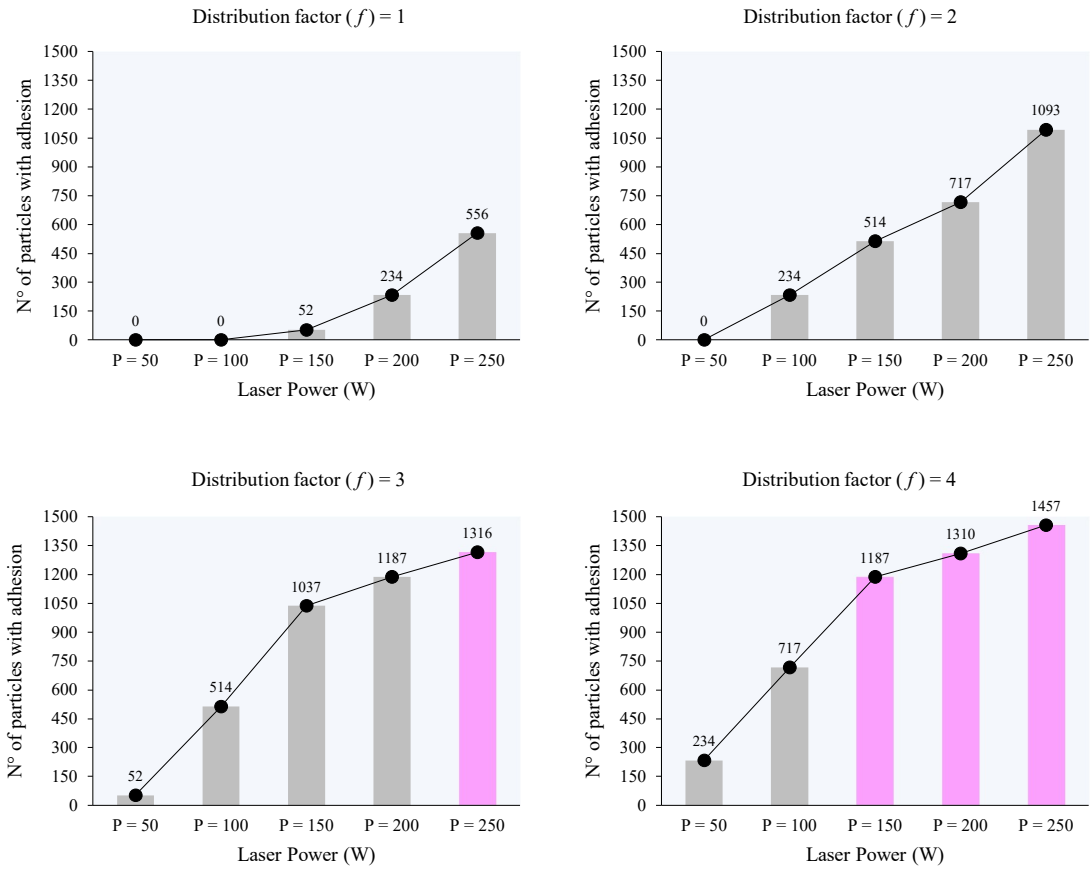

Source: Author.

Figure 61 – Ring width as a function of laser power and distribution factor

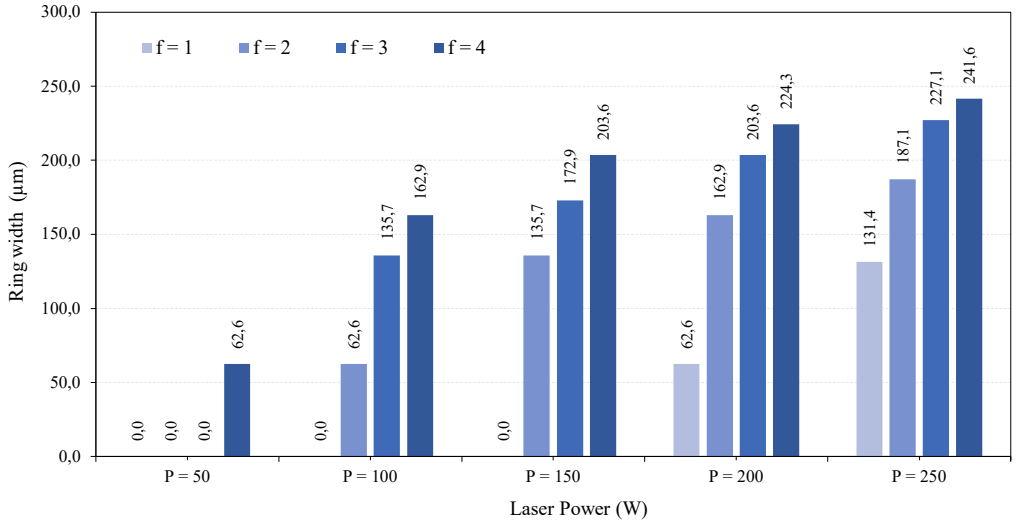

Source: Author.

Figure 62 – Summary of the width and height of the ring as a function of the nominal power

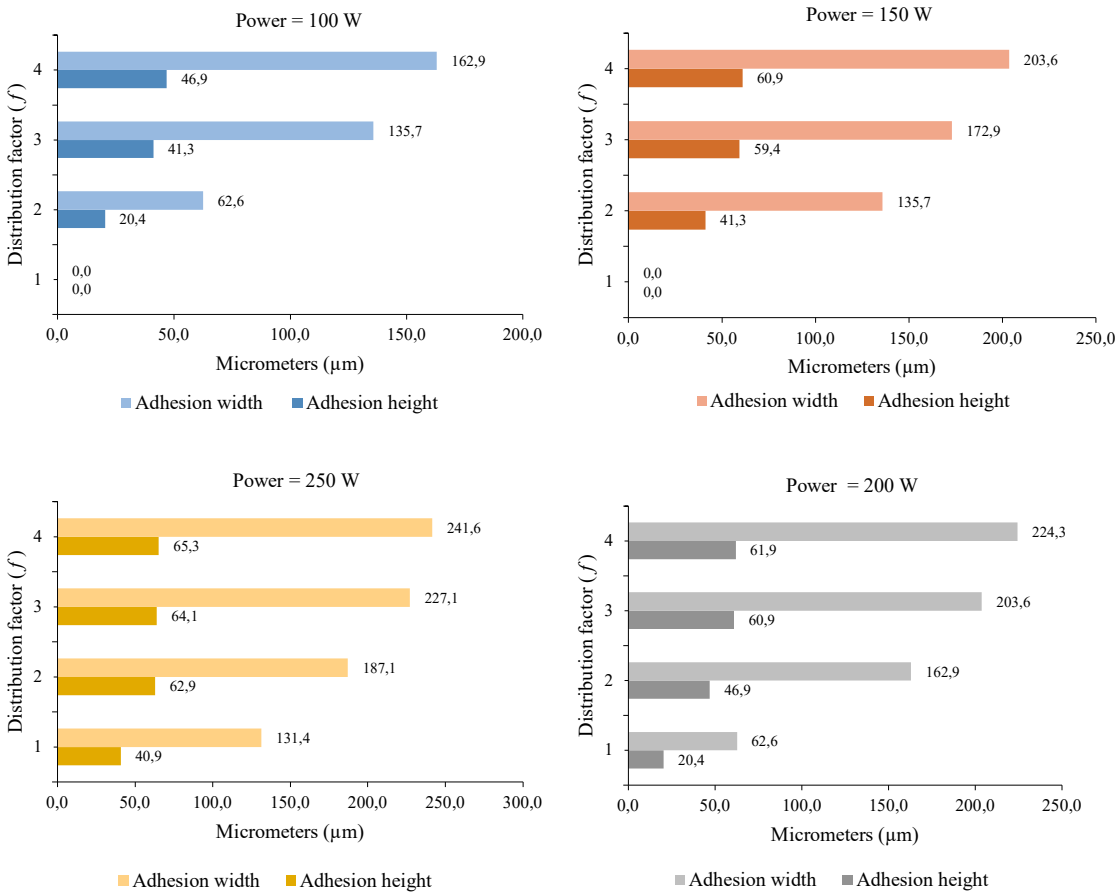

Source: Author

Figure 63 – Sintering ring-part process from the first up to the fourth lap in a representative case

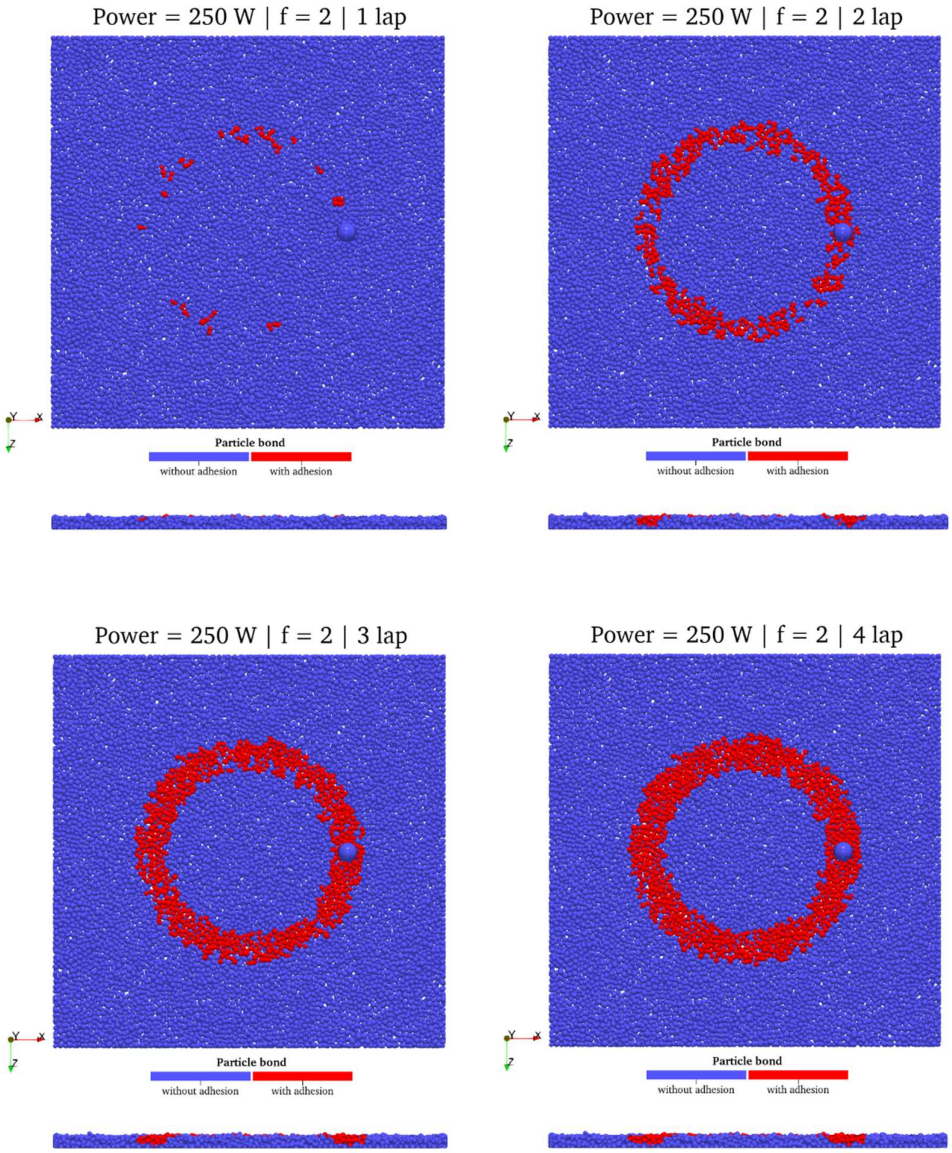

Source: Author.

As we can see in Figure 60, the number of particles with bonding directly depends on the power of the laser and the distribution factor. However, too high values may turn some particles into gas, and this could create an undesired entrapped porosity on the final manufactured piece (see Figure 54 and the bars in magenta color of Figure 60). Another interesting aspect is that when the value of f increases (i.e., the energy becomes more focused), the width and the height of the ring increase too, independently of the laser power. For example, when the power is 50 W and $f = 3$ only few particles experience adhesion and no ring is

formed, but when $f = 4$ we obtain a ring with $\overline{w} =$ 62.6 μm and $\overline{h} =$ 20.4 μm. Other values are summarized in Figure 61 and Figure 62. To show in detail the process, we choose one representative case of the sintering process in which the bonded particles are depicted after the laser beam has completed each of the four laps, see Figure 63. For the series of simulations presented in this example, we have varied the intensity and distribution factor of the laser and fixed the scanning velocity and the size of the particles, but our model has the flexibility to vary other parameters like the type of material, the scanning speed, and so on. The optimal set of parameters to be determined will depend on the material, geometry and purpose of the fabricated piece.

So far, we have run the simulations up to the laser beam completed four laps, and only during this interval of time, the particles located at the top of the domain were allowed to cool through convection and radiation with the environment. So, as a curiosity and to ascertain the robustness of our model during a long cooling phase, we run one more simulation with a longer time (equivalent to ten more laps of the laser, however without the laser) to let the particles cool. We note that cooling through conduction also takes place, since the hotter particles of the ring loose heat to the neighboring cooler ones. We choose a laser power of 200 W and $f = 2$ because those are typical values found in the literature. Figure 64 shows an isometric and side view of the temperature distribution at the fourth lap ($t =$ 0.00628 s) and Figure 65 and Table 9 summarizes the other results at different intervals of time.

Figure 64 – Temperature distribution at the fourth lap. Left: isometric view. Right: side view

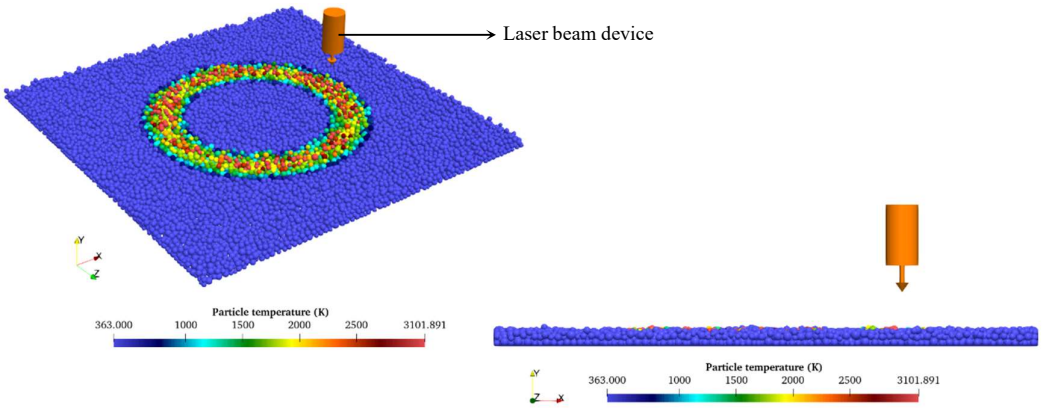

Source: Author.

Figure 65 – Temperature distribution during the cooling phase. Top left: fourth lap. Top right: eighth lap. Bottom left: twelfth lap. Bottom right: fourteenth lap

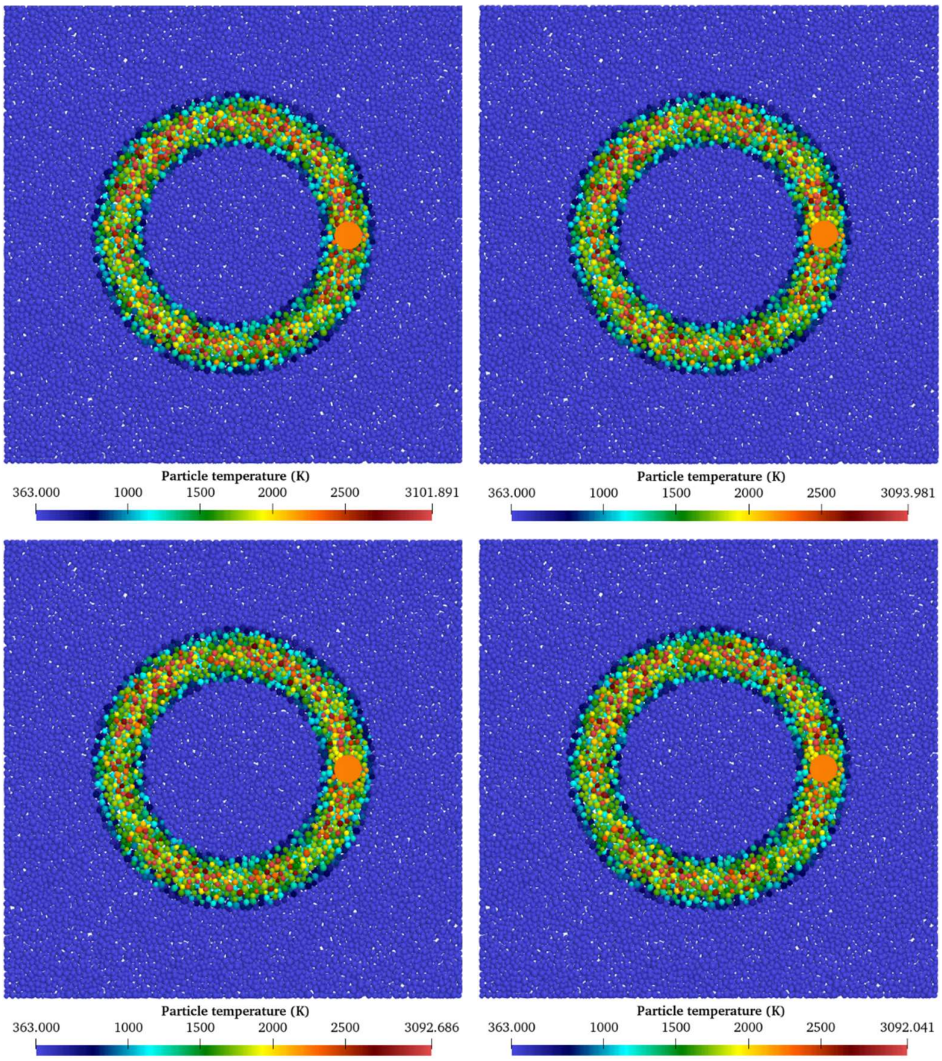

Source: Author.

Table 9. Summary of temperatures during the cooling phase

Lap	Final temperature (K)	Time (s)
4th	3101.891	0.00628
8th	3093.981	0.01256
12th	3092.686	0.01884
14th	3092.041	0.02198

Source: Author

Chapter 6

Conclusions and future works

In this work, we presented a thermo-mechanical computational model for the simulation of problems involving thermo-mechanically-active particles forming discrete particle systems, in an attempt to simulate modern advanced manufacturing processes and, in particular, SLS processes. In this Chapter, we discuss about the relevant aspects of this work, limitations and possible extensions.

6.1 Conclusions

This research aimed to propose a thermo-mechanical model for the simulation of advanced manufacturing processes, in particular, SLS process. An original adhesion force model for inter-particle bonding, for the study and simulation of modern engineering applications involving dry particulate media was presented. The computational implementation was addressed through an in-house DEM code developed by the author and performed in the Fortran 90 language. Based on the quantitative and qualitative results, it can be concluded that the proposed model is able to incorporate the most essential ingredients that are relevant in SLS process. The incorporation of thermal effects into the DEM mechanical model, combining with a bond model has demonstrated to be highly versatile to simulate not only AM processes, but also other types of problems involving particulate materials in association with heat transfer mechanisms. A briefly summary of the main relevant aspect of the present work is discussed below.

In Chapter 2, we introduce the mechanical DEM formulation, as well as the forces and moments involved in the physical problem that we are interested to solve. The numerical solution procedure to solve the governing equations was presented in Section 2.4. Special attention was given to the adhesion force presented in Chapter 3, where the bond model proved to work very well for capturing inter-particle bonding − at least for the purposes envisioned and the types of problems we are interested in. In particular, through consideration of a simple mass-dependent viscous term, the model turns well-suited for problems involving the bonding of either small and non-small particles (with sizes of the order of at least a few hundred micrometers), wherein inertia forces are relevant, and adhesion theory-based models are usually not satisfactory.

In Chapter 4, we present our developments to incorporate the thermal effects into the DEM (mechanical-only) model of Campello [9] [10] [11], with detailed accounts of each possible heat transfer mechanism and the numerical method for solution of the system´s equations. To test our thermo-mechanical model, the example 4.10.1 presents a simple validation problem involving only a single particle, attempting to assess some of the features of our scheme under simple idealized conditions. In the example 4.10.2, we extended our analysis from a single to a multi-particle system by analyzing the response of a granular stack when this is heating up while it is being vibrated under certain frequencies. The results showed that when the heat transfer by convection is considered, it dominates the overall heat transfer mechanism, not allowing the particles to heat up significantly, however, if convection is not considered, the particles' temperatures steadily grow as the bottom and lateral layers are heated due to multiple contacts with the walls, and from them, other particle layers through inter-particle conduction. Similar conclusions we found in the example 4.10.3, which is the 3D version of the same example. With respect to the final configuration of the particles at the end of the simulation, we did not find significantly difference with respect to the reference work, Campello [11] (without the consideration of thermal effects), the reason of this could be in the fact that we did not considered the degrading of the mechanical properties (elastic modulus), which is a source of coupling between the thermal and mechanical fields and affects the overall structure of the particle packing.

Another type of problem (although particularly important in the context of granular materials) we investigate in the example 4.10.4, our interest was to determine the effective (i.e.,

bulk) thermal conductivity of a particle assembly, which is an important parameter for calculating the heat exchange between granular contact pairs. The results demonstrated a strong dependency of the cross-sectional size contact with the heat conduction rate, affecting the final value of the thermal conductivity of the overall assembly. The size of the contacting pair directly depends on the increment of the overlap between particles, which in the case of the example, is due to the degrading of the elastic modulus.

With respect to problems concerning to AM processes, in the example 4.10.5, we choose a reference solution of a sintering bed of particles proposed by Ganeriwala and Zohdi [121] to validate our thermo-mechanical model, our intention was to see the effect of the heat transfer by conduction in this type of problems, especially, during the phase change. Variation of the material properties (mechanical and thermal) as a function of temperature and phase as well as, adhesion force, thermal interaction with the base and heat transfer by convection and radiation were not considered. The obtained results showed that the average temperature obtained in the simulation was in very good agreement with those from the reference work. Moreover, we realize that the smallest particles turn out into gas before the larger particles melted, which is a very important fact in this type of problems since this gas bubble may create an entrapped porosity on the final manufactured piece. For this reason, the particle size distribution becomes an important aspect which must be considered. Under high working temperatures, volumetric variation due to thermal expansion (or contraction) requires a special attention, for that reason, we run another simulation considering this effect and the results showed only a small increment in the overall average temperature (about 3%), but this value could be different for other types of materials, laser power or particle size distribution.

In the first example of Chapter 5, we proceed to calibrate the particles´ properties using the results of Ganeriwala and Zodhi [116], which it was a recreation of an experiment conducted by Khairallah and Anderson [91]. With the calibrated properties, in the example 5.2 we repeat the same problem setting as in example 4.10.5, but now taking the material properties of real metallic powders that are usually used PBF techniques. Our intention was to analyze and compare the influence on the results when the simulation is performed with real material properties and laser type as used in AM processes. By the obtained results we found significative differences especially in the temperature distribution in which the absorptivity of the material and the type of laser beam adopted highly influenced in the amount of energy

adsorbed by the particles. Finally, in the example 5.3 we put in practice all the variables that most influenced in a real SLS process, considering real material calibrated properties of the particles (performed in the example 5.1), a type of laser commonly used in this type of processes (Gaussian laser beam) and including the bonding between particles (presented in Chapter 3) to simulate a sintering ring-like part.

By the obtained results we found very interesting conclusions, for example, how the amount and distribution (w.r.t. the beam´s cross-section) of energy provided to the system influenced on the final number of particles with bonding and its effects on the quality of the final manufactured piece. This can be very helpful in the configuration of the best desirable scenario that will guarantee the proper bonding between particles and the amount of energy that will be required. Moreover, this model allows us to study an optimal size distribution of particles to ensure the maximum quantity of particles with adhesion without reaching an undesirable gas phase, that as we said before, will be increase the porosity. We believe that, with models of the type as proposed here, many AM industrial processes may be optimized, and experimental tests may be set up in a more oriented way.

6.2 Future works

The results obtained along the course of the thesis encourage us to continue exploring other scenarios to allow the optimization of various process parameters, for example, modifying the scan velocity in combination with the intensity of the laser or the particle size distribution. Incorporate more particle layers to turn the process more realistic and include a second (a posteriori) mechanical analysis to study the development of residual stresses during the colling phase. Mixing different types of materials in the same manufactured part in attempting to incorporate specific mechanical characteristics its also a field of great interest for us. Chemical reactions may be considered too. Another area that we are interested to explore is the genetic algorithms and machine learning, looking for to incorporate the potentialities of these powerful tools in the optimization of AM processes.

Bibliography

[1] M. Cotteleer, J. Holdowsky, M. Matho e J. Coykendall, "3D opportunity for aerospace and defense: Additive manufacturing takes flight," [Online]. Available: https://www2.deloitte.com/us/en/insights/focus/3d-opportunity/additive-manufacturing-3d-opportunity-in-aerospace.html. [Acesso em April 2021].

[2] D. E. Mouzakis, "Advanced Technologies in Manufacturing 3D-Layered Structures for Defense and Aerospace," em *Lamination | Theory and Application*, IntechOpen, 2018.

[3] XtreeE. [Online]. Available: http://www.xtreee.com. [Accessed April 2021].

[4] D. Lowke, E. Dini, A. Perrot, D. Weger, C. Gehlen e B. Dillenburguer, "Particle-bed 3D printing in concrete construction – Possibilities and challenges," *Cement and Concrete Research,* vol. 112, pp. 50-65, 2018.

[5] R. Patrick, M. Nicodemi, R. Delannay, P. Ribière e D. Bideau, "Slow relaxation and compaction of granular systems," *Nature Materials,* vol. 4, pp. 121-128, 2005.

[6] E. U. Schlünder, "Particle Heat Transfer," em *Proceedings of the Seventh Heat Transfer International Conference*, Munich, 1982.

[7] W. King, A. Anderson, R. Ferencz, N. Hodge, C. Kamath e S. Khairallah, "Overview of modelling and simulation of metal powder bed fusion process at Lawrence Livermore National Laboratory," *Materials Science and Technology,* vol. 31, nº 8, pp. 957-968, 2015.

[8] Anon, *3D printing and the new shape of industrial manufacturing,* Delaware: PricewaterhouseCoopers LLP, 2014.

[9] E. Campello, "A description of rotations for DEM models of particle systems," *Computational Particle Mechanics,* vol. 2, pp. 109-125, 2015.

[10] E. Campello, *Um modelo computacional para o estudo de materiais granulares. Habilitation thesis, Escola Politécnica da Universidade de São Paulo,* São Paulo, 2016.

[11] E. Campello, "A computational model for the simulation of dry granular materials," *International Journal of Non-Linear Mechanics,* vol. 106, pp. 89-107, 2018.

[12] T. Zohdi, Dynamics of charged particulate systems: modeling, theory and computation, New York: Springer, 2012.

[13] T. Zohdi, "Additive particle deposition and selective laser processing — a computational manufacturing framework," *Computational Mechanics,* vol. 54, pp. 171-191, 2014.

[14] J. Duran, Sands, powders and grains: an introduction to the physics of granular matter, New York: Springer, 1997.

[15] P. Cundall, “A computer model for simulating progressive large scale movements in blocky rock systems,” em *Proc. Symp. Int. Soc. Rock Mech*, Nancy, 1971.

[16] P. Cundall, “A Computer Model for Rock Mass Behavior Using Interactive Graphics for the Input and Output of Geometrical Data,” em *Technical Report MRD-2-74*, Minneapolis, 1974.

[17] P. Cundall e O. Strack, “The distinct element method as a tool for research in granular media. Report to the National Science Foundation. Part I,” Department of Civil and Mineral Engineering, University of Minnesota, Minneapolis , 1978.

[18] P. Cundall e O. Strack, “The distinct element method as a tool for research in granular media. Report to the National Science Foundation. Part II,” Department of Civil and Mineral Engineering, University of Minnesota, Minneapolis, 1978.

[19] P. Cundall e O. Strack, “A discrete numerical model for granular assemblies,” *Géotechnique,* vol. 29, nº 1, pp. 47-65, 1979.

[20] T. Wakabayashi, “Photoelastic method for determination of stress in powdered mass,” em *Proceedings of the 7th Japanese National Congress for Applied Mechanics*, Tokyo, 1957.

[21] H. Deresiewicz, “Mechanics of Granular Matter,” *Advances in Applied Mechanics,* vol. 5, pp. 233-306, 1958.

[22] N. Bićanić, “Discrete Element Methods. Part 1. Fundamentals,” *Encyclopedia of Computational Mechanics,* vol. Chichester , nº John Wiley & Sons, pp. 1-33, 2004.

[23] P. Thomas e J. Bray, “Capturing nonspherical shape of granular media with disk clusters,” *Jornal of Geotechnical and Geoenviromental Engineering,* vol. 125, nº 3, pp. 169-178, 1999.

[24] L. Vu-Quoc, X. Zhang e O. Walton, “A 3-D discrete-element method for dry granular flows of ellipsoidal particles,” *Computer Methods in Applied Mechanics and Engineering,* vol. 187, nº 3-4, pp. 483-528, 2000.

[25] J. Favier, M. Abbaspour-Fard, M. Kremmer e A. Raji, “Shape representation of axi-symmetrical, non-spherical particles in discrete element simulation using multi-element model particles,” *Engineering Computations,* vol. 16, nº 4, pp. 467-480, 1999.

[26] C. O'Sullivan, *The Application of Discrete Element Modelling to Finite Deformation Problems in Geomechanics. Ph.D. thesis,* Berkeley: University of California, 2002.

[27] N. Das, P. Giordano, D. Barrot, S. Mandayam, A. Ashmawy e B. Sukumaran, “Discrete element modeling and shape characterization of realistic granular shapes,” em *Proceedings of the Eighteenth International Offshore and Polar Engineering Conference, ISOPE’08*, Vancouver, 2008.

[28] A. X. Jerves, R. Y. Kawamoto e J. E. Andrade, “A geometry-based algorithm for cloning real grains,” *Granular Matter,* pp. 19-30, 2017.

[29] D. A. Medina e A. X. Jerves, “A geometry-based algorithm for cloning real grains 2.0,” *Granular Matter,* 2019.

[30] A. H. Barr, “Superquadrics and Angle-Preserving Transformations,” *IEEE Computer Graphics and Applications ,* vol. 1, nº 1, pp. 11-23, 1981.

[31] P. Cleary, “Large scale industrial DEM modelling,” *Engineering Computations,* vol. 21, nº 2/3/4, pp. 169-204, 2004.

[32] P. Cleary, "DEM prediction of industrial and geophysical particle flows," *Particuology,* vol. 8, nº 2, pp. 106-118, 2010.

[33] P. Cleary e M. L. Sawley, "DEM modelling of industrial granular flows: 3D case studies and the effect of particle shape on hopper discharge," *Applied Mathematical Modelling ,* vol. 26, pp. 89-111, 2002.

[34] A. Podlozhnyuk, S. Pirker e C. Kloss, "Efficient implementation of superquadric particles in Discrete Element Method within an open-source framework," *Computational Particle Mechanics,* vol. 4, pp. 101-118, 2017.

[35] P. Cundall, "Formulation of a three-dimensional distinct element model — Part I. A scheme to detect and represent contacts in a system composed of many polyhedral blocks," *International Journal of Rock Mechanics and Mining Sciences & Geomechanics,* vol. 25, nº 3, pp. 99-182, 1988.

[36] E. G. Nezami, Y. M. Hashash, D. Zhao e J. Ghaboussi, "A fast contact detection algorithm for 3-D discrete element method," *Computers and Geotechnics,* vol. 31, nº 7, pp. 575-587, 2004.

[37] T. Pöschel e T. Schwager, Computational Granular Dynamics, Berlin: Springer-Verlag, 2005.

[38] F. Alonso-Marroquín e Y. Wang, "An efficient algorithm for granular dynamics simulations with complex-shaped objects," *Granular Matter,* vol. 11, pp. 317-329, 2009.

[39] A. A. Serrano e J. M. Rodriguez-Ortiz, "A contribution to the mechanics of heterogeneous granular media," em *Proceedings of the Symposium on the role of plasticity in soil mechanics*, Cambridge, 1973.

[40] S. Li, J. S. Marshall, G. Liu e Q. Yao, "Adhesive particulate flow: The discrete-element method and its application in energy and environmental engineering," *Progress in Energy and Combustion Science,* vol. 37, pp. 633-668, 2011.

[41] C. O'Sullivan, Particulate Discrete Element Modelling. A Geomechanics Perspective, New York: Spon Press, 2011.

[42] H. Zhu, Z. Zhou, R. Yang e A. Yu, "Discrete particle simulation of particulate systems: A review of major applications and findings," *Chemical Engineering Science,* vol. 63, pp. 5728-5770, 2008.

[43] X. Zhang e L. Vu-Quoc, "Simulation of chute flow of soybeans using an improved tangential force-displacement model," *Mechanics of Materials,* vol. 32, nº 2, pp. 115-129, 2000.

[44] A. J. Matchett, T. Yanagida, Y. Okudaira e S. Kobayashi, "Vibrating powder beds: A comparison of experimental and Distinct Element Method simulated data," *Powder Technology,* vol. 107, nº 1-2, pp. 13-30, 2000.

[45] S. C. Yang e S. S. Hsiau, "Simulation study of the convection cells in a vibrated granular bed," *Chemical Engineering Science,* vol. 55, nº 18, pp. 3627-3637, 2000.

[46] M. Saeki, "Analytical study of multi-particle damping," *Journal of Sound and Vibration,* vol. 281, nº 3-5, pp. 1133-1144, 2005.

[47] H. Zhu, Z. Y. Zhou, R. Y. Yang e A. B. Yu, "Discrete particle simulation of particulate systems: Theoretical developments," *Chemical Engineering Science ,* vol. 62, pp. 3378-3396, 2007.

[48] J. S. Curtis e B. Van Wachem, "Modeling particle-laden flows: A research outlook," 2004. [Online]. Available: https://aiche.onlinelibrary.wiley.com/doi/epdf/10.1002/aic.10394. [Acesso em April 2021].

[49] Y. T. Feng, K. Han e D. R. J. Owen, "Coupled lattice Boltzmann method and discrete element modelling of particle transport in turbulent fluid flows: Computational issues," *International Journal for Numerical Methods in Engineering,* vol. 72, pp. 1111-1134, 2007.

[50] Y. T. Feng e D. R. J. Owen, "Advances in Computational Modelling of Multi-Physics in Particle-Fluid Systems," em *Particle-Based Methods. Fundamentals and Applications. Part of the Computational Methods in Applied Sciences*, vol. 25, Springer, 2011, pp. 51-88.

[51] F. Radjaï e F. Dubois, Discrete-element Modeling of Granular Materials, Wiley-ISTE, 2011.

[52] J. Sun e M. M. Chen, "A theoretical analysis of heat transfer due to particle impact," *International Journal of Heat and Mass Transfer,* vol. 31, nº 5, pp. 969-975, 1988.

[53] O. Molerus, "Particle-to-gas heat transfer in particle beds at Peclet numbers Pe ≤ 10," *Powder Technology,* vol. 90, nº 1, pp. 47-51, 1997.

[54] J. C. Chen e S. W. Churchill, "Radiant Heat Transfer in Packed Beds," *American Institute of Chemical Engineering,* vol. 9, nº 1, pp. 35-41, 1963.

[55] R. Siegel e J. R. Howell, Thermal Radiation Heat Transfert, McGraw-Hill, 1981.

[56] Y. S. Yang, J. R. Howell e D. E. Klein, "Radiative heat transfer through a randomly packed bed of spheres by the monte carlo method," *Journal of Heat Transfer,* vol. 105, pp. 325-332, 1983.

[57] B. P. Singh e M. Kaviany, "Modelling radiative heat transfer in packed beds," *International Journal of Heat and Mass Transfer,* vol. 35, nº 6, pp. 1397-1405, 1992.

[58] W. Strieder, "Radiation heat transport in disordered media," *Advances in Water Resources,* vol. 20, nº 2-3, pp. 171-187, 1997.

[59] Q. Brewster, "Volume Scattering of Radiation in Packed Beds of Large, Opaque Spheres," *Journal of Heat Transfer,* vol. 126, nº 6, pp. 1048-1050, 2004.

[60] C. Argento e D. Bouvard, "Thermal conductivity of granular media," em *Proceedings of the Second International Conference on Micromechanics of Granular Media. Powder & Grains*, Birmingham, 1993.

[61] G. K. Batchelor e R. W. O'Brien, "Thermal or Electrical Conduction Through a Granular Material," em *Proceedings of the Royal Society of London. Series A, Mathematical and Physical Sciences*, 1977.

[62] A. Majumdar e B. Bhushan, "Fractal Model of Elastic-Plastic Contact Between Rough Surfaces," *Journal of Tribology,* vol. 113, nº 1, pp. 1-11, 1991.

[63] M. R. Sridhar e M. M. Yovanovich, "Elastoplastic Constriction Resistance Model for Sphere-Flat Contacts," *Journal of Heat Transfer,* vol. 118, nº 1, pp. 202-205, 1996.

[64] R. L. Jackson, S. H. Bhavnani e T. Ferguson, "A Multiscale Model of Thermal Contact Resistance Between Rough Surfaces," *Journal of Heat Transfer,* vol. 130, nº 8, pp. 081301(1-8), 2008.

[65] Y. T. Feng, K. Han e D. R. J. Owen, "Discrete thermal element modelling of heat conduction in particle systems: Basic formulations," *Journal of Computational Physics,* vol. 227, nº 10, pp. 5072-5089, 2008.

[66] W. W. M. Siu e S. H. -K. Lee, "Transient temperature computation of spheres in three-dimensional random packings," *International Journal of Heat and Mass Transfer,* vol. 47, pp. 887-898, 2004.

[67] C. Argento e D. Bouvard, "Modeling the effective thermal conductivity of random packing of spheres through densification," *International Journal of Heat and Mass Transfer,* vol. 39, nº 7, pp. 1343-1350, 1996.

[68] M. L. Hunt, "Discrete element simulations for granular material flows: effective thermal conductivity and self-diffusivity," *International Journal of Heat and Mass Transfer,* vol. 40, nº 13, pp. 3059-3068, 1997.

[69] G. J. Cheng, A. B. Yu e P. Zulli, "Evaluation of effective thermal conductivity from the structure of a packed bed," *Chemical Engineering Science,* vol. 54, nº 19, pp. 4199-4209, 1999.

[70] W. L. Vargas-Escobar, *Discrete Modeling of Heat Conduction in Granular Media. Doctoral thesis,* Pittsburgh: University of Pittsburgh. School of Engineering, 2002.

[71] C. K. Chan e C. L. Tien, "Conductance of Packed Spheres in Vacuum," *Journal of Heat Transfer,* vol. 95, nº 3, pp. 302-308, 1973.

[72] S. Ji e L. Liu, Computational Granular Mechanics and Its Engineering Applications, Singapore: Springer, 2020.

[73] H. W. Zhang, Q. Zhou, H. L. Xing e H. Muhlhaus, "A DEM study on the effective thermal conductivity of granular assemblies," *Powder Technology,* vol. 205, nº 1-3, pp. 172-183, 2011.

[74] M. Baniasadi, M. Baniasadi e B. Peters, "Coupled CFD-DEM with heat and mass transfer to investigate the melting of a granular packed bed," *Chemical Engineering Science,* vol. 178, pp. 136-145, 2018.

[75] F. Dierich, P. A. Nikrityuk e S. Ananiev, "2D modeling of moving particles with phase-change effect," *Chemical Engineering Science,* vol. 22, nº 15, pp. 5459-5473, 2011.

[76] H. Gan, J. J. Feng e H. H. Hu, "Simulation of the sedimentation of melting solid particles," *International Journal of Multiphase Flow,* vol. 29, nº 5, pp. 751-769, 2003.

[77] T. Oschmann e H. Kruggel-Emden, "A novel method for the calculation of particle heat conduction and resolved 3D wall heat transfer for the CFD/DEM approach," *Powder Technology,* vol. 338, pp. 289-303, 2018.

[78] M. N. Ozisik, Finite Difference Methods in Heat Transfer, Boca Raton: CRC Press, 1994.

[79] A. -. C. F. o. A. M. Technologies, "ASTM International," [Online]. Available: https://www.astm.org/COMMITTEE/F42.htm. [Acesso em April 2021].

[80] I. Gibson, D. Rosen e B. Stucker, Additive Manufacturing Technologies - 3D Printing, Rapid Prototyping , and Direct Digital Manufacturing, London: Springer, 2015.

[81] J. O. Milewski, Additive Manufacturing of Metals. From Fundamental Technology to Rocket Nozzles, Medical Implants, and Custom Jewelry, Springer, 2017.

[82] K. Du, S. Li, S. Jie, X. Gao e Y. Yu, “Effect of 316L stainless steel powder size distribution on selective laser melting process,” em *Journal of Physics: Conference Series. XV International Russian–Chinese Symposium "NEW MATERIALS AND TECHNOLOGIES"*, Sochi, 2019.

[83] Q. Chen, G. Guillemot, C.-A. Gandin e M. Bellet, “Three-dimensional finite element thermomechanical modeling of additive manufacturing by selective laser melting for ceramic materials,” *Additive Manufacturing,* vol. 16, pp. 124-137, 2017.

[84] R. Ganeriwala, *Multiphysics Modeling of Selective Laser Sintering/Melting. Ph.D. thesis,* Berkeley: University of California, 2015.

[85] A. Simchi e H. Pohl, “Effects of laser sintering processing parameters on the microstructure and densification of iron powder,” *Materials Science and Engineering: A,* vol. 359, nº 1-2, pp. 119-128, 2003.

[86] M. Matsumoto, M. Shiomi, K. Osakada e F. Abe, “Finite element analysis of single layer forming on metallic powder bed in rapid prototyping by selective laser processing,” *International Journal of Machine Tools and Manufacture,* vol. 42, nº 1, pp. 61-67, 2002.

[87] K. Antony, N. Arivazhagan e K. Senthilkumaran, “Numerical and experimental investigations on laser melting of stainless steel 316L metal powders,” *Journal of Manufacturing Processes,* vol. 16, nº 3, pp. 345-355, 2014.

[88] S. Kirihara e K. Nakata, Multi-dimensional Additive Manufacturing, Springer, 2021.

[89] A. Mokrane, M. Boutaous e S. Xin, “Process of selective laser sintering of polymer powders: Modeling, simulation, and validation,” *Comptes Rendus Mécanique,* vol. 346, nº 11, pp. 1087-1103, 2018.

[90] A. V. Gusarov e J.-P. Kruth, “Modelling of radiation transfer in metallic powders at laser treatment,” *International Journal of Heat and Mass Transfer,* vol. 48, nº 16, pp. 3423-3434, 2005.

[91] S. A. Khairallah e A. Anderson, “Mesoscopic simulation model of selective laser melting of stainless steel powder,” *Journal of Materials Processing Technology,* vol. 214, nº 11, pp. 2627-2636, 2014.

[92] T. Zohdi, Modeling and Simulation of Functionalized Materials for Additive Manufacturing and 3D Printing: Continuous and Discrete Media, Cham, Switzerland: Springer, 2018.

[93] T. Zohdi, “A direct particle-based computational framework for electrically enhanced thermo-mechanical sintering of powdered materials,” *Mathematics and Mechanics of Solids,* vol. 19, nº 1, pp. 93-113, 2014.

[94] T. Zohdi, “Rapid Simulation of Laser Processing of Discrete Particulate Materials,” *Archives of Computational Methods in Engineering,* vol. 20, pp. 309-325, 2013.

[95] K. L. Johnson, Contact Mechanics, Cambridge: Cambridge University Press, 1985.

[96] K. Iwashita e M. Oda, “Rolling resistance at contacts in simulation of shear band development by DEM,” *Journal of Engineering Mechanics,* vol. 124, nº 3, pp. 285-292, 1998.

[97] K. Han, Y. T. Feng e D. R. J. Owen, “Performance comparisons of tree-based and cell-based contact detection algorithms,” *Engineering Computations: Int J for Computer-Aided Engineering,* vol. 24, nº 2, pp. 165-181, 2007.

[98] C. K. P. Vallabh e C. Cetinkaya, "Single particle adhesion variability in additive manufacturing powders," *The Journal of Adhesion,* vol. 97, nº 1, pp. 19-37, 2019.

[99] K. L. Johnson, K. Kendall e A. D. Roberts, "Surface energy and the contact of elastic solids," em *Proceedings of the Royal Society London: A Mathematical, Physical and Engineering Sciences*, London, 1971.

[100] E. Campello e O. Quintana-Ruiz, "On a simple, stable and efficient bond model for inter-particle adhesion," *Computational Particle Mechanics,* Published online: 29 January 2021.

[101] J. E. Lennard-Jones, "On the determination of molecular fields. —II. From the equation of state of a gas," em *Proceedings of the Royal Society London A*, 1924.

[102] E. Campello e K. Cassares, "Rapid Generation of Particle Packs at High Packing Ratios for DEM Simulations of Granular Compacts," *Latin American Journal of Solids and Structures,* vol. 13, pp. 23-50, 2015.

[103] O. Quintana-Ruiz e E. Campello, "A coupled thermo-mechanical model for the simulation of discrete particle systems," *Journal of the Brazilian Society of Mechanical Sciences and Engineering,* vol. 42, nº 378, pp. 387(1-21), 2020.

[104] Y. T. Feng, K. Han e D. R. J. Owen, "Discrete thermal element modelling of heat conduction in particle systems: Pipe-network model and transient analysis," *Powder Technology,* vol. 193, nº 3, pp. 248-256, 2009.

[105] Y. Liang, "A series solution based formulation for discrete thermal element method of granular materials," *Granular Matter,* p. 23:11, 2021.

[106] S. Whitaker, "Forced convection heat transfer correlations for flow in pipes, past flat plates, single cylinders, single spheres, and for flow in packed beds and tube bundles," *American Institute of Chemical Engineers,* vol. 18, nº 2, pp. 361-371, 1972.

[107] H. Wessels, C. Weißenfels e P. Wriggers, "Metal particle fusion analysis for additive manufacturing using the stabilized optimal transportation meshfree method," *Computer Methods in Applied Mechanics and Engineering,* vol. 339, pp. 91-114, 2018.

[108] T. DebRoy, H. L. Wei, J. S. Zuback, T. Mukherjee, J. W. Elmer, J. O. Milewski, A. M. Beese, A. Wilson-Heid, A. De e W. Zhang, "Additive manufacturing of metallic components – Process, structure and properties," *Progress in Materials Science,* vol. 92, pp. 112-224, 2018.

[109] A. V. Gusarov, I. Yadroitsev, P. Bertrand e I. Smurov, "Model of Radiation and Heat Transfer in Laser-Powder Interaction Zone at Selective Laser Melting," *Journal of Heat Transfer,* vol. 131, nº 7, pp. 072101(1-10), 2009.

[110] E. Campello, "Effect of particle spin on the spatio-thermal distribution of incandescent materials released from explosions," *Journal of the Brazilian Society of Mechanical Sciences and Engineering,* vol. 42, pp. 40(1-11), 2020.

[111] D. S. Driver, *Discrete Element Multiphysical Models for Additive Manufacturing in conjunction with a Domain Specific Language for Computational Mechanics. Ph.D. thesis,* Berkeley: University of California, 2015.

[112] C. Bonacina, G. Comini, A. Fasano e M. Primicerio, "Numerical solution of phase change problems," *International Journal of Heat and Mass Transfer,* vol. 16, nº 10, pp. 1825-1832, 1973.

[113] M. Muhieddine, É. Canot e R. March, "Various approaches for solving problems in heat conduction with phase change," *International Journal on Finite Volumes,* vol. 6, nº 1, pp. 66-85, 2009.

[114] M. Zeneli, A. Nikolopoulos, S. Karellas e N. Nikolopoulos, *Numerical methods for solid-liquid phase-change problems,* 2021.

[115] H. T. Hashemi e C. M. Sliepcevich, "A numerical method for solving two-dimensional problems of heat conduction with change of phase," em *Chem. Eng. Prog. Symp. Series*, 1967.

[116] R. Ganeriwala e T. Zohdi, "A coupled discrete element-finite difference model of selective laser sintering," *Granular Matter,* vol. 21, pp. 18(1-15), 2016.

[117] H. Xin, W. Sun e J. Fish, "Discrete element simulations of powder-bed sintering-based additive manufacturing," *International Journal of Mechanical Sciences,* vol. 149, pp. 373-392, 2018.

[118] H. Wessels, *Thermo-Mechanical Modeling for Selective Laser Melting. Ph.D. thesis,* Hannover: Gottfried Wilhelm Leibniz Universität Hannover, 2019.

[119] S. A. Galindo-Torres, "A coupled Discrete Element Lattice Boltzmann Method for the simulation of fluid–solid interaction with particles of general shapes," *Computer Methods in Applied Mechanics and Engineering,* vol. 265, pp. 107-119, 2013.

[120] C. Wellmann e P. Wriggers, "A two-scale model of granular materials," *Computer Methods in Applied Mechanics and Engineering,* Vols. %1 de %2205-208, pp. 46-58, 2012.

[121] R. Ganeriwala e T. Zohdi, "Multiphysics modeling and simulation of selective laser sintering manufacturing processes," *Procedia CIRP 14. 6th CIRP International Conference on High Performance Cutting, HPC2014,* pp. 299-304, 2014.

[122] E. Clément, L. Vanel, J. Rajchenbach e J. Duran, "Pattern formation in a vibrated two-dimensional granular layer," *Physical Review E,* vol. 53, nº 3, pp. 2972-2975, 1996.

[123] V. N. Dolgunin, A. N. Kudi, A. A. Ukolov e M. A. Tuev, "Rapid granular flows on a vibrated rough chute: Behaviour patterns and interaction effects of particles," *Chemical Engineering Research and Design,* vol. 122, pp. 22-32, 2017.

[124] Z. Hashin e S. Shtrikman, "On some variational principles in anisotropic and non-homogeneous elasticity," *Journal of the Mechanics and Physics of Solids,* vol. 10, pp. 335-342, 1962.

[125] Z. Hashin e S. Shtrikman, "A variational approach to the theory of the elastic behaviour of multiphase materials," *Journal of the Mechanics and Physics of Solids,* vol. 11, pp. 127-140, 1963.

[126] Z. Hashin, "Analysis of composite materials: a survey," *ASME Journal of Applied Mechanics,* vol. 50, pp. 481-505, 1983.

[127] T. Zohdi e E. Campello, "On Pressurized Functionalized Particle-Laden Fluid Infiltration into Porous Media," *International Journal for Multiscale Computational Engineering,* vol. 17, nº 2, pp. 223-237, 2019.

[128] AK Steel, "316/316L Stainless Steel Product Data Bulletin," [Online]. Available: https://www.aksteel.com/sites/default/files/2018-01/316316L201706_2.pdf. [Acesso em April 2021].

[129] INCO databooks, “Reprinted from the publication "Mechanical and Physical Properties of the Austenitic Chromium-Nickel Stainless Steels at elevated temperatures,” 1968. [Online]. Available: https://nickelinstitute.org/media/1637/austeniticchromium_nickelstainlesssteelsatelevatedtemperatures_mechanicalandphysicalproperties_2980_.pdf. [Acesso em April 2021].

[130] K. Walton, “The effective elastic moduli of a random packing of spheres,” *Journal of the Mechanics and Physics of Solids,* vol. 35, nº 2, pp. 213-226, 1987.

[131] Y. Shi, W. Zhang, Y. Cheng e S. Huang, “Compound scan mode developed from subarea and contour scan mode for selective laser sintering,” *International Journal of Machine Tools and Manufacture,* vol. 47, nº 6, pp. 873-883, 2007.